6/16/65
123pps.

G. CHARPAK, *et al.*
16 Giugno 1965
Il Nuovo Cimento
Serie X, Vol. 37, pag. 1241-1363

The Anomalous Magnetic Moment of the Muon.

G. CHARPAK (*), F. J. M. FARLEY, R. L. GARWIN (**), T. MULLER (***), J. C. SENS and A. ZICHICHI

CERN - Geneva

(ricevuto il 18 Settembre 1964)

Summary. — The anomalous part of the gyromagnetic ratio, $\mathbf{a} \equiv \frac{1}{2}(g-2)$ of the muon has been measured by determining the precession $0 = \mathbf{a}\omega_0 \bar{B}t$ for 100 MeV/c muons as a function of storage time t in a known static magnetic field of the form $B = B_0(1+ay+by^2+cy^3+dy^4)$. The result is $\mathbf{a}_{\text{exp}} = (1162 \pm 5)\cdot 10^{-6}$ compared with the theoretical value $\mathbf{a}_{\text{th}} = \alpha/2\pi + 0.76\alpha^2/\pi^2 = 1165\cdot 10^{-6}$. This agreement shows that the muon obeys standard quantum electrodynamics down to distances ~ 0.1 fermi. Details are given of the methods used to store muons for $\sim 10^3$ turns in the field, and of measuring techniques and precautions necessary to achieve the final accuracy. Some of the methods of orbit analysis, magnet construction shimming and measurement, polarization analysis, and digital timing electronics may be of more general interest.

1. – Introduction.

1·1. *Purpose of the experiment.* – The correction to the gyromagnetic ratio g of the electron, first discovered experimentally through the splitting of the $2P_{\frac{1}{2}}$-$2S_{\frac{1}{2}}$ levels in hydrogen (Lamb shift), and explained as a consequence of

(*) On leave from Centre National de la Recherche Scientifique, Paris.
(**) IBM Watson Laboratory, Columbia University, New York.
(***) Centre National de la Recherche Scientifique and Institut de Recherches Nucléaires, Strasbourg.

the emission and reabsorption of virtual photons, has played a leading part in the development of quantum electrodynamics (QED). The theoretical result for the anomalous part of the gyromagnetic ratio is

$$\mathbf{a}_{\text{th}}\,(\text{electron}) \equiv \frac{g-2}{2} = \frac{\alpha}{2\pi} - 0.328\frac{\alpha^2}{\pi^2} = 1159.615\cdot 10^{-6}\,, \tag{1}$$

where one assumes

$$(\alpha)^{-1} = 137.0391 \tag{2}$$

has been confirmed with great accuracy, notably by the recent result of WILKINSON and CRANE (1)

$$\mathbf{a}_{\text{exp}}\,(\text{electron}) = 1159.622\cdot 10^{-6} \pm 0.027\cdot 10^{-6}\,. \tag{3}$$

The muon, apart from its mass, appears to have properties identical to the electron: the absence of strong interaction, the parallel role in the weak interaction, and the observation of the electromagnetic processes expected for a spin-$\frac{1}{2}$ particle point to this conclusion. The gyromagnetic ratio is close to 2, and conclusive evidence in favour of spin-$\frac{1}{2}$ is obtained from the experiments on muonium and muonic X rays (2).

If the muon is also to be described by the Dirac equation, similar corrections to its gyromagnetic ratio will apply. In this case the main contribution to the integrals used in evaluationg $\mathbf{a}_{\text{th}}$ comes from virtual photons of $q^2 \sim (m_\mu c)^2 \sim (100\ \text{MeV/c})^2$, so the result tests QED at much shorter distances. The prediction (3) is

$$\mathbf{a}_{\text{th}}\,(\text{muon}) = \frac{\alpha}{2\pi} + 0.76\frac{\alpha^2}{\pi^2} = 1165\cdot 10^{-6}\,, \tag{4}$$

the coefficient of the second term (fourth order in e) being different from eq. (1) because the contribution of virtual electron pairs produced by the virtual photon is greater in this case.

The importance of the anomalous magnetic moment of the muon as a test of QED at short distances was commented on by BERESTETSKIJ, KROKHIN

---

(1) D. T. WILKINSON and H. R. CRANE: *Phys. Rev.*, **130**, 852 (1963); W. H. LOUISELL, R. W. PIDD and H. R. CRANE: *Phys. Rev.*, **94**, 7 (1954).

(2) K. ZIOCK, V. W. HUGHES, R. PREPOST, J. BAILEY and W. CLELAND: *Phys. Rev. Lett.*, **8**, 103 (1962); G. BACKENSTOSS, K. GOEBEL, U. HEGEL, D. QUITMANN and B. STADLER: *Nucl. Phys.* (in press).

(3) A. PETERMANN: *Helv. Phys. Acta*, **30**, 407 (1957). A complete list of references is given in a review by A. PETERMANN: *Fortschr. d. Phys.*, **6**, 505 (1958). The numerical coefficient of the second term has now been evaluated for more precisely, PETERMANN: (private communication).

and KHLEBNIKOV in 1956 (4). Upon the discovery (5) of parity violation for muons in 1957, it was recognized that a direct measurement of the anomaly, that is of $(g-2)$, should be possible using the principles which had been applied to the electron by CRANE *et al.* (1). In 1958 PANOFSKY (6) reported that experiments were in progress independently in three laboratories.

In addition to its sensitivity to QED at short distances, this measurement gives direct information about the muon. If the muon has a structure the contribution of high momentum transfers to eq. (4) will be reduced leading to a lower value of a_{th}. On the other hand, any coupling of the muon to another field will modify the gyromagnetic ratio directly (through the emission and reabsorption of virtual field particles) either increasing or decreasing a_{th} according to the nature of the field (7). This provides a sensitive test of unknown interactions of the muon which are sometimes invoked, for example, to explain the $\mu-e$ mass difference (8).

Therefore, barring accidental cancellation of these effects, an accurate determination of the anomalous magnetic moment of the muon would:

i) test the validity of QED at short distances;

ii) explore the structure of the muon electromagnetic vertex; and

iii) indicate whether there is any unexplored coupling to another field, which might perhaps explain the mass difference between electron and muon.

Experimentally measurements on muons are subject to the difficulty that muon sources are weak and diffuse, and the natural lifetime requires the measurement to be completed in a few microseconds. On the other hand, theso urce ($\pi \to \mu$ decay) provides muons which are fully polarized at birth, and the anisotropic decay ($\mu^+ \to e^+ + \bar{\nu}_\mu + \nu_e$) provides an indicator for the final spin direction.

The best indirect evidence for the g factor is obtained by combining the precession frequency measurement for muons at rest in a known magnetic field B (9),

$$\omega_s = \frac{g}{2} \cdot \frac{eB}{mc}, \tag{5}$$

(4) V. B. BERESTETSKIJ, O. N. KROKHIN and A. K. KHLEBNIKOV: *Žurn. Eksp. Teor. Fiz.*, **30**, 788 (1956) [translation: *Soviet Physics JETP*, **12**, 993 (1961)].

(5) R. L. GARWIN, L. M. LEDERMAN and M. WEINRICH: *Phys. Rev.*, **105**, 1415 (1957).

(6) W. K. H. PANOFSKY: *Proceedings of the* 1958 *International Conference on High-Energy Physics at CERN* (ed. B. FERRETTI) (CERN, 1958), p. 4.

(7) W. S. COWLAND: *Nucl. Phys.*, **8**, 397 (1958).

(8) J. SCHWINGER: *Ann. Phys.*, **2**, 407, (1957).

(9) D. P. HUTCHINSON, J. MENES, G. SHAPIRO and A. M. PATLACH: *Phys. Rev.*, **131**, 1351 (1963). see also G. MCD. BINGHAM: *Nuovo Cimento*, **27**, 1352 (1963).

with the mass value obtained from a study of the 88 keV (3D — 2P) transition in μ-mesic phosphorus ([10-12]). This gives $g = 2(1.0011^{\pm 0.0001}_{\pm 0.0002})$ confirming the theoretical value of **a** to about 15%. Although ω_s/B is known to 1:60000, an improvement in the mass measurement beyond the present accuracy of 1:10000, and therefore in the determination of g, is hardly to be expected.

Here we describe the direct measurement of $(g-2)$ for the muon which gives the g-factor to an accuracy of 1:250000. Two short reports on this experiment have already been published. The first described a preliminary measurement of the anomalous moment to $\pm 1.7\%$ accuracy ([13]), while the second, published a year later, gave the result of a new experiment to $\pm 0.4\%$ incorporating many refinements and improvements in the technique ([14]).

1·2. *Principle of the method.* – In our experiment longitudinally muons (formed by forward decay in flight of pions from the CERN Synchro-cyclotron) are injected into an almost uniform magnetic field $B(\sim 16$ kG) in such a way that they describe many (~ 1000) quasi-circular orbits before reaching the end of the magnet and being ejected (see Fig. 1). While the muons are in the field, the anomalous moment causes the spin to turn faster than the momentum vector. After time dt the angle between spin and momentum ($\theta = \theta_s - \theta_p$) has changed by the amount

$$d\theta = \mathbf{a}\omega_0 B\, dt\,, \tag{6}$$

where ω_0 is the cyclotron frequency $e/m_0 c$ for low-energy muons in unit magnetic field. The total change in polarization angle after time t is therefore

$$\theta(t) - \theta(0) = \Delta\theta = \mathbf{a}\omega_0 \bar{B} t\,, \tag{7}$$

where $\bar{B}$ is the field averaged over the trajectory. By bringing the muons to rest in a field-free apparatus (polarization analyser) and observing their decay, the final polarization can be measured. In this way one records $\Delta\theta$ as a function of the storage time t, allowing **a** to be determined.

([10]) J. F. LATHROP, R. A. LUNDY, V. L. TELEGDI, R. WINSTON and D. D. YOVANOVITCH: *Nuovo Cimento*, **17**, 109 (1960).

([11]) J. F. LATHROP, R. A. LUNDY, S. PENMAN, V. L. TELEGDI, R. WINSTON and D. D. YOVANOVITCH: *Nuovo Cimento*, **17**, 114 (1960).

([12]) S. DEVONS, G. GIDAL, L. M. LEDERMAN and G. SHAPIRO: *Phys. Rev. Lett.*, **5**, 330 (1960).

([13]) G. CHARPAK, F. J. M. FARLEY, R. L. GARWIN, T. MULLER, J. C. SENS, V. L. TELEGDI and A. ZICHICHI: *Phys. Rev. Lett.*, **6**, 128 (1961).

([14]) G. CHARPAK, F. J. M. FARLEY, R. L. GARWIN, T. MULLER, J. C. SENS and A. ZICHICHI: *Phys. Lett.*, **1**, 16 (1962).

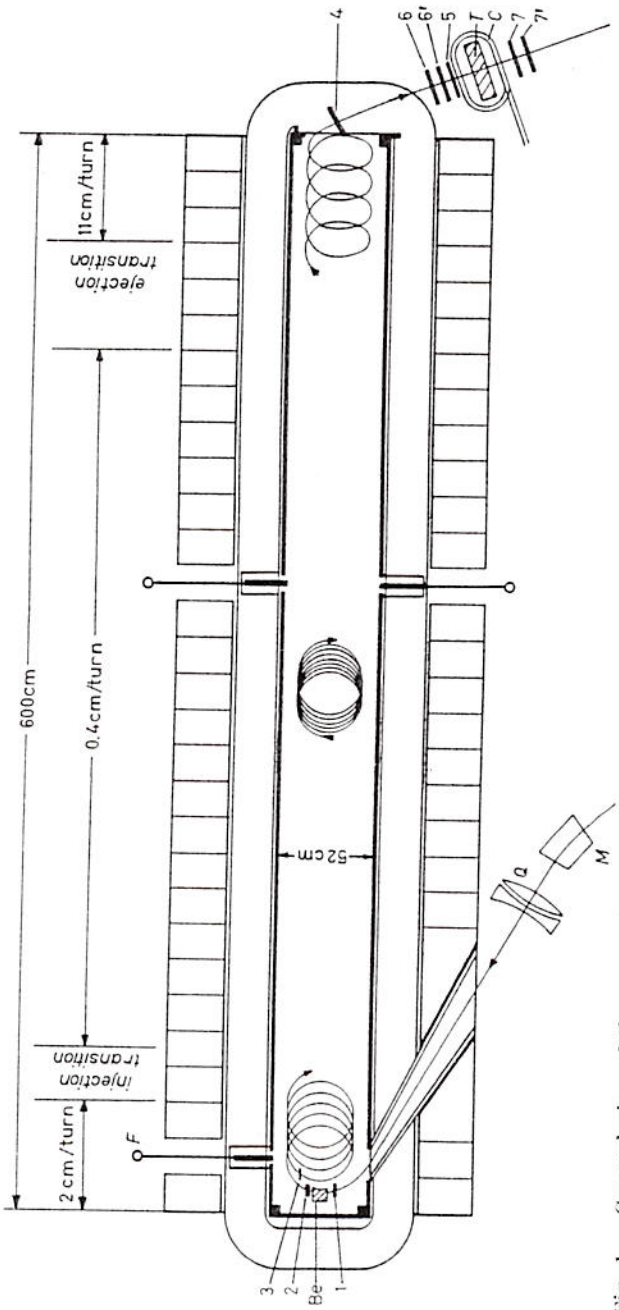

Fig. 1. – General view of the apparatus, showing magnet of pole surface $(600\times52)\,\mathrm{cm}^2$. Muons, deflected by the bending magnet M and focused by the quadrupole pair Q enter the magnet via a shielded channel. After slowing down in the beryllium moderator Be they describe many turns in the field. The quasi-circular orbit is slowly displaced by the field gradient (2 cm/turn in the *injection* region, 0.4 cm/turn in the *storage* region, and 11 cm/turn in the final *ejection* region). Muons ejected from the magnet are stopped in target T of the polarization analyser where the spin direction is determined by recording the decay electrons. Injected muons are indicated by the counter signature 123. Ejected muons by the signature $466'\,5\bar{7}$. Decay electrons by $66'\,4(\bar{7}7')$ and $77'\,\bar{4}(6\bar{6}')$. The time of flight of muons between counters 2 and 4 is recorded.

Equation (6) is easily verified for the nonrelativistic case. Its validity for relativistic particles in a uniform field has been established by BARGMANN, MICHEL and TELEGDI [15] who treat, in a rigorously covariant formalism, the motion of a classical magnetic gyrostat in an electromagnetic field. The equations also represent the average motion of a quantized spin because the expectation value of a quantum-mechanical operator for a system in a slowly varying field of force obeys the classical equations of motion. A purely quantum-mechanical proof of eq. (6) also exists.

As the change in polarization predicted by eq. (6) is $\sim 0.4°$ per turn, for an accurate measurement of a it is necessary to constrain the muons to circle many times in the field. To measure the muons' spin direction while they are still in the field presents many problems: it is desiderable eventually to extract the particles and bring them to rest in a field-free region. By observing the decay-electron asymmetry the final spin direction can then be established.

It is necessary, therefore, to set up a magnetic field into which the muons can be injected with high efficiency. After making a large number (~ 1000) of turns, they are finally ejected and fall on the measuring apparatus.

In our method a large conventional H-type magnet with a vertical field of 16 kG constant in time, between poles (52×600) cm^2 with 14 cm gap, is shimmed to give a field of special form, uniform along the x axis (long axis), but varying along the y axis (transverse axis, see Fig. 2)

$$B_z = B_0(1 + ay + by^2 + \ldots) \,. \tag{8}$$

This is necessary in order to store and focus the particles, as explained below.

Before going further, we examine the validity of eqs. (6) and (7) in the nonuniform fields used in the actual magnet.

Above and below the median plane there is a y-component of field

$$B_y = z \frac{\partial B_z}{\partial y} \,, \tag{9}$$

which gives rise to vertical oscillations (focusing) of the particles in the magnet. The question, is how does this affect the spin motion?

1'2.1. Spin motion in the storage magnet. The spin direction is defined in the rest frame of the muon, and does not change when the muon is slowed down in matter and stopped in a field-free region. (The electric fields which slow down the muon are longitudinal on the average, and after Lorentz transformation to the rest frame, give zero average magnetic field;

---

[15] V. BARGMANN, L. MICHEL and V. L. TELEGDI: *Phys. Rev. Lett.*, 2, 435 (1959).

therefore, they do not precess the spin. The effect of multiple scattering is considered below.)

The direction of the momentum vector $\boldsymbol{p}$ is defined in the laboratory frame. It remains the same when transferred to the rest frame by a Lorentz transformation parallel to $\boldsymbol{p}$.

The analysis of the spin motion is based on a result of BARGMANN, MICHEL and TELEGDI [15]. They express the spin direction with respect to a system of three orthogonal axes in the rest frame defined by vectors $\boldsymbol{e}_1$, $\boldsymbol{e}_2$, $\boldsymbol{e}_3$, which all rotate in the laboratory frame as if they were momentum vectors:

$$\dot{\boldsymbol{e}}_k = \omega_0 \boldsymbol{B} \times \boldsymbol{e}_k \,. \tag{10}$$

This system of axes is called the Michel frame. ($\boldsymbol{B}$ is the magnetic field in laboratory, the dot indicates differentiation with respect to proper time measured in the muon rest frame, and the constant $\omega_0 = e/m_0 c$ is the cyclotron frequency for low-energy muons in unit magnetic field. Vectors in the muon rest frame are indicated thus $\mathfrak{B}$.)

The orientation of the Michel axes is unimportant. We use only the fact that the whole frame rotates in the laboratory like a momentum vector, *i.e.* with angular frequency $\boldsymbol{\Omega}_p = \gamma^{-1}\omega_0 \mathfrak{B}$, where $\gamma = (1-\beta^2)^{-\frac{1}{2}}$ is included to convert proper time to laboratory time.

It is shown by Bargmann, Michel and Telegdi that in the rest frame with respect to these axes, the spin rotates at angular frequency $\boldsymbol{\Omega}_a = \mathbf{a}\,\omega_0 \mathfrak{B}$, where $\mathfrak{B}$ is the magnetic field in the rest frame. In laboratory time this becomes $\boldsymbol{\Omega}_a = \gamma^{-1} \cdot \mathbf{a}\omega_0 \mathfrak{B}$. To find the total rotation of the spin in the laboratory, we have to add these two angular velocities:

$$\boldsymbol{\Omega}_a + \boldsymbol{\Omega}_p = \gamma^{-1}\omega_0 \{\mathbf{a}\mathfrak{B} + \boldsymbol{B}\} \,. \tag{11}$$

As the momentum vector rotates about the field at angular frequency $\boldsymbol{\Omega}_p = \gamma^{-1}\omega_0 \boldsymbol{B}$, formula (6) for the case of motion perpendicular to a uniform field (where $\mathfrak{B} = \gamma B$) follows immediately.

In general, therefore, the procedure for calculating the spin motion is to calculate the rotation of the spin in the rest frame, about the direction defined by $\mathfrak{B}$; and to add to this the rotation of the Michel frame in the laboratory about the direction defined by $\boldsymbol{B}$. It is not, however, necessary to express analytically the first motion with respect to the Michel axes, which may have a complicated motion, as is done in the reference quoted; it will often be simpler to express both motions in terms of fixed laboratory axes.

Apply this now to our magnet with main field component B_z and horizontal field B', remembering that $\int B' \cdot \mathrm{d}l$ along the orbit is zero because the orbit does not encircle any current. The motion of the Michel frame is as follows.

About a vertical axis it rotates exactly as the momentum vector $\boldsymbol{p}$. About a horizontal axis perpendicular to $\boldsymbol{p}$, it oscillates because of the $\boldsymbol{B}'$ field, following exactly the vertical oscillations of the momentum vector ($\pm 2°$). It also has a rotational oscillation about $\boldsymbol{p}$ as axis because of the component of $\boldsymbol{B}'$ parallel to $\boldsymbol{p}$, but there is no net rotation because $\int \boldsymbol{B}' \cdot \mathrm{d}\boldsymbol{l} = 0$. In the worst case (ejection region where the coefficient a is as high as 10^{-2}) the oscillations are about $\pm 5°$.

To find the motion of the spin with respect to the Michel frame we must compute $\mathfrak{B}$, the field in the rest frame. If at any instant the trajectory is inclined at angle Θ to the y axis and at angle ζ to the horizontal, one finds by resolving the field parallel and perpendicular to the trajectory and transforming to the rest frame

$$\mathfrak{B}_z = \gamma B_z \left[1 + \zeta^2 \left(\frac{1}{\gamma} - 1\right)\right] + B_y \zeta (1 - \gamma) \cos \Theta \,, \tag{12}$$

while the horizontal components parallel and perpendicular to the projected trajectory are, respectively,

$$\mathfrak{B}_1 = -B_z(\gamma - 1)\zeta + B_y[1 + (\gamma - 1)\zeta^2]\cos\Theta \tag{13}$$

$$\mathfrak{B}_2 = \gamma B_y \sin \Theta \,. \tag{14}$$

Now, averaging over the whole trajectory, as $\bar{\zeta} = 0$ and $\int B_y \cos\Theta \, \mathrm{d}l = \int \boldsymbol{B}' \cdot \mathrm{d}\boldsymbol{l} = 0$, we find $\bar{\mathfrak{B}}_1 = 0$. Also $\bar{\mathfrak{B}}_2$ is proportional to the mean vertical focusing force on the particle and must also be 0.

Further, as $\bar{\zeta} = 0$, and there is no correlation between ζ and $\cos\Theta$,

$$\bar{\mathfrak{B}}_z = \gamma \bar{B}_z \left[1 + \bar{\zeta}^2 \left(\frac{1}{\gamma} - 1\right)\right] = \gamma \bar{B}_z \,, \tag{15}$$

the correction being less than 0.1 % and therefore negligible as $\zeta \leqslant 2°$.

The combined motion of the spin in the laboratory is therefore in the horizontal plane and relative to $\boldsymbol{p}$, a rotation about the z axis at frequency $\Omega_a = \gamma^{-1}\omega_0 \mathbf{a}\bar{\mathfrak{B}}_z = \mathbf{a}\omega_0 \bar{B}_z$; plus the oscillations of the Michel frame about two horizontal axes which are too small to affect the measurement. We conclude, therefore, that eq. (7) is valid for our experiment.

1·2.2. Effect of electric dipole moment. If the muon has an electric dipole moment $f \cdot e\hbar/mc$, the precession frequency of the spin would be altered ([16]) by the factor $\{1 + 4\beta^2 f^2/\mathbf{a}^2\}^{\frac{1}{2}}$, leading to an error in the determi-

([16]) R. L. GARWIN and L. M. LEDERMAN: *Nuovo Cimento*, **11**, 776 (1959).

nation of **a**. This effect has been discussed in a separate paper ([17]) in which, by looking for a storage-time-dependent vertical component of the polarization, we have shown that $f \leqslant (3 \pm 6) \cdot 10^{-5}$. It follows that the error introduced in the measurement of **a** is less than 0.5 %.

As, however, f is expected to be zero from considerations of time reversal invariance ([18]), we do not include this uncertainty in the error estimates reported below for our measurement of **a**.

1·2.3. Average over the ensemble of muons. So far we have considered only one muon, but the spin direction can be measured accurately only as an average over an ensemble of muons. The probability of counting a decay electron in a direction defined by unit vector $\boldsymbol{k}$ is

$$\mathrm{d}P/\mathrm{d}\Omega = 1 + \boldsymbol{k} \cdot \boldsymbol{A} \,, \tag{16}$$

where $\boldsymbol{A}$ is a vector of length equal to the asymmetry parameter and with direction parallel to the muon spin. Summing over the ensemble of m muons, the decay electron count n_k recorded in direction $\boldsymbol{k}$ is

$$n_k = m \Delta\Omega \left[1 + \boldsymbol{k} \cdot \left(\frac{1}{m} \sum \boldsymbol{A} \right) \right] . \tag{17}$$

The vector $(1/m) \sum \boldsymbol{A}$ defines the muon spin direction and overall asymmetry parameter for the ensemble. This can in principle be measured with any desired accuracy by increasing the number of muons considered, thus increasing the statistical accuracy of the angular distribution n_k.

In the case of muons of the storage magnet consider the ensemble of the muons which all have storage time t. Summing eq. (7) over all muons in this ensemble we obtain

$$\theta(t) - \theta_t(0) = \mathbf{a} \omega_0 \bar{B}_t \cdot t \,, \tag{18}$$

where $\theta(t)$ is the mean polarization angle (*) after storage; $\theta_t(0)$ is the mean initial polarization angle for this group of muons (the subscript t labelling the ensemble is necessary because muons stored for a different time may have different initial conditions and different initial polarizations); $\bar{B}_t$ is the mean

---

([17]) G. CHARPAK, F. J. M. FARLEY, R. L. GARWIN, T. MULLER, J. C. SENS and A. ZICHICHI: *Nuovo Cimento*, 22, 1043 (1961).

([18]) L. LANDAU: *Nucl. Phys.*, 3, 127 (1957).

(*) By the mean of an angle we always imply the vector mean as defined above: this is not exactly the same as the arithmetic mean angle, but the difference is negligible for a small angular spread.

field for the ensemble, it is an average over the time in the magnet and over the different trajectories that contribute to storage time t; again the subscript t indicates a possible dependence of $\bar{B}$ on t.

This is the fundamental equation for the experiment, but it will be further developed in Sect. 7·1 to include a number of important experimental corrections. The steps necessary to measure **a** will now be described; namely, the setting-up of the storage field and the measurement of t and $\bar{B}_t$, the preparation of the input beam and the determination of the correctly weighted mean initial polarization angles $\theta_t(0)$, and, finally, the measurement of the final polarization angle $\theta(t)$.

2. – Theory of storage system.

2·1. *Outline of method.* – The problem in designing a magnet for storing muons for $\sim 10^3$ turns is to find a field shape which allows the particles to be efficiently injected, stored and finally ejected. Long-time storage and efficient ejection are directly contradictory requirements and are made more difficult by the necessity to know the magnetic field to ~ 0.1 % along the trajectory.

As the total path lenth in the magnet is ~ 1 km, vertical focusing is essential. Since it is impossible by Liouville's theorem to inject the particles into a fixed orbit in a static magnetic field, like that of our magnet, a gradient field is used which causes the quasi-circular orbit to « walk » slowly along the long axis of the magnet, in a direction transverse to the gradient, see Fig. 1.

Muons of 150 MeV/c momentum, formed by forward decay in flight of pions in the CERN Synchro-cyclotron, are injected and fall on a beryllium moderator Be. They emerge with momentum ~ 90 MeV/c and the orbit, now of radius ~ 19 cm, remains wholely inside the magnetic field. The orbit displacement along the x axis (distance s per turn=*step-size*) allows the particles to miss the moderator after one turn and to continue down the magnet. Clearly only the muons emerging from the first s centimetres at the edge of the moderator can be stored. In the injection region the step-size is ~ 2 cm per turn. In the central section of the magnet the field gradient is small, reducing the step-size to ~ 0.4 cm per turn, and the muons spend a long time in this region. Finally, a transition is made to the ejection region where a large gradient gives step-size ~ 12 cm per turn bringing the particles rapidly across the end of the magnet with the result that they are ejected from the field.

2·2. *Orbits in an almost-uniform magnetic field.* – The approach to the design of the magnetic field was twofold:

i) analytic; from a general parametrized field of what seemed heuristically to be a useful symmetry, the important measurable quantities are

deduced — drift rate of particle orbit (storage time), vertical focusing, and storage-time distribution; specific values of the parameters were then chosen, bearing in mind intensity, size of required magnet, cost, and minimization of certain errors introduced into the measurement by scattering, etc;

ii) numerical; for specific values of the parameters the particle trajectories are studied by point-by-point integration of the differential equation through the entire storage system. This numerical work established the validity of the analytical methods. The ejection could not be treated analytically since the magnetic field varies too greatly and too sharply in that region. The possibility of ejection was established by the numerical calculations and the field designed from these results.

In the median plane of the storage region of our magnet the field $B_z(y)$ is uniform in x, but varies with y. In the median plane, $z = 0$, the field has only a z-component; for $z \neq 0$, $B_y \neq 0$.

Consider first the motion of a charged particle whose position and velocity lie in the median plane. We shall prove that its motion is a secular drift in x, plus a periodic motion in x and y. The drift in x per period is defined as the step-size. The study of the stability of the orbit with respect to z leads to a derivation of the « vertical » (z) focusing wavelength which is important in design of the magnet for nonzero intensity. From these two quantities the storage-time distribution and the magnet phase-space is computed, and the magnet field shape is designed by appropriate choice of parameters.

Since the accuracy of our knowledge of the mean magnetic field over the orbit (*) must be greater than the desired precision of the measurement of **a**, we limit our discussions to fields which depart only slightly from uniformity. Most of the results will be derived only to first order in $(B - B_0)/B_0$; however, since the particles will make very many turns in the fields, we are obliged to prove the exact validity of two fundamental theorems: constancy of energy and absence of a « transverse drift » in the storage field. Some of our results proved only to first order are in fact true *to all orders* (which does not, of course, mean that they are exactly true). For the proofs to all orders and a discussion of adiabatic invariants, we refer the reader to the extensive literature developed in relation to cosmic rays and to the containment of particles for the production of controlled thermonuclear reactions (**). Since we are con-

---

(*) It should be noted that an alternative possibility of measurement exists. Instead of measuring $\Delta\theta$, $\overline{B}$, and t as required by eq. (7) one can make use of the equally true integral $\Delta\theta = a\gamma\varphi$, where $\gamma \equiv (1-\beta^2)^{-\frac{1}{2}}$ and φ is the angle through which the momentum vector has turned. Such investigations were carried out by the group and by others, extending as far as a 20-turn prototype « SCREW » magnet. Accurate knowledge of γ and φ would be required for a precision measurement.

(**) For a recent review see T. G. NORTHROP: *Rev. Geophys.*, **1**, 283 (1963).

cerned with almost-uniform fields, we may obtain many of the results by a simple perturbation approach which is at once both compact and physically satisfying.

THEOREM A. – *In a static magnetic field, the kinetic energy of a charged particle is an absolute invariant of the motion* (neglecting radiation effects).

PROOF. – The Lorentz force is

$$\boldsymbol{F} \equiv \dot{\boldsymbol{p}} = \frac{e}{c}\,\boldsymbol{v}\times\boldsymbol{B}\,. \tag{19}$$

Since

$$\frac{\mathrm{d}E}{\mathrm{d}t} = \boldsymbol{F}\cdot\boldsymbol{v} = \frac{e}{c}\,\boldsymbol{v}\cdot\boldsymbol{v}\times\boldsymbol{B} \equiv 0\,,$$

the particle energy and $|p|$ itself are constant throughout the motion.

THEOREM B. – *In a field of the form* $\boldsymbol{B} = \boldsymbol{k}B_z(y)$ *in the median plane* ($z = 0$), *and with*

$$B_z(y) > 0\,, \tag{20}$$

($\boldsymbol{i}$, $\boldsymbol{j}$, $\boldsymbol{k}$ *are unit vectors along* x, y, z *axes*), *the particle co-ordinate* $y(t)$ *is strictly periodic in* t *and has a period less than* $2\pi\gamma mc/eB_{\min}$, *where* $B_{\min}$ *is the smallest value of* B_z *in the vicinity of the orbit.*

PROOF. – Note that $\Theta \equiv \mathrm{tg}^{-1}(p_y/p_x)$ increases continuously with time. [From eq. (19) we have $\dot{\Theta} = (e/mc\gamma)B$.] Thus $\dot{\Theta} > (e/mc\gamma)B_{\min}$, and the time for Θ to change by 2π is $T < 2\pi mc\gamma/eB_{\min}$. By considering the motion over the interval $-\pi < \Theta < \pi$, we shall show that y is strictly periodic in t and that x has, in addition to a part periodic in t, a secular increase with t. Since we wish to exhibit different behaviour of x and y, it is profitable to write eq. (19) in component form:

$$\begin{cases} \ddot{x} = \dfrac{e}{m\gamma c}\,\dot{y}\,B_z(y) = \omega_1\,\dot{y}\,B_z(y)\,, \\ \ddot{y} = \dfrac{-e}{m\gamma c}\,\dot{x}\,B_z(y) = -\,\omega_1\,\dot{x}\,B_z(y)\,, \end{cases} \tag{21}$$

where $\omega_1 \equiv e/m\gamma c$.

For the origin of time corresponding to $\Theta = 0$ and $\dot{y} = 0$, one has a very simple symmetry property: the eqs. (21) are invariant under $x \to -x$ and $t \to -t$. Thus $y(t) = y(-t)$ and $\dot{y}(t) = -\dot{y}(-t)$. If at some time $t = T/2$, $\dot{y} = 0$ and $\Theta = \pi$, then at $t = -T/2$, $\dot{y} = 0$, $\Theta = -\pi$. Thus if $T/2$ is the min-

imum time to have $\dot{y}$ again zero, T is a candidate for the period of $y(t)$. That the motion is indeed periodic with period T follows immediately, since at the two times $t = -T/2$, $t = +T/2$ we have $\dot{y} = 0$, $y(-T/2) = y(T/2)$, so $\dot{x}(-T/2) = \dot{x}(+T/2)$ from theorem A. Also $x(T/2) = -x(-T/2) \equiv s/2$.

Since y, $\dot{y}$, $\ddot{y}$ and $\dot{x}$ have indentical values at $t = \pm T/2$, the y-motion obtained by integrating the two second-order differential equations (21) will be identical in every period T. [x does not enter explicitly since $B = B(y)$.] In each such interval of time x will increase by s (the step-size).

Thus we see that the particle will shift uniformly in x but will have *no* secular drift in y.

We now leave the realm of exact proofs and derive results good to first order in $f(y)$ where

$$B_z(y) = B_0[1 + f(y)], \qquad f(y) \ll 1. \tag{22}$$

As commented above, some of these results have been shown to be *adiabatic invariants* and so to have more general validity.

2·2.1. Perturbation calculation of step-size. Consider the unperturbed system to be a particle of momentum p and charge e, but with field equation (22) with $f(y) = 0$. For this unperturbed case the solution of eq. (19) or eq. (21) is well known to be

$$\left| \begin{array}{l} x = \varrho_0 \sin(\omega t) \\ y = -\varrho_0 \cos(\omega t) \\ \dot{z} = v_z = \text{const}\,, \end{array} \right. \tag{23}$$

with $\varrho_0 \equiv cp/eB_0$ and $\omega \equiv eB_0/m\gamma c$, where p and γ refer to the motion in the x,y plane. Thus the unperturbed motion is a helix. To the desired approximation we obtain the effect of the perturbing field by exhibiting the response of the unperturbed system to the introduction of the magnetic nonuniformity $B_0 f(y)$ as a perturbation.

We are guaranteed by theorem B that the secular response can be only a shift in x with step-size s centimetres per turn.

2·2.2. Step-size. We may now proceed to calculate the step-size by a perturbation treatment of (*) eq. (19)

$$\dot{\boldsymbol{v}} = \frac{e}{mc\gamma}\, \boldsymbol{v} \times \boldsymbol{B}(y) \tag{24}$$

(*) As above, $\hat{\imath}, \hat{\jmath}, \hat{k}$ are unit vectors along x, y, z axes.

with

$$\boldsymbol{B}(y) = \hat{\boldsymbol{k}} B_0[1 + f(y)] \tag{25}$$

$$\boldsymbol{v}(t) = \boldsymbol{v}_0(t) + \boldsymbol{v}_1(t) \tag{26}$$

$$\boldsymbol{v}_0(t) = |v_0|[\hat{\boldsymbol{i}} \sin \omega t + \hat{\boldsymbol{j}} \cos \omega t] . \tag{27}$$

$\boldsymbol{v}_0(t)$ is the unperturbed circular motion $[f(y) = 0]$. Equation (24) now reads:

$$\dot{\boldsymbol{v}}_0 + \dot{\boldsymbol{v}}_1 = \frac{e}{mc\gamma} (\boldsymbol{v}_0 + \boldsymbol{v}_1) \times \hat{\boldsymbol{k}} B_0[1 + f(y)] ,$$

and suppressing the unperturbed equation and the product of the small quantities $\boldsymbol{v}_1 f(y)$, we have

$$\dot{\boldsymbol{v}}_1 = \frac{eB_0}{mc\gamma} [(\boldsymbol{v}_0(t) \times \hat{\boldsymbol{k}} f(y)) + (\boldsymbol{v}_1 \times \hat{\boldsymbol{k}})] . \tag{28}$$

Integrating eq. (28) over a period of the unperturbed motion we have for the $\hat{\boldsymbol{j}}$ component

$$\hat{\boldsymbol{j}} \cdot \int_0^T \dot{\boldsymbol{v}}_1 \, \mathrm{d}t \equiv \hat{\boldsymbol{j}} \cdot [\boldsymbol{v}_1(T) - \boldsymbol{v}_1(0)] \simeq 0 = - \frac{eB_0}{mc\gamma} \left[\int_0^T v_{0z} f(y) \, \mathrm{d}t + \int_0^T v_{1z} \, \mathrm{d}t \right] . \tag{29}$$

In eq. (29) the $\int_0^T \dot{\boldsymbol{v}}_1 \mathrm{d}t$ would be zero if the new period T' in the perturbed field were the same as the old. Since the change of period is at most first order in f, as is $\boldsymbol{v}_1$ itself, this integral is $0(f^2)$ and is dropped. Also

$$\int_0^T \boldsymbol{v}_1 \, \mathrm{d}t \equiv \boldsymbol{s}$$

to first order, and we know by theorem B that $\boldsymbol{s}$ has only an x-component. Thus eq. (29) becomes

$$s = - \int_0^T v_{0z}(t) f(y) \, \mathrm{d}t = - \oint_0 f(y) \, \mathrm{d}x_0 = - [f(y) x_0(t)]_0^T + \oint_0 x_0 \frac{\partial f(y)}{\partial y} \, \mathrm{d}y$$

as a result of integration by parts. Since $x_0(t)$ indicates the unperturbed motion, we have finally

$$s = \oint_0 \frac{\partial f(y)}{\mathrm{d}y} x_0 \, \mathrm{d}y = \frac{\partial}{\partial y} \oint_0 \frac{B(y)}{B_0} x_0 \, \mathrm{d}y \tag{30}$$

or

$$s = -\oint_0 f(y)\,\mathrm{d}x = \frac{1}{B_0}\frac{\partial M_0}{\partial y_c}\,, \tag{31}$$

where $M_0 = \oint\int B(y)\,\mathrm{d}x\,\mathrm{d}y$ = flux through the unperturbed orbit.

Equation (31) relates the step-size along x to the rate of change of flux with y_c through the unperturbed circular orbit as its centre y_c is moved in y. By an obvious generalization of eq. (31) we have, to first order in f,

$$\boldsymbol{s} = -\frac{1}{B_0}\,\boldsymbol{k}\times(\nabla M_0) \tag{32}$$

which would be useful for fields of lower symmetry in the median plane. Thus in general $\boldsymbol{s}\cdot\nabla M_0 = 0$ and the orbit centre moves along the contour lines of flux. So to first order, $\partial M_0/\partial t = 0$, the orbit moves in such a way as to preserve constant flux through a circle the size of the unperturbed orbit. It would be difficult to define more accurately than to first order in f the flux through the perturbed orbit; consideration of the motion of particles through static magnet fields of form slowly varying in space shows that the flux is an *adiabatic invariant, i.e.* in situations in which it may be accurately defined, all the coefficients are zero in its power series expansion in space-frequency of the magnetic field variations.

Let us now specialize to a field of the form

$$B = B_0(1 + ay + by^2 + cy^3 + dy^4 \ldots)\,. \tag{33}$$

Equation (31) gives

$$s_0 = \pi\varrho_0^2[a + \tfrac{3}{4}c\varrho_0^2 \ldots] = \pi\varrho_0^2 a_{\mathrm{eff}}, \tag{34}$$

with $a_{\mathrm{eff}} \equiv a + \frac{3}{4}c\varrho_0^2$ for an orbit with $y_c = 0$ and an unperturbed radius ϱ_0. An orbit with centre at y_c will have

$$s = \pi\varrho_0^2[a + \tfrac{3}{4}c\varrho_0^2 + 2by_c + 3dy_c\varrho_0^2 \ldots] \tag{35}$$

all to first order in f.

In a field parametrized in the manner of eq. (33), it is clear that the step-size for orbits central in the magnet is determined by a and c and that b and d may be chosen for other reasons. We shall show that b provides the main vertical focusing for the particles. Evidently eq. (34) implies a very strong dependence of step-size on orbit radius (particle momentum). This may be much

reduced to zero if desired by an appropriate choice

$$c = -\frac{2}{3}\frac{a}{\varrho_0^2}. \tag{36}$$

We later make a slightly different choice for c in order to reduce the spread in storage time rather than the spread in number of turns. Such choices for c incidentally reduce the maximum amount of iron required for shimming to a given step-size.

2·2.3. Vertical focusing. We can calculate the vertical focusing to first order in f by considering the possibility of z-components of the velocity $\boldsymbol{v}$. With $\boldsymbol{v}(t) = \boldsymbol{v}_0(t) + \hat{\boldsymbol{k}} v_z(t)$, $v_z \ll v_0$, and $\boldsymbol{B} = \hat{\boldsymbol{k}} B_0[1 + f(y)]$ for $z = 0$, $f(y) \ll 1$, the z component of eq. (24) reads:

$$\dot{v}_z(t) = \frac{e}{mc\gamma} v_x B_y . \tag{37}$$

However,

$$B_y = \frac{\partial B_y}{\partial z} z = -\frac{\partial B_z}{\partial y} z$$

so that

$$\dot{v}_z(t) = -\frac{e}{mc\gamma} v_x \frac{\partial B_z}{\partial y} z . \tag{38}$$

On the assumption that $f(y) \ll 1$, we may integrate eq. (38) over a period of the unperturbed orbit, thus ignoring the periodic terms in the Fourier expression of

$$v_x \cdot \frac{\partial B_z}{\partial y} .$$

The result is, if we put $z = z_0 \exp[i\omega_z t]$

$$-\omega_z^2 z_0 T = -\frac{e}{mc\gamma} z_0 \oint_0 v_z \frac{\partial B_z}{\partial y} \, \mathrm{d}t \tag{39}$$

or

$$\omega_z^2 = \frac{e}{mc\gamma T} \oint_0 \frac{\partial B_z}{\partial y} \, \mathrm{d}x . \tag{40}$$

Integrating by parts, we find

$$\lambda_z^{-2} = \frac{\omega_z^2 T^2}{4\pi^2 \varrho_0^2} = \frac{Te}{4\pi^2 \varrho_0^2 mc\gamma} \left[\left(\frac{\partial B_z}{\partial y} x \right)_0^T - \oint_0 x \frac{\partial^2 B_z(y)}{\partial y^2} \, \mathrm{d}y \right] . \tag{41}$$

In the bracket of eq. [41], the first quantity is zero while the second is the second derivative of the flux through the unperturbed orbit with respect to y_c.

Thus,

$$\lambda_z^{-2} = -\frac{1}{2\pi \varrho_0^2 B_0} \oint\oint \frac{\partial^2 B_z(y)}{\partial y^2} \, \mathrm{d}x \, \mathrm{d}y = -\frac{1}{2M_0} \frac{\partial^2 M_0}{\partial y_c^2} . \tag{42}$$

Equation (42) gives the vertical weak focusing wavelength in terms of an integral of $\partial^2 B_z(y)/\partial y^2$ over the area of the unperturbed orbit, or equivalently in terms of the second derivative of the flux through that circle. Comparison with eq. (31) shows that

$$\lambda_z^{-2} = \frac{1}{2\pi \varrho_0^2} \frac{\partial s}{\partial y_c} . \tag{43}$$

This is an important general result which shows that a field configuration which has no variation of step-size s with orbit-position y_c will also have no focusing.

The formulae (31) and (42) in terms of the derivatives of the orbit flux are useful not only as mnemonics; but also in determining experimentally the orbits in an existing magnet, in the following manner. A disc-shaped coil the diameter of the orbit to be investigated, is placed in the magnet with its centre coincident with the initial position of the orbit. A ballistic galvanometer or other voltage integrator is attached to the terminals of the coil (fluxmeter). The centre of the disc may be moved along the trajectory of the orbit centre by moving the disc in such a direction that the flux change is zero. In practice, one makes a flux map of the magnet with this device by moving it in x and then draws the contour lines on the flux map. The procedure is much easier and more reliable than the characterization of the field by point-by-point Hall plate measurements. These measurements are reported in Sect. 3·2. The same flux coil can, of course, be used to measure the vertical focusing wavelength λ_z, according to eq. (42).

2·2.4. Storage time. For a magnet of useful length D, the storage time, *i.e.* the time required for the orbit to drift from one end to the other, is

$$t = \frac{D - 2\varrho}{s} \cdot \frac{2\pi m\gamma c}{eB} , \tag{44}$$

with s given by eq. (35).

Particles leaving the injection assembly (assumed at $y = 0$) at angle Φ to the y axis (see Fig. 2) have

$$y_c = \varrho_0 \Phi \,. \tag{45}$$

Thus t is a function of injection angle Φ and radius ϱ_0 through the corresponding terms in eq. (35) with eq. (45) and the γ term in eq. (44) ($D \gg 2\varrho$ is assumed). By differentiation one finds

$$\frac{\mathrm{d}t}{t} = (\beta^2 - A)\frac{\mathrm{d}\varrho}{\varrho} - B\,\mathrm{d}\Phi \,, \tag{46}$$

where $\beta = v/c$, and for $y_c = 0$

$$A = 2\,\frac{a + \frac{3}{2}c\varrho^2}{a + \frac{3}{4}c\varrho^2} \,, \tag{47}$$

$$B = \frac{2b\varrho + 3\,d\varrho^3}{a + \frac{3}{4}c\varrho^2} \,. \tag{48}$$

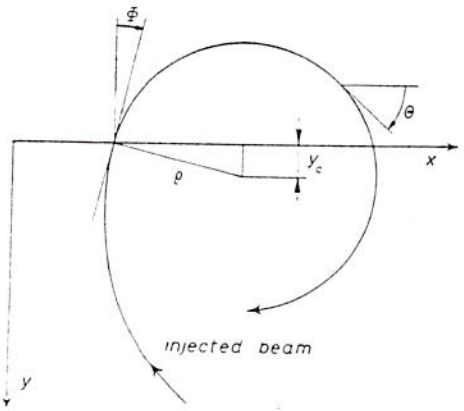

Fig. 2. – Co-ordinate system. x-axis, long axis of magnet, the pole extends from $x=0$ to $x=600$ cm; y-axis, horizontal transverse axis ($y=0$ along centre line of magnet); ϱ, orbit radius; Θ, orbit angle to x-axis; Φ, injection angle; y_c, y co-ordinate of orbit centre.

As already implied above, the variation of storage time with Φ (in effect y_c) cannot be cancelled without destroying the focusing; but the variation with ϱ (orbit momentum) can be eliminated over the design region by choosing c such that $A = \beta^2$. The importance of this choice in eliminating a certain source of error is discussed in Sect. 6·4.

2·3. *Orbit stability.* – For small values of $f(y)$, orbit stability is assured if $\lambda_z^{-2} > 0$. For $\lambda_z^{-2} < 0$ [eq. (42)] the vertical motion is unstable and exponential build-up occurs in the z co-ordinate. The situation is different for $f(y)$ not small. We are still assured by theorem B, however, that the orbit motion in the median plane retains the same general character. It is the oscillations in z which require a more careful treatment, since the neglect of the periodic focusing terms (« strong-focusing ») in eq. (39) is no longer justified. In fact, as $\partial^2 B_z/\partial y^2$ is made larger, the vertical motion becomes first more stable and then finally over-stable and blows up exponentially. This behaviour is not contained in our derivation of the weak focusing. For the ejection region we must use a large $f(y)$ and are therefore required to investigate the stability bands of the vertical motion.

Our only assumption in what follows is that z/ϱ_0 is small (*).

The fundamental equation is eq. (38), which can be rewritten

$$\ddot{z} = -\frac{e}{mc\gamma} V_z \frac{\partial B_z}{\partial y} z \,, \tag{49}$$

for which we investigate the stability in a field of the form eq. (22). Theorem B guarantees that the coefficient of z in eq. (49) is a periodic function of time with period T.

Rewriting eq. (49) as

$$\frac{\mathrm{d}^2 z}{\mathrm{d}\eta^2} + z g(\eta) = 0 \,, \tag{50}$$

where $\eta \equiv 2\pi t/T$ and $g(\eta)$ is a periodic function of η with period 2π, we see that we have a Hill differential equation, the stability and detailed properties of which must be investigated. It is readily shown that the entire problem may be solved by a single numerical integration of eq. (50) or eq. (49) over a period of the motion in the x-y plane. If one starts with $z(0)=0$, $z'(0) \equiv (\mathrm{d}z/\mathrm{d}\eta)\,(0)=1$, then, since in our problem $g(\eta) = + g(-\eta)$, it is easy to show that if

$$r \equiv z'(2\pi) \,, \qquad q \equiv r + (r^2-1)^{\frac{1}{2}} \equiv \exp[2\pi\omega]; \tag{51}$$

then

$$\omega \equiv \frac{1}{2\pi} \ln (q)$$

is the phase advance of the vertical oscillation per actual orbit period. For ω real we have a stop-band (unstable vertical motion). For ω pure imaginary the vertical oscillation is stable. It is easily seen that ω is always either pure real or pure imaginary.

At the two egdes of a pass-band $\omega = 0$ (*i.e.* $\omega = i\mu$, with $\mu = 0$ and 2π at the two edges of the band). Thus, $\mu = \pi$, $q = -1$ and $r = -1$ at the centre of a pass-band, corresponding to a half-cycle of the vertical oscillation per orbit turn. The numerical calculation also gives the Floequet factors (the detailed shape of the vertical oscillation). It can be shown that the maximum

---

(*) The problem of the stability of the orbit in a field $B = B_0(1 - ay + by^2)$ was solved analytically by W. K. H. PANOFSKY, CERN guest professor, who found the orbit motion and then investigated the stability of the resultant eq. (38) with x and y given as a function of time. Our investigations were carried out by the technique described in the text, which is useful for a field arbitrary y-dependence.

vertical deviation of the ray starting with $z = 0$ and dip angle 1 is less than

$$z_m = \frac{r}{\sin(2\pi\mu)} . \tag{52}$$

It can be shown also that an adiabatic or invariant of the vertical oscillation exists for slow changes in the characteristics of the strong-focusing field. If the vertical motion is at all times stable, then under gradual distortions of the field shape the quantity

$$\frac{z^2_{\max}(\sigma)}{z'^2(\sigma)} \tag{53}$$

is adiabatically constant. $z^2_{\max}(\sigma)$ is the actual maximum excursion of the orbit at the stage σ of the slow transformation of the vertical focusing. $z'(\sigma)$ is obtained from eq. (52) for the static state σ. The result of eq. (53) agrees in the case of weak focusing with the usual adiabatic result $z_{\max}\lambda_z^{-\frac{1}{2}} = \text{const}$.

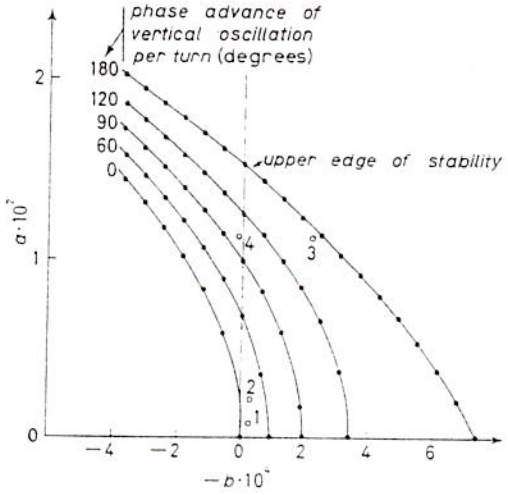

Fig. 3. – First stability band for vertical motion as a function of parameters a and b for field of form $B = B_0(1 - ay - by^2)$ computed for orbit radius $\varrho = 18$ cm. • computed point.

It should be noted that if $g(\eta) \neq g(-\eta)$, it is necessary to integrate two rays through a cycle of the x-y motion. Similar results then obtain.

These methods allow us to ensure that the vertical motion is stable under the design values of the field coefficients a, b, c ... to be described below. In particular, in the steep-gradient ejection region we found it necessary to have $b \sim 0$ to remain well within the stable region. This is clear from Fig. 3 which delineates the pass band in the (a, b)-plane for the parabolic field $B = B_0(1 + ay + by^2)$.

2·4. *Storage time, storage efficiency; transition fields.* – For a given value of B, if muons are stored for time t the effect to be measured [eq. (7)] is proportional to t, while the number of surviving muons $n = n_0 \exp[-t/\tau]$, assuming the ideal case of loss only by decay.

The statistical accuracy of the measurement is then proportional to

$t(n_0 \exp[-t/\tau])^{\frac{1}{2}}$, which has a maximum at $t = 2\tau \sim 5.5$ μs, allowing for time dilatation. So, other things being equal, an optimum design would centre around this storage time. Also, for the anticipated value of **a**, the precession curve of asymmetry *vs.* time crosses zero at 4 μs and 6 μs: in determining the precession frequency these points contribute most significantly to the precision. Therefore, remembering that a larger precession angle would also reduce systematic errors, we decided to optimize the storage system for 6 μs storage time, corresponding to about 1000 turns in a field of 16 kG.

In this section, the orbit theory of Sect. 2·2 will be used to answer the all-important question: suppose one designs a magnet large enough to hold 1000 turns, then will there be enough muons left after storage to be able to do a precision measurement on their spins? In the design stage of the experiment this question could be answered only in a semi-quantitative way, mostly because the structure of the beam when incident on the moderator was not sufficiently well known. Furthermore, the sequence in which the arguments are presented below is somewhat artificial: no one parameter is independent of any other and therefore frequent iterations are necessary to find suitable values. Short-cutting this procedure we shall at various points anticipate the final values and justify the choice by its consequences.

2·4.1 Choice of material for the moderator. In traversing the moderator, the phase-space volume of the beam increases, due to multiple scattering and broadening. For the multiple scattering the angle Θ_m in the moderated beam increases according to

$$\overline{\mathrm{d}\Theta_m^2} = \frac{(21.2)^2}{p^2\beta^2}\,\frac{\mathrm{d}x}{X_0}\,, \tag{54}$$

where p is the momentum in MeV/c, $\beta = v/c$. and X_0 is the radiation length in the moderator. Furthermore, the range R is given approximately for muons below 100 MeV by

$$R = CE^{\frac{7}{4}}\,, \qquad \mathrm{d}R = \tfrac{7}{4}\,CE^{\frac{3}{4}}\,\mathrm{d}E\,, \tag{55}$$

where E is the kinetic energy of the particle in MeV and C is a constant: for carbon and beryllium $C \approx 1/80$, for hydrogen $C \approx 1/160$, and for copper $C \approx 1/64$. For slow muons $p\beta \approx 2E$. Substituting eq. (55) into eq. (54) and inserting the radiation length, we have, after integration:

$$\overline{\Theta_m^2} = K(E^{-\frac{1}{2}} - E_0^{-\frac{1}{2}})\,, \tag{56}$$

with $K = 0.04$ for H_2, 0.16 for Be, 0.27 for C, and 1.48 for Cu. In addition

to the scattering there is also a broadening of the beam, which is given approximately for a moderator of length D by

$$\overline{r_m^2} \approx \frac{\overline{\Theta^2} D^2}{3} . \tag{57}$$

The phase-space added by the moderator to an initially perfect beam is

$$F_m = \pi r_m^2 \cdot \pi \Theta_m^2 . \tag{58}$$

For muons moderated from 70 MeV down to 37 MeV, the effect of various moderators is given in Table I.

TABLE I.

	ϱ	D (cm)	$\overline{\Theta_m^2}$	$\overline{r_m^2}$ (cm^2)	F_m (cm^2 rad^2)
Be	1.85	7.5	0.010	0.19	0.02
C	1.8	7.2	0.016	0.28	0.045
H_2	0.07	80	0.002	4.3	0.086
Cu	8.9	1.86	0.088	0.10	0.09

Beryllium was chosen as moderator material, since it degrades the beam quality the least.

2·4.2. Maximum storable fraction of the beam: phase-space limitations. To obtain efficient storage, angles and directions in the beam must as much as possible fall within the range of angles and directions that the storage system can hold. Prior to designing the magnet, data were therefore obtained on the beam-space volume. The size of the beam was measured by scanning horizontally and vertically with counters. To separate angular divergence from momentum dispersion in the horizontal plane, the scanning was done with a range telescope, thus keeping p and Δp fixed. The beam angles were obtained by scanning with a small counter at a fixed distance in front of the range telescope. By means of two quadrupole magnets the image can be given the desired shape. In particular the horizontal width could be reduced from ± 4.5 to ± 1.3 cm; this represents a considerable increase in the useful

TABLE II.

horizontal angle Θ_x	0.060 rad
horizontal width x	± 1.3 cm
vertical angle Θ_z	0.0175 rad
vertical width z	± 4.3 cm

fraction of the beam, as will become apparent below. Table II summarizes the data on the beam.

For the beam phase-space volume one finds, from the data in Table II:

$$F_0 = \pi x z \, \pi \Theta_x \Theta_z = \pi r_0^2 \, \pi \Theta_0^2 = 0.06 \text{ cm}^2 \text{ rad}^2 . \tag{59}$$

One can now combine F_m of eq. (58) and F_0 of eq. (59) to obtain the phase-space volume of the moderated beam:

$$F_{mb} = \pi(\overline{r_0^2} + \overline{r_m^2})\pi(\overline{\Theta_0^2} + \overline{\Theta_m^2}) = F_0 + F_m + \pi^2(\overline{r_0^2}\,\overline{\Theta_m^2} + \overline{r_m^2}\,\overline{\Theta_0^2}) . \tag{60}$$

F_m and F_{mb} have been tabulated in Table III for various values of the orbit radius in 16 kG field after moderation. The incident momentum is fixed at 150 MeV/c.

TABLE III.

ϱ (cm)	p (MeV/c)	F_m (cm² rad²)	F_{mb} (cm² rad²)	F_s (cm² rad²)	$f = F_s/F_{mb}$
12	58	0.3	1.87	0.0825	$4.4 \cdot 10^{-2}$
14	67	0.18	1.48	0.081	$5.5 \cdot 10^{-2}$
16	77	0.10	1.17	0.074	$6.3 \cdot 10^{-2}$
18	86	0.05	0.89	0.063	$7.1 \cdot 10^{-2}$
20	96	0.02	0.64	0.046	$7.2 \cdot 10^{-2}$
22	106	0.008	0.52	0.025	$4.8 \cdot 10^{-2}$
24	116	0.002	0.40	0	0

It is of interest at this point to see to what extent the phase-space of the moderated beam could have been reduced further by proper « matching » of the beam to the moderator, *i.e.* by introducing lenses so that

$$\frac{\overline{\Theta_0^2}}{\overline{r_0^2}} = \frac{\overline{\Theta_m^2}}{\overline{r_m^2}} . \tag{61}$$

In this case the moderated beam phase-space of eq. (60) is a minimum,

$$F_{mb}^{\min} = F_0 + F_m + 2\sqrt{F_0 F_m} . \tag{62}$$

For example, for $\varrho = 20$ cm, $\overline{r_m^2} = 0.19$ cm², $\overline{\Theta_m^2} = 0.010$ rad²; for the beam $\overline{r_0^2} = 5.6$ cm², $\overline{\Theta_0^2} = 0.0010$. Equation (60) then gives $F_{mb} = 0.64$ cm² rad², while eq. (62) results in $F_{mb}^{\min} = 0.15$ cm² rad². A factor 4 improvement could thus have been obtained in theory but was not possible because of physical limitations.

Next, we consider the storage system. The storage phase-space volume is given by:

$$F_s = \pi x z \, \pi \Theta_x \Theta_z ,$$

where x and z are the horizontal and vertical co-ordinates perpendicular to the direction of motion of the beam. x is given by the step-size in the storage region, $x = s/2$; z is determined by the gap height h, $z = h/2$; Θ_x is limited by the available width $2W$ of the magnet: $\Theta_x = (W - \varrho)/\varrho$; Θ_z is given by the vertical focusing $\Theta_z = h/2\hat{\lambda}_z$. Therefore

$$F_s = \left(\frac{\pi^2}{8}\right)\left(\frac{h^2 s}{\hat{\lambda}_z}\right)\left(\frac{W - \varrho}{\varrho}\right) . \tag{63}$$

We may express this in terms of the field parameters a, b by: $s = \pi\varrho^2 a_{eff}$ (for orbit centre at $y_c = 0$) and $\hat{\lambda}_z = 1/\sqrt{b}$:

$$F_s = \left(\frac{\pi^3}{8}\right)(a_{eff}\sqrt{b}\,h^2)\,\varrho(W - \varrho) . \tag{64}$$

Note that the effect of ϱ and of the field parameters can be considered independently. F_s clearly has a maximum at $\varrho = W/2$.

The maximum storable fraction of the beam f is determined by

$$f = \frac{F_s}{F_{mb}} , \tag{65}$$

with F_s from eq. (64) and F_{mb} from eq. (60). This ratio is a function of a, b, h, W, B, the magnetic field, the incident momentum p_0, the momentum after moderation p, and the lateral and angular spread of the incident beam. It is listed in Table III and plotted in Fig. 3 as a function of ϱ for certain values of a_{eff} and b. It is seen that although F_s has a maximum at 12 cm, the ratio f maximizes at $\varrho = 19$ cm since a larger residual momentum implies less deterioration of phase-space of the incident beam. The peaking of storage efficiency at 19 cm orbit radius is in excellent agreement with experiment. From eqs. (64) and (60) it is evident that the optimum value of ϱ is independent of a_{eff} and b.

So far we have omitted the spread in momenta as a factor in the storage efficiency, tacitly assuming that this spread is sufficiently small, so as not to give rise to a decrease in efficiency. The spread $\Delta p_0/p_0$ of the incident beam is $\pm 1.5\,\%$. As the range $R \propto p^{\frac{1}{2}}$

$$\frac{\mathrm{d}p}{p} = \mathrm{const} \cdot p^{-\frac{1}{2}} \mathrm{d}R ;$$

therefore, after slowing down from momentum p_0 to p we have

$$\frac{\Delta p}{p} = \left(\frac{p_0}{p}\right)^{\frac{1}{2}} \frac{\Delta p_0}{p_0} . \tag{66}$$

For example, for p_0=150 MeV/c, p=90 MeV/c ($\varrho = 19$ cm), $\Delta p/p = \pm 9\,\%$. For a design radius of 19 cm we thus expect a band of radii ranging from 17 to 21 cm; from the F_s/F_{mb} curve in Fig. 4 it is seen that this decreases the efficiency by less than 5 %. This factor can thus be neglected.

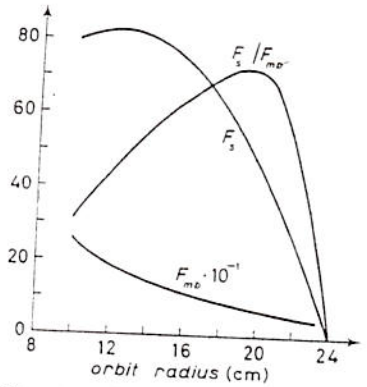

Fig. 4. – Phase-space volume *vs.* orbit radius. F_s for storage magnet, curve *a*. F_{mb} for moderated beam available for injection, curve *b*. The optimum orbit radius $\varrho = 19$ cm corresponds to the maximum value of F_s/F_{mb}, curve *c*.

2·4.3. Injection and ejection. Equation (65) gives an upper limit to the stored intensity. Two comments are in order: first, there is no point in making F_s larger than F_{mb} (indeed, it would require a very large magnet to make F_s even equal to F_{mb}); second, whatever F_s, it is only the fraction of F_s overlapping with F_{mb} that contributes to the efficiency.

In Fig. 5 we have plotted the horizontal and vertical projection of the various phase-space volumes involved. It is seen that for the chosen values of the storage parameters (see Sect. 2·5) there is a strong mismatch between F_{mb} and F_s in the horizontal projection. To improve the overlap Θ_x^{stor} could be made smaller and x^{stor} larger, keeping the product constant; to obtain complete overlap $x^{\text{stor}} = s^{\text{stor}}/2$ must increase by a factor ~ 3. This would require a magnet of ~ 20 m length. The alternative solution is to construct a special injection field, with phase-space F_i which overlaps with F_{mb}. This field must satisfy the conditions $x_i < x_{mb}$, $\Theta_{x_i} < \Theta_{x_{mb}}$, $\Theta_{x_i} x_i = \Theta_{x_s} x_s$. In a transition region which connects the injection field to the storage field, the phase-space is deformed adiabatically, the angle increases and the linear dimension decreases, always keeping the product constant, until the storage field configuration is reached. This second solution was adopted. The chosen injection phase-space is indicated in Fig. 5. Its area, F_i, is equal to F_s. In the vertical projection this opportunity does not arise since the storage phase-space is almost completely included within the phase-space of the moderated beams.

From conservation of phase-space for the stored beam before and after the transition it follows that

$$\Delta y_c^{\text{inj}} s^{\text{inj}} = \Delta y_c^{\text{stor}} s^{\text{stor}} . \tag{67}$$

This is another illustration of the fact that the orbits move along contour

lines of the magnetic flux (see Sect. 2·2). Now Δy_c^{stor} is restricted by the width of the magnet to

$$\Delta y_c^{stor} = W - \varrho,$$

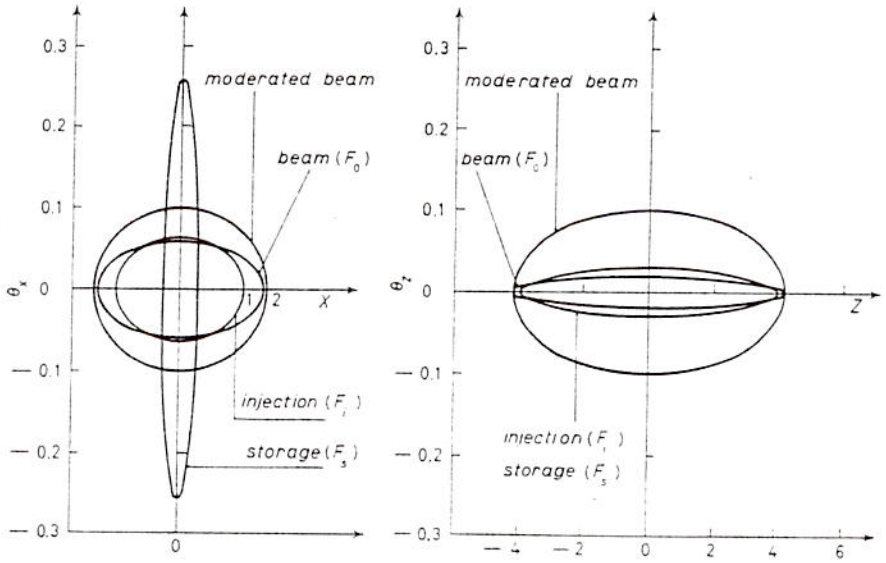

Fig. 5. – Horizontal and vertical phase-space diagrams for *storage* and *injection* regions of the magnet, and for the moderated beam available for injection. This shows how the efficiency is improved by using a special injection region to give a better match to the available beam.

and thus with eq. (67) the useful width of the injection region is

$$\Delta y_c^{inj} = (W - \varrho)\frac{s^{stor}}{s^{inj}}, \tag{68}$$

which means that only a fraction s^{stor}/s^{inj} of the total available width $(W - \varrho)$ in the injection region contains particles that are not lost in the transition.

In an exact design one would thus arrange the moderation and incident energy such that the moderated beam would just fill the available Δy_c^{inj} from eq. (68). However, in practice we have $\Theta_x^{mb} > \Theta_x^{inj}$ or equivalently $\Delta y_c^{mb} > \Delta y_c^{inj}$ and some loss will occur. Let us call

$$\frac{\Delta y_c^{inj}}{\Delta y_c^{mb}} = r\,.$$

Then the fraction lost is $1 - r$. The loss sets in as soon as Δy_c grows beyond $\Delta y_c = r(W - \varrho)$ when going through the transition region. It may be noted, however, that in referring the storage efficiency directly to the ratio of the

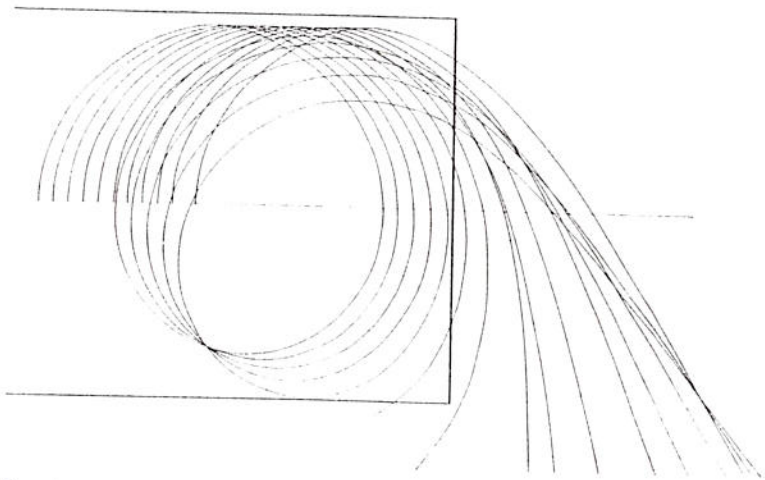

Fig. 6. – Computed orbits at the ejection end of the magnet based on detailed field measurements with the iron block (Fig. 61) in position. The downward movement in the last turn is due to the falling off of the field at the end of the magnet; but this actually improves the ejection by bringing the orbit away from the corner post of the vacuum chamber.

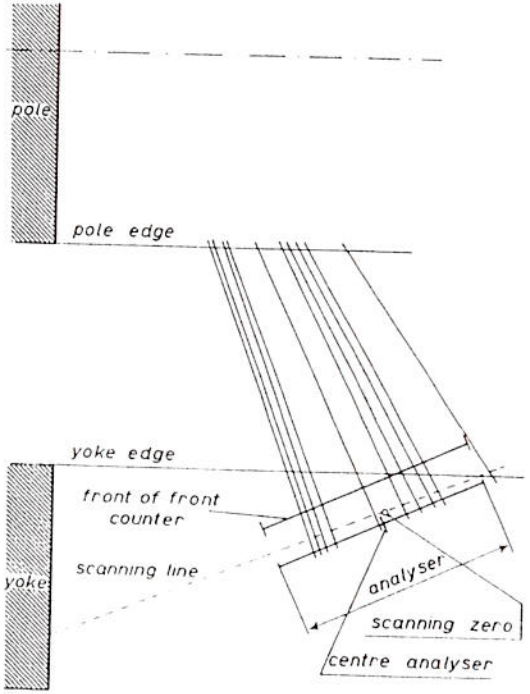

Fig. 7. – Trajectories of ejected muons as established by floating wire technique. One end of the wire was fixed in the centre line of the magnet at various values of x, and was required to leave this point perpendicular to the x-axis. The iron block (Fig. 61) partially shields the ejected particles from the fringing field and brings the trajectories further away from the yoke. The optimum shape was established empirically by the floating wire method to maximize the flux falling on the analyser.

storage phase-space to the moderated beam phase-space, as was done in eq. (65), no such loss factor enters.

A higher intensity is injected into the injection region but the extra particles are spilled out of the magnet sideways in going through the transition.

Having completed a sufficient number of turns the muons must now be extracted. This requires a special ejection field for the following qualitative reason. In any gradient field the particle orbit drifts in a direction perpendicular to both the field and its gradient. At the edge of the magnet the fringing field adds a strong x-gradient to the locally present y-gradient. The orbit will then drift in a direction perpendicular to the resultant gradient. The x-gradient at the edge is of the order 10^{-1}/cm. If the very weak storage gradient (of order 10^{-3}/cm) were maintained all the way to the edge of the magnet, then the orbit would drift along the edge at the end, turn by 90° at the corner and follow the side edge back to the injection side! Computer calculations show that this is indeed the case for weak y-gradients near the end of the magnet. Therefore a transition is made to a very strong gradient, $a^{\text{ejection}} = 1.2 \cdot 10^{-2}$/cm, which gives a step-size $s^{\text{ejection}} \sim 12$ cm. Orbit tracing by the computer then shows a good ejection efficiency. A consequence of this increase in gradient is a narrowing of the band of orbit centres Δy_c by the factor $s^{\text{ejection}}/s^{\text{stor}}$ just the reverse of what happens in the transition region between injection and storage. As shown in Sect. 2·3, a larger value of a would have made the vertical motion unstable, and in fact in this region we make $b \sim 0$ to remain well within the stability band. Figure 6 shows computed ejection trajectories: trajectories established with floating wire on the final magnet are given for comparison in Fig. 7.

2·5. *Numerical values of the field parameters.* – The storage efficiency is proportional to $a_{\text{eff}}\, b^{\frac{1}{2}}$, as can be seen in eq. (64). For a given percentage spread in step-size due to the injected range of y_c, eq. (35) shows that b can be increased proportionally to a_{eff}. Hence stored intensity $I \propto a_{\text{eff}}^{\frac{3}{2}} \propto s^{\frac{3}{2}}$; thus for a given number of turns a longer magnet is more efficient. The precision in $(g-2)$ for a fixed number of turns is proportional to $n^{\frac{1}{2}}$ where n is the total number of analysed muons; hence for a given precision $L^{\frac{3}{2}}T$ is constant where L is the length of the magnet and T the data-taking time. In fact, every argument shows that L should be as large as possible: therefore we chose $L = 6$ m as the maximum length for which one can conveniently make coils. We shall see below that this leads to an efficiency of several per cent and a reasonable running time for a 0.4 % experiment.

Of the 6 m, about 2 m are occupied by the injection and ejection fields and the corresponding transitions, which contribute ~ 0.5 μs to the storage time. To store for an additional 5.5 μs in the remaining 4 m, a step-size of $s = c\tau/t = 0.44$ cm is required. Since $s = \pi\varrho^2 a_{\text{eff}}$, we have, for $\varrho = 19$ cm, $a_{\text{eff}} = 3.9 \cdot 10^{-4}$ cm^{-1}.

The value of a_i, the linear gradient term in the injection region, is found from eq. (67) and the size of the moderated beam. Requiring $\Theta_x < \Theta_{x_{mb}} = 0.1$, we have from eq. (67)

$$s_i > 10 s_s \Theta_{x_s}$$

$$s_i > 10 s_s \frac{W - \varrho}{\varrho} = 1.2 \text{ cm}$$

for $W = 24$ cm (*i.e.* the useful width of the magnet), $\varrho = 19$ cm, and $s_s = 0.44$ cm. In particular, as seen in Fig. 4, the acceptance phase-space will be nicely centred inside the phase-space of the moderated beam if we choose $s_i = 2$ cm, leading to $a_i = 17 \cdot 10^{-4}$ cm^{-1}. The ejection gradient term, a_e, was made as large as possible. It was verified by ray-tracing in the computer that ejection would be achieved.

The quadratic term in the field b can, in principle, have the same value throughout the magnet, except in the ejection field where focusing is entirely provided by the linear term (see Sect. 2·3). We have seen in eq. (64) that the stored intensity goes as $\sqrt{b}$, hence b should be large; on the other hand, increasing b implies increasing the spread in storage times. This can be shown most easily by referring to eq. (35), from which it follows that

$$\Delta s = 2\pi\varrho^2 b \, \Delta y_e = \pi\varrho^2 \cdot 2b\Delta y_e \,. \tag{69}$$

Also the storage time

$$t \sim \frac{x\tau}{s} \text{ which implies } st = \text{const} \,. \tag{70}$$

To obtain an estimate of the desired value of b, suppose we wish to store muons for times ranging from 2 to 8 μs, centred at 5 μs. For $\varrho = 19$ cm, $\tau = 6$ ns, the average step-size in 400 cm is ~ 0.5 cm, if $t = 5$ μs. For 2 μs $s = 1.2$ cm; for 8 μs $s = 0.3$ cm; the spread $\approx \pm 0.45$ cm. In eq. (69) we then have, since $\Delta y_e = W - \varrho = 5$:

$$b = \frac{\Delta s}{2\pi\varrho^2 (W - \varrho)} = 3.9 \cdot 10^{-5} \text{ cm}^{-2} \,. \tag{71}$$

In fact we chose $b = 3.4 \cdot 10^{-5}$ cm^{-2}.

The value b must not only satisfy the criteria of storage efficiency and spread in storage time, but also be consistent with the requirements of stability with respect to vertical motion. The Hill equation describing the vertical motion has been discussed in Sect. 2·3. From the plotted stability bands of Fig. 3 it is clear that the limits on b set by the stability requirement are wider than those set by the desired spread in storage time. Equation (71) gives, therefore, the correct design value for b.

The « c term » in the field has already been discussed in Sect. 2·2. From eq. (46) we obtain $c \approx 1.3 \cdot 10^{-6}$ cm^{-3}. It cancels the momentum-dependence of the storage time.

2·6. *Predicted time distribution of stored muons.* – As already mentioned, the step-size s can be obtained by integrating over one orbit loop [cf. eq. (31)],

$$s = B_0 \varrho_0 \int_0^{2\pi} \frac{\sin \Theta}{B(y)} \, \mathrm{d}\Theta \,, \tag{72}$$

where the field $B(y)$ is to be computed at $y = \varrho_0 \sin \Theta$. This allows the step-size to be evaluated for any arbitrary field shape. Using the actual measured storage field one obtains the results shown in Fig. 8 which gives s as a function of orbit radius, and y_c the position of the orbit centre.

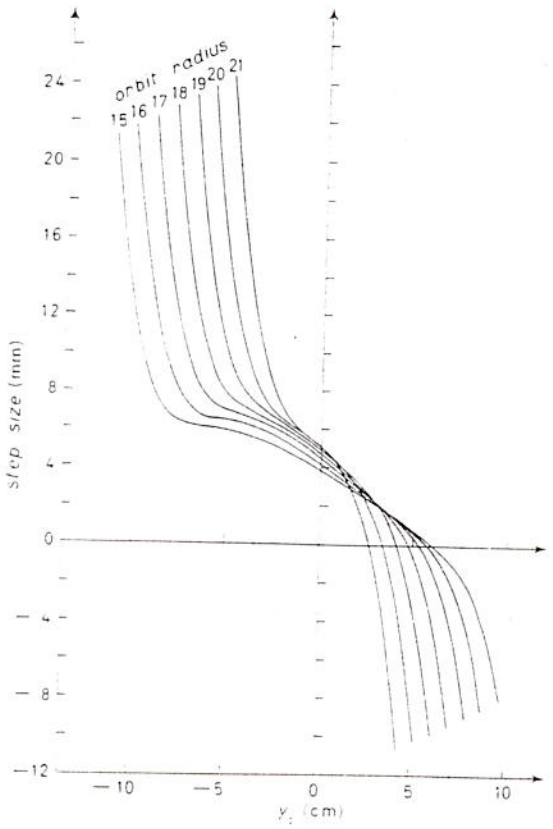

Fig. 8. – Step-size *vs.* orbit centre y_c for various orbit radii (cm), computed for the measured storage field using eq. (72).

In general around $y_c \sim 0$ there is a region where s varies linearly with y_c, corresponding to a field of parabolic form. At the extremes, however, the orbit starts to run partially into the fringing field and s varies more rapidly. Note that according to Sect. 2·2 eq. (43), the slope of the curve at any point determines the strength of the vertical focusing.

To calculate the expected time distribution of stored particles, one notes that to a good approximation the injection system distributes the orbit centres uniformly in y_c, while the corresponding storage time t is given by eq. (44).

Calculating for 1 cm steps in y_c, one allocates equal

numbers of muons to the corresponding intervals of t. This number is then corrected for muon decay, and for the small variation of injected intensity with y_c expected from the scattering distribution in the beryllium block.

A typical result is given in Fig. 9 calculated for $\varrho = 18$ cm. The reason for the double-peak structure is as follows. Wherever the range Δt of t, corresponding to $\Delta y_c = 1$ cm, is small there will be a concentration of particles in this range of time, and there will be a peak. For $y_c \ll 0$, s is large and t is small, so Δt is small also; this gives the first peak. Around $y_c = -3$ cm ds/dy_c has a minimum so Δt is again small; this gives the second peak. In general, a storage system of this type will always tend to give a two-peak distribution because there will usually be a minimum value of ds/dy_c.

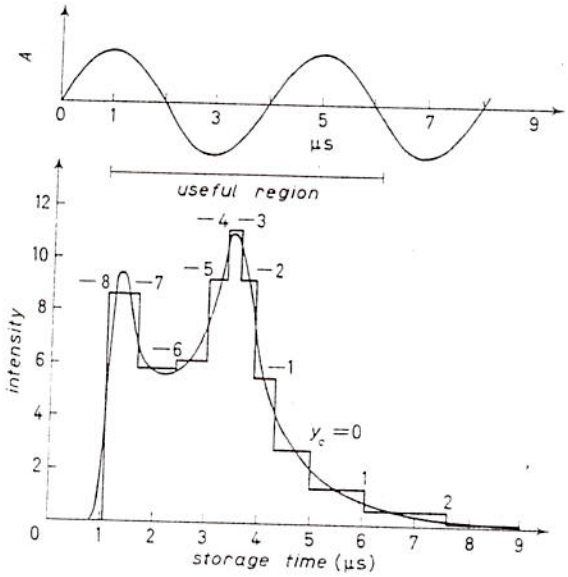

Fig. 9. – Ejected intensity *vs.* storage time computed from Fig. 8 for radius = 18 cm. To be compared with experimental results Fig. 50. The upper curve is the predicted $(g-2)$ precession curve. Orbit radius 18 cm.

As will be seen below, the experimental storage-time distribution is very similar to this prediction (see Fig. 50).

3. – Realization of storage system.

3·1. *Construction of the pole profiles.*

3·1.1. y-dependence. As we have seen in Sect. 2·2 we need a magnetic field of polynomial form [eq. (33)] in order to store muons for ~1000 turns or more. We also need an « injection » field and an « ejection » field. Moreover, it is necessary to connect these fields, which have amongst them different magnetic parameters [by magnetic parameters we mean the coefficients a, b, c, d in eq. (33)] and this means that we also need « transition » fields. In Table IV we show the values of the magnetic parameters obtained for these various fields.

The most important field to be constructed with great precision is clearly the « storage » field. The muons have to spend most of their time in this field, and irregularities in the desired field shape have to be reduced to the minimum if we want to keep maximum stored intensity. As already mentioned, the contour lines of the field must run straight down the magnet: otherwise the orbits will jitter sideways and particles will be lost. We will consider the « storage » field in some detail, the others only briefly. In order to have a more quantitative idea of the difficulties involved in the construction of a field of the form eq. (33) it is necessary to remember (see Sect. 2·5 and Table IV) that the choice of the magnetic parameters has led us to values for a, b, c, d such that the variations of the magnetic field in the storage region are of the order of 0.05 % per cm; consequently, the measuring apparatus has to be

TABLE IV. – *Magnetic parameters for the various fields.*

	x	a 10^{-4} cm^{-1}	b 10^{-5} cm^{-2}	c 10^{-6} cm^{-3}	d 10^{-7} cm^{-4}
Injection	30	17.0	— 4.0	0	0
Storage	420	7.1 (a_{eff} = 3.9)	— 4.0 (— 3.4)	— 1.3	0.2
End of storage	480	8.4 (a_{eff} = 6.7)	— 4.0 — 4.0	— 0.68	0
1) Ejection trans.	487.5	14.0 (a_{eff} = 15)	— 4.4 (b_{eff} = 4.0)	+ 0.4	+ 0.2
2) Ejection trans.	503.5	43.0	— 5.0	0	0
3) Ejection trans.	518.5	74.5 (a_{eff} = 71.0)	— 5.0	— 1.4	0
4) Ejection trans.	533.5	—	—	—	—
Ejection	570	125.0 (a_{eff} = 114)	— 18.0 (b_{eff} = + 0.8)	— 4.6	+ 3.8

The values of $\left.\begin{matrix} a_{eff} \\ b_{eff} \end{matrix}\right\}$ are computed for 18 cm radius:

$$a_{eff} = a + 243c$$

$$b_{eff} = b + 483d$$

N.B.: When zero appears for the value of « d » it has to be understood as being less than $1 \cdot 10^{-7}$ cm^{-4}.

sensitive and stable preferably to a level five times better, which means to one part in ten thousand. The problem is therefore not only to construct a field of polynomial form eq. (33), but also to measure it with sufficient accuracy.

The procedure used in shimming the magnet was to express the shape of the shims in polynomial form, the gap height H of the magnet being

$$H = H_0(1 - a'y - b'y^2 - c'y^3 - d'y^4) , \tag{73}$$

where the coefficients a', b', ... are called mechanical parameters. Far away from the fringing fields one expects the required a', b' to be about the same as the parameters a, b, ... which define the field shape. Near the edges of the magnet, however, the shims must be built up largely by trial and error and the final shape cannot be expressed in the simple form eq. (73), using the same parameters over the whole range of y. To avoid this difficulty we parametrized the shims according to eq. (73) independently for the inner region $|y|<19$ cm, and for the outer region $|y|>19$ cm.

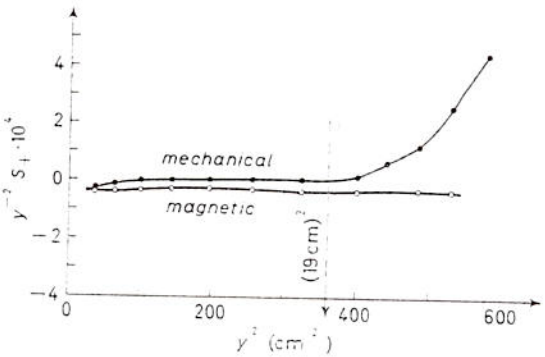

Fig. 10. – Determination of field parameters b and d. The symmetric component of the field shape $y^{-2}S_+$ is plotted *vs.* y^2. The intercept determines b and the slope determines d.

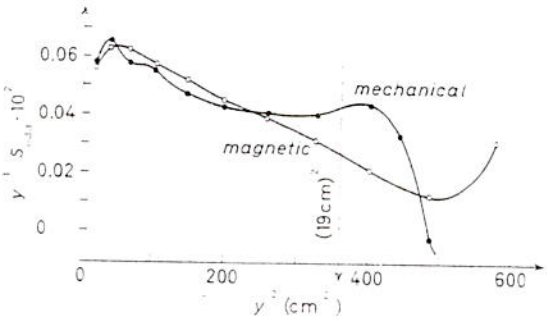

Fig. 11. – Determination of field parameters a and c from the odd component of field shape $y^{-1}S_{\text{odd}}$. The intercept determines a and the slope determines c.

To deduce the field parameters a, b, c and d from a given set of measurements one forms the sums $S_+(y) = B(y) + B(-y) - 2B(0)$ and $S_-(y) = B(y) - B(-y)$. By plotting $y^{-2}S_+$ against y^2 one should obtain a straight line determined by b and d (Fig. 10). Similarly the graph of $y^{-1}S_-$ *vs.* y^2 (Fig. 11) determines a and c.

To achieve the necessary accuracy in gap width (~ 0.07 mm per cm in y is the desired slope), and to allow for several trials, it was decided to build up the whole field shape by shimming. Any attempt

to realize the desired field by accurate machining of solid pole-pieces would have led to endless difficulties.

The magnet was shimmed with sheets of Armco-iron ($\mu = 1000$) with

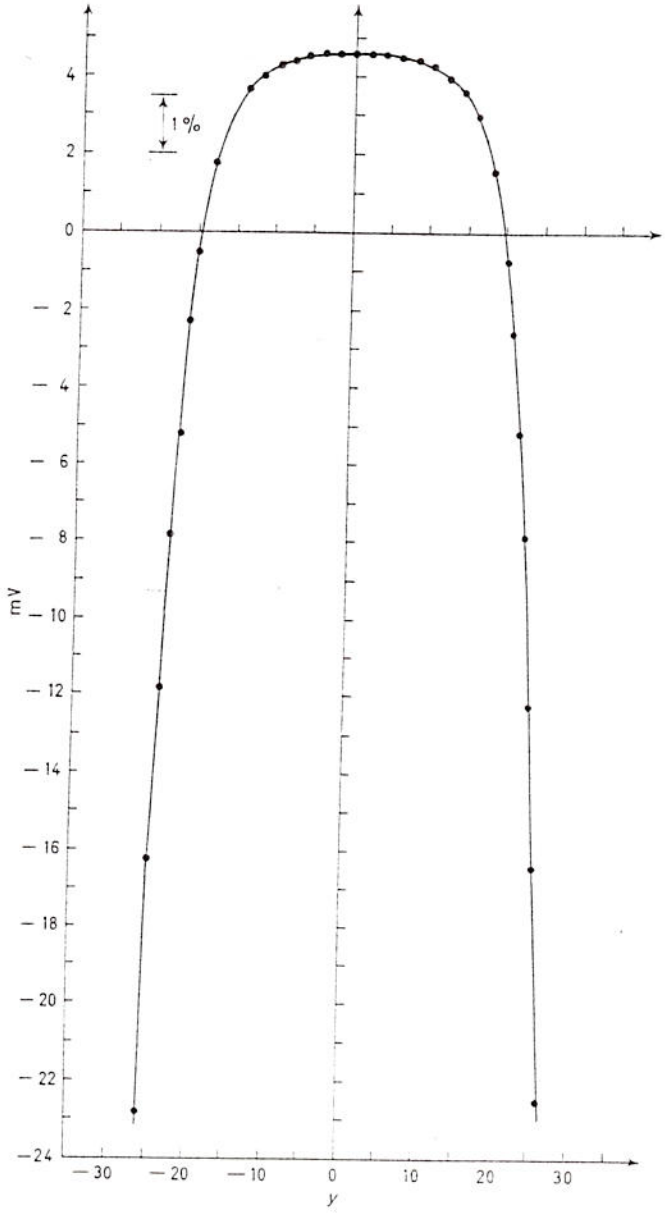

Fig. 12. – Field shape *vs.* y for the unshimmed magnet. The zero of the millivolt scale of Hall voltage is arbitrary.

thicknesses varying from 0.03 mm to 5 mm. By combining them in such a way as to have the profile of the poles with the desired shape [polynomial form eq. (73)], we were able to construct in three successive approximations the magnetic field desired. Figure 12 shows the shape of the magnetic field without any shimming. In Fig. 13 the shape of the « storage » field obtained after shimming is shown. In Fig. 14

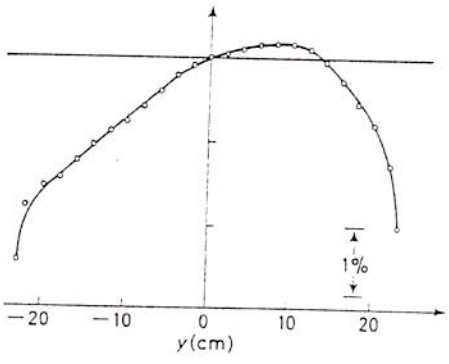

Fig. 13. – Final field shape in *storage* region measured at $x=350$ cm. Storage field at $x=350$.

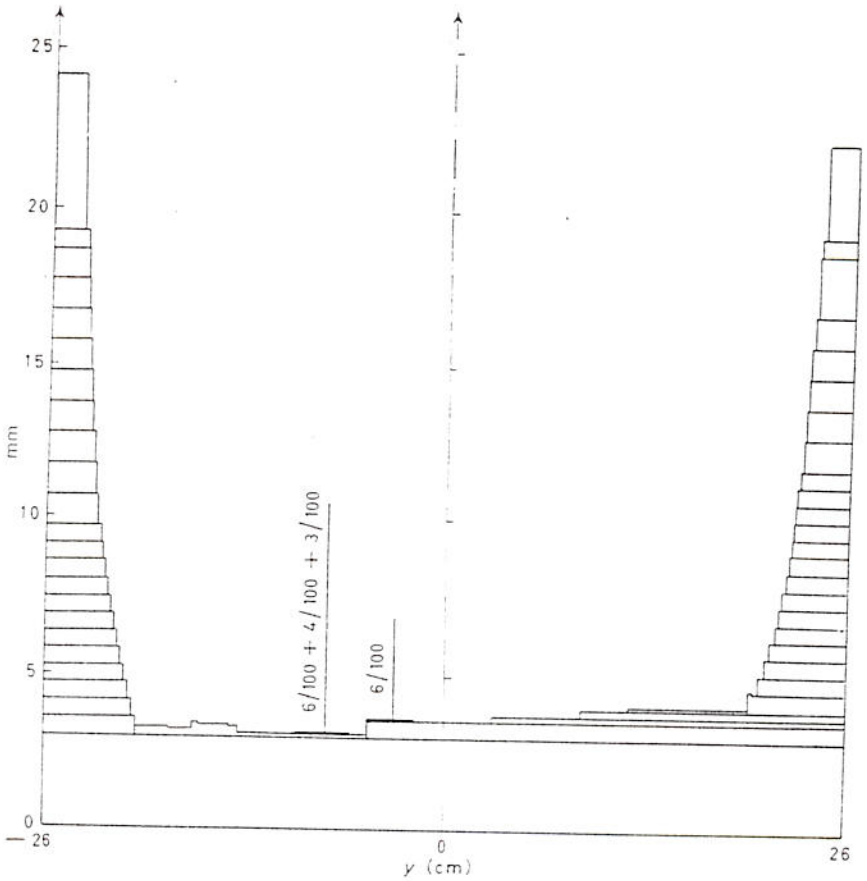

Fig. 14. – Shim heights in millimetres, required to produce the storage field of Fig. 13.

we see the corresponding profile of the pole pieces. As mentioned above, this profile has been obtained after three successive approximations.

Notice that the final field shape has always been obtained by correcting the value of the « mechanical » parameters in the two above-mentioned regions and not by introducing local corrections (which would have corrected the field locally but destroyed its shape outside the region where the correction had been applied).

Following the same principles, we have constructed the « injection » field and the « ejection » field. The injection field is connected to the « storage » field by joining the shim shapes of these two fields in a continuous way over the region of 30 cm in x separating these two fields. The storage field has

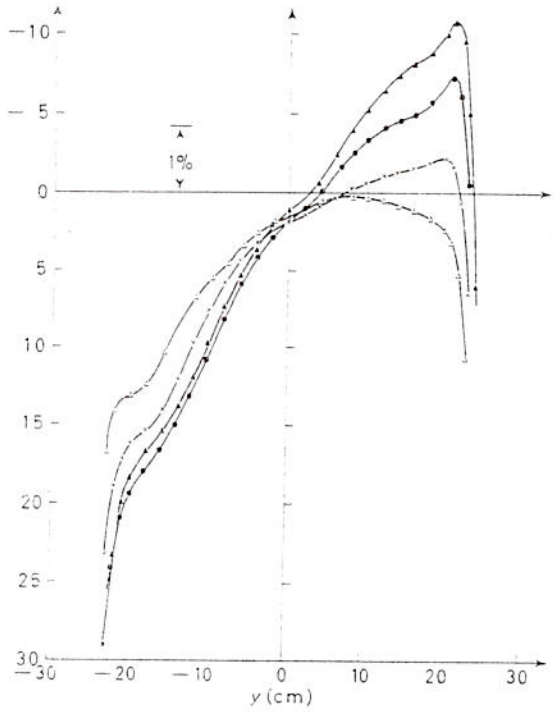

Fig. 15. – *Injection* fields at various values of x, showing gradual transition from the steeper injection gradient to the storage field in Fig. 13.

been connected to the ejection field by the use of four intermediate fields with magnetic parameters chosen by interpolating in the region of separation (60 cm in x) between the two extreme sets of values characteristic of the « storage »

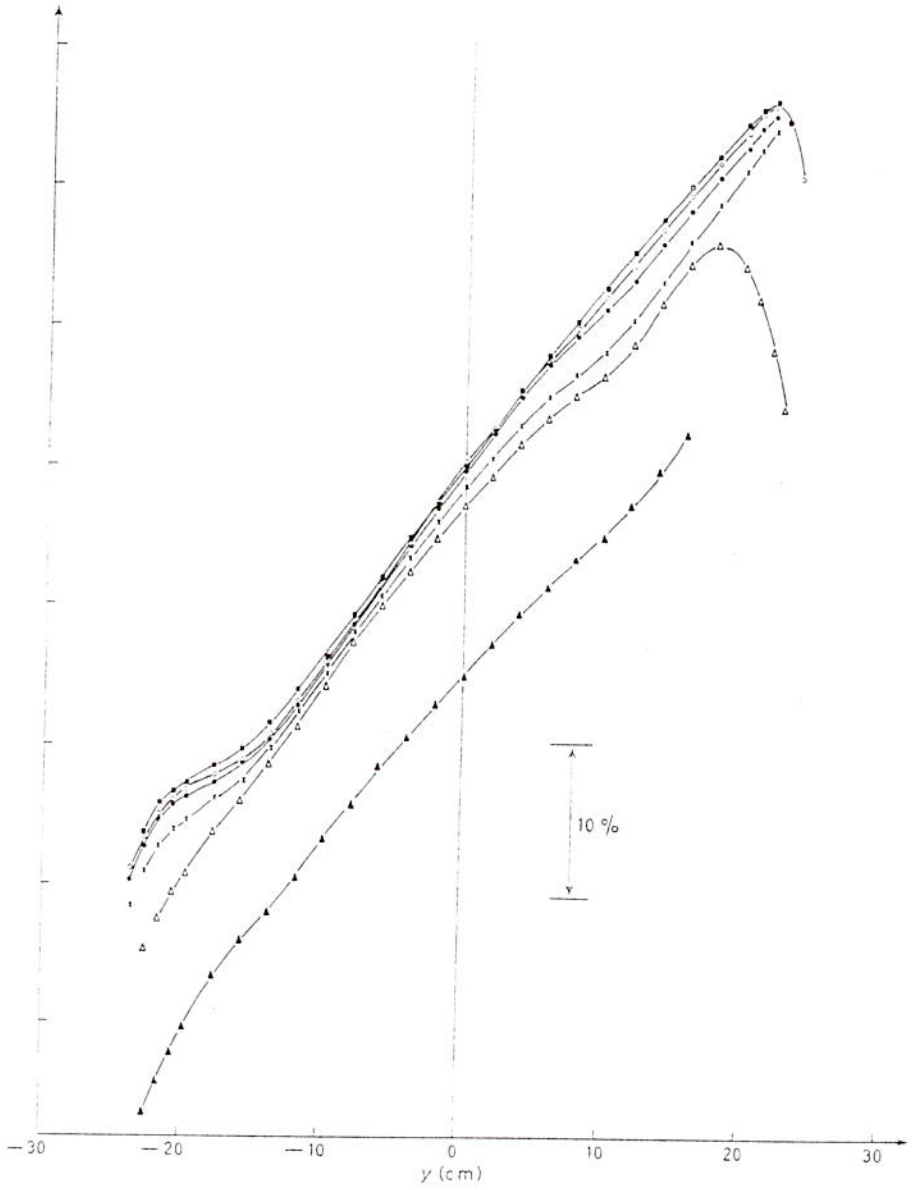

Fig. 16. – *Ejection* field at various x showing the inevitable decrease of field level at the end of the magnet ($x=600$). To obtain good ejection it is essential to maintain the field for as long as possible, and to maintain the gradient. From the constant-flux theorem it is clear that at $x=590$, for example the orbit would move over only ~ 1 cm in y_c, an acceptably small sideways drift. (Cf. Fig. 6.)

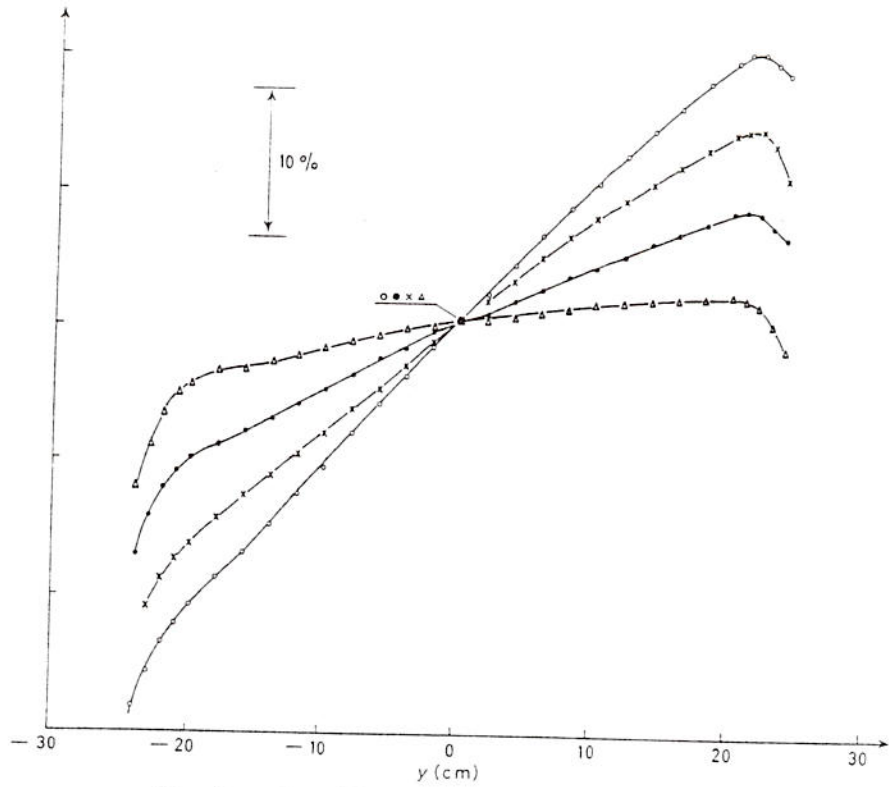

Fig. 17. – Transition fields from storage to ejection.

and the « ejection » fields; in Figs. 15 to 19 there are the various field shapes (injection, ejection and transitions) and some of the corresponding shim pro-

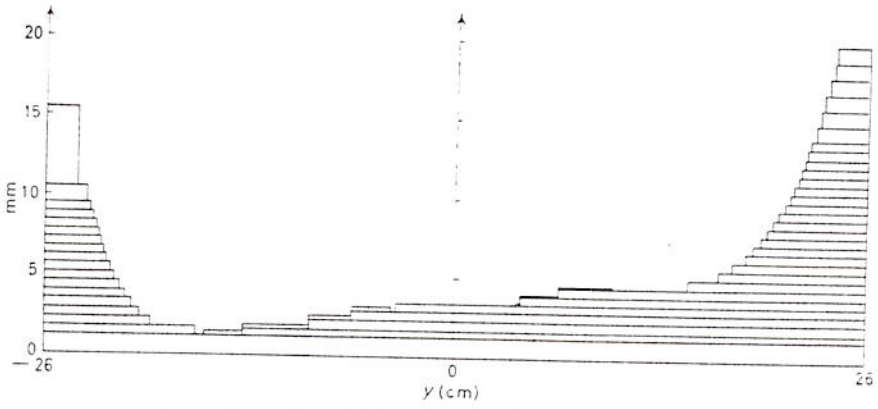

Fig. 18. – Shim heights required for injection field.

files. So far we have assumed that the magnet is perfect and infinite along the x axis, and we have only discussed the y-dependence of the field.

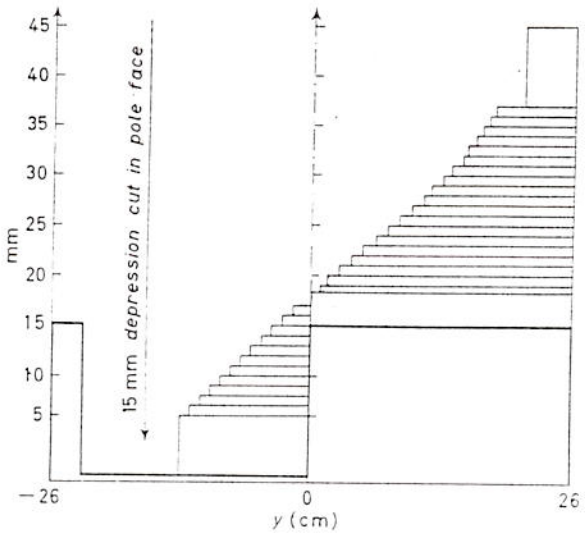

Fig. 19. – Shims for ejection field. In order to establish the desired gradient while maintaining the field constant at $y=0$, it was necessary to cut away iron from the pole face on the weak-field side.

3·1.2. x-dependence. The magnet presents some irregularities along the x axis and its dimensions along x are finite (6 m). This means that we have

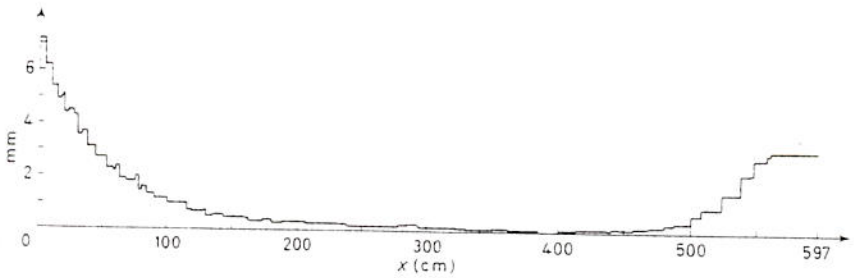

Fig. 20. – Shims required to correct the x-dependence of the field. This was necessary to prevent sideways wandering (parallel to y-axis) of the orbits. The x-dependence of the field is shown in Fig. 28, but the final x-corrections were determined from the flux-coil measurements.

to correct « locally » along x in these regions of the magnet where we measure the irregularities; moreover, we have to correct the two ends of the magnet

for the natural fall-off of the field. The x-correction has been done by making local corrections, using sheets of iron of suitable thicknesses, and the overall x-corrections are as shown in Fig. 20.

3·1.3. The perturbation due to the injection channel. An $(y\text{-}x)$ perturbation is introduced in the injection region by the iron channel used to shield the incoming particles from the fringing field of the magnet. The position and actual dimensions of the injection channel with respect to the

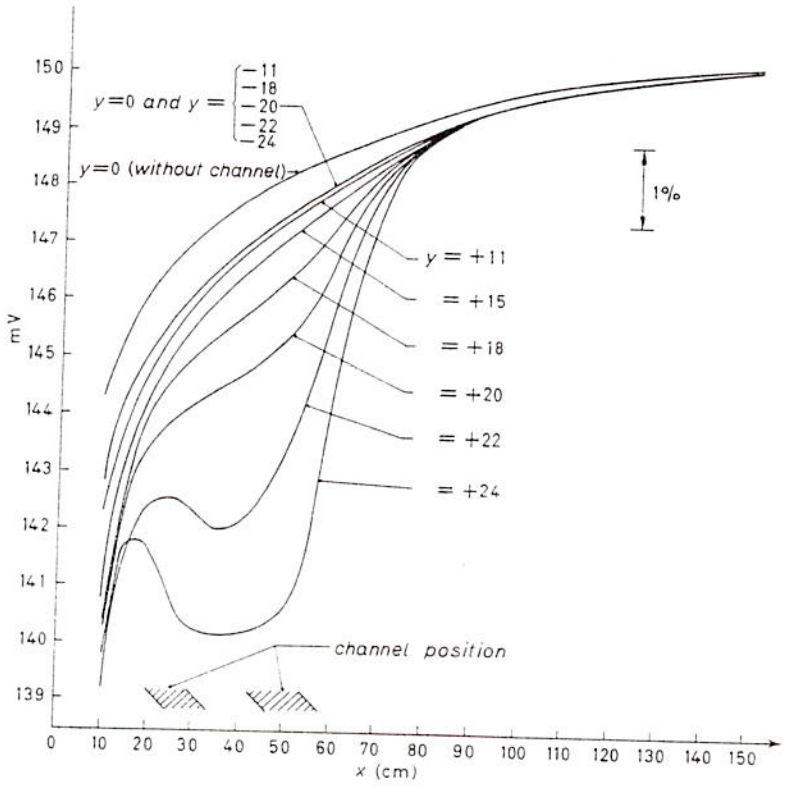

Fig. 21. – Local perturbation of field by the iron shielding channel used for the injected beam.

magnet can be seen in Fig. 1. The function of this channel is to reduce the magnetic field in the region outside the magnet gap in order to minimize the bending of the injected beam. For this reason it is necessary to bring this channel as close as possible to the pole pieces. The resulting perturbation in the field can be seen in Fig. 21. The shims necessary to correct for this perturbation along x and y are shown in Fig. 22.

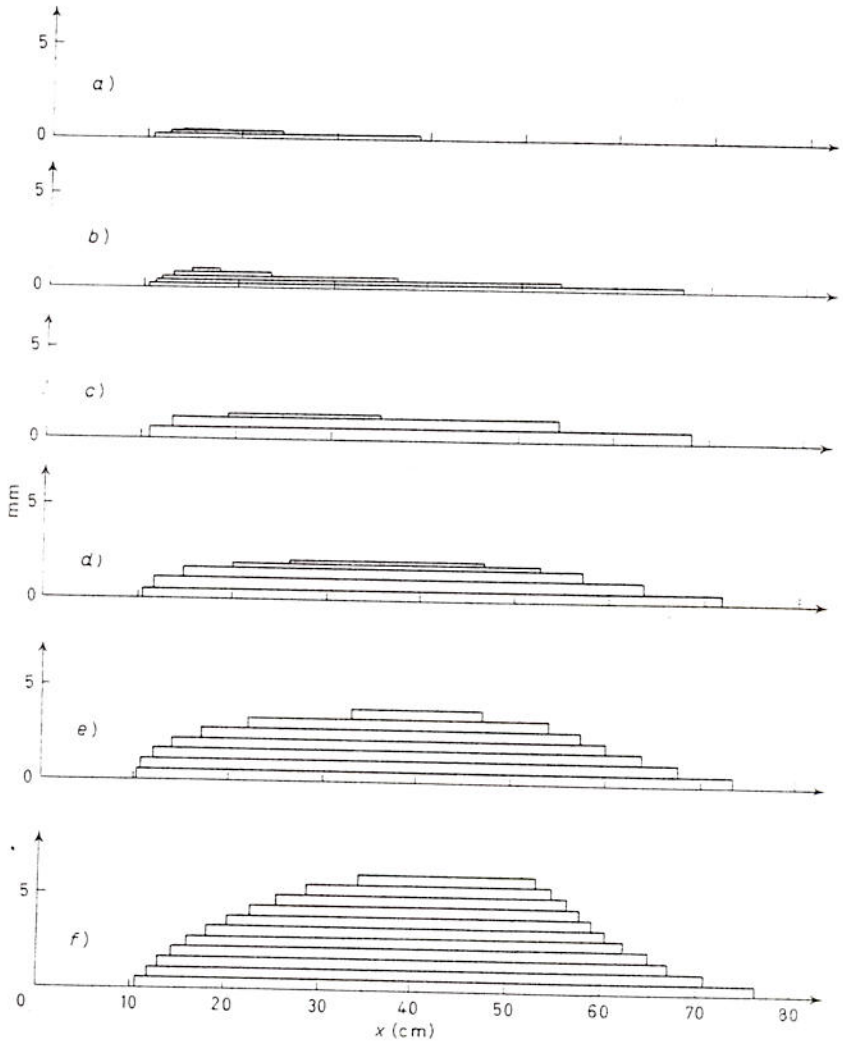

Fig. 22. – Local corrections to compensate for the effect of the injection channel (see Fig. 21).

3·1.4. Magnet facilities. Before closing this section on the construction of the desired magnetic fields, it is necessary to mention two details concerning our electromagnet.

i) The top and bottom poles terminate in 5 cm thick removable pole pieces (see Fig. 23). These pole pieces ($5 \times 52 \times 600$ cm^3) can be taken out from the magnet gap; this allows us to screw onto them the various shims needed. In Fig. 24 is shown a picture of the magnet with the 5 cm pole pieces

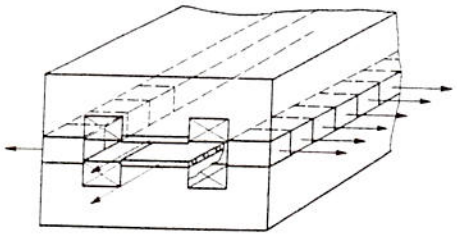

Fig. 23. – Overall view of the magnet showing the removable iron blocks ($20 \times 20 \times 31$ cm^3) in the yokes, and the removable top and bottom pole pieces (5 cm thick). To remove the poles the lower pole was first raised by hydraulic jacks via vertical push rods passing through the lower half of the magnet. An assembly of rollers was then introduced below this pole, and finally the upper and lower poles were rolled out of the magnet together onto a special table also equipped with rollers. Arrows indicate those parts of the magnet which can be taken out.

out from the gap; it is also possible to distinguish the shims mounted, held down by copper plates all along the 6 m length.

ii) Both yokes of the magnet are made, in the central region of the vertical plane, of iron blocks ($20 \times 20 \times 31$ cm^3) which can be taken out. This

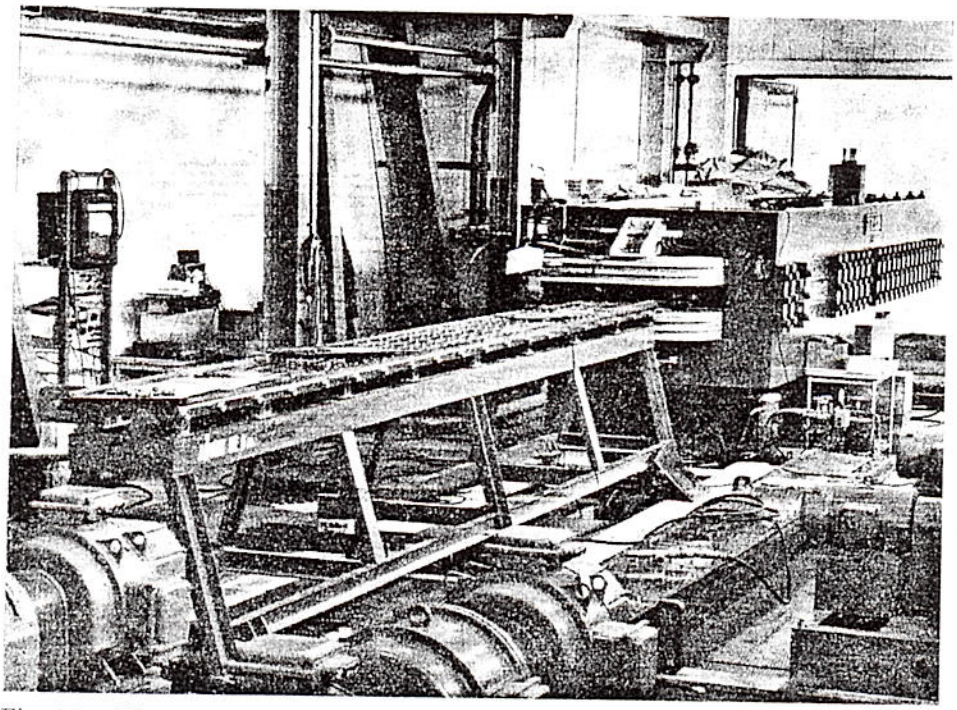

Fig. 24. – The magnet during the shimming operations, with injection shims removed for changes. In the foreground one sees the lower pole lying on the rollers of the special table. The shims are finally held in position by copper plates secured by brass bolts. The rollers at the side of the pole are for supporting the side plate of the vacuum chamber. The upper pole is on the floor in the right foreground, and behind this one sees one of the hydraulic jacks for lifting the poles with associated oil pump.

allows the possibility of introducing counters or flaps in any region of the magnet gap: however, it is necessary to see whether in the region where a block is removed the field suffers a local variation. Figure 25 shows that no such effect exists; but we have found that there is an effect on the overall field level. We have, in fact, measured the value of the magnetic field with different numbers of blocks out, and find that the field level varies by $\sim 0.1\,\%$ per two blocks.

iii) To facilitate movement the 86-ton magnet is supported on four compressed-air platforms 1 m in diameter. By correctly

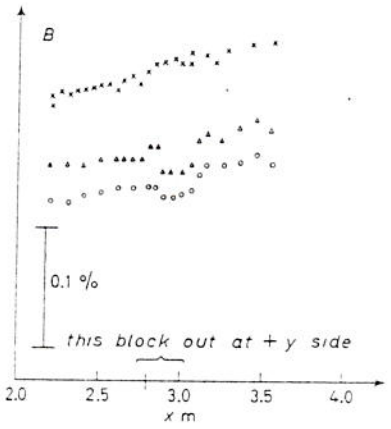

Fig. 25. – B *vs.* x, showing that the removal of a single side block does not give a local perturbation in the field. However, it does lower the whole field by $\sim 0.05\,\%$ due to the increase in yoke reluctance.

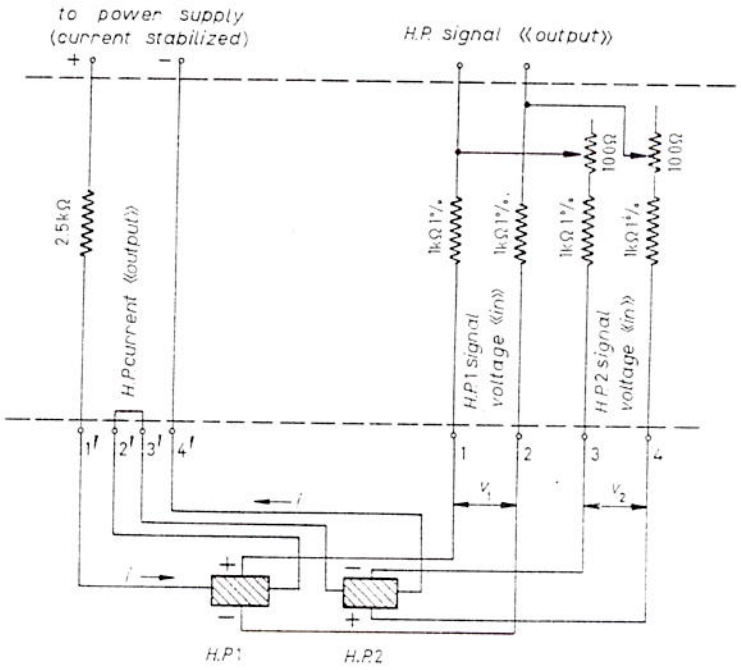

Fig. 26. – Compensating circuit for using two Hall plates in opposition. The Hall voltages cannot be added directly because of the potential difference between them due to the excitation current. A matched pair of Hall plates was used.

regulating the compressed-air supply the magnet could be raised slightly off the ground and moved about by means of block and tackle traction.

3·2. *Measurements of field shape.* – As mentioned above, a measuring stability of the order of 10^{-4} is necessary in order to construct a smoothly varying field of the correct shape. This is ten times higher than the stability needed for the $(g-2)$ measurement itself, and during the preparation of the shims the generator available for energizing the magnet was stabilized only to the order of 10^{-3}. To cancel the corresponding field fluctuations two Hall plates were used in opposition, with the circuit of Fig. 26. Such an arrangement also cancels to first order the fluctuations in the current supply to the Hall plates themselves. One Hall plate is kept fixed in a standard position in the magnet while the other is moved to survey the field, using the device sketched in Fig. 27. An overall short-term stability close to 10^{-4} was achieved.

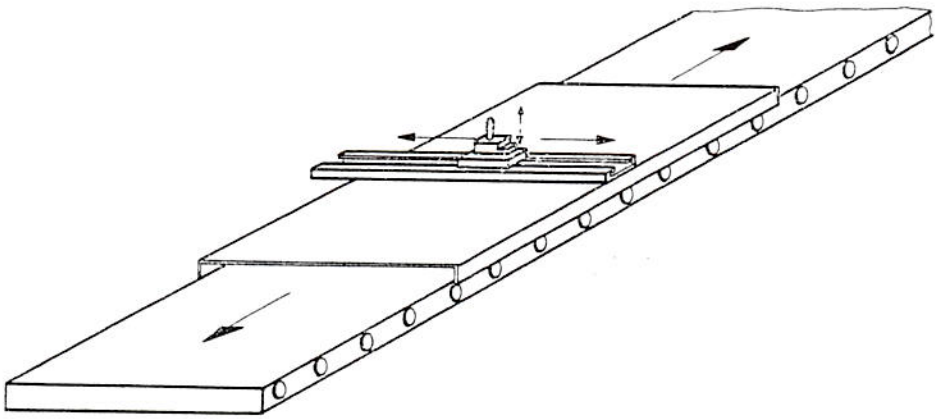

Fig. 27. – Carriage for moving Hall plate. The carriage rolled on rollers mounted on the side of the lower pole. (These rollers served later for supporting the side plates of the vacuum chamber, Fig. 33.) Control of x- and y-displacements was by means of nylon cords. A preset vertical adjustment was also available. The x-scale was established by means of a nonmagnetic tape attached to the carriage, and the y-scale fixed to the carriage was read by means of a telescope. Arrows indicate degrees of freedom.

We have measured the field shapes along y in some 20 chosen x positions. Knowing the shapes at given x's we know how, by now fixing a value of y, the field should vary along x. We have done this measurement for $y=0$, ± 5, ± 10, ± 15, ± 20, ± 21, ± 22, ± 23 and ± 24 cm. The final results of these measurements are shown in Fig. 28. All local irregularities have been reduced to a level of $\pm 0.2\,\%$ of the total field.

As we have seen in Sect. 2·2 the orbits follow contour lines of the magnetic field: strictly speaking the quantity that remains constant is the flux through

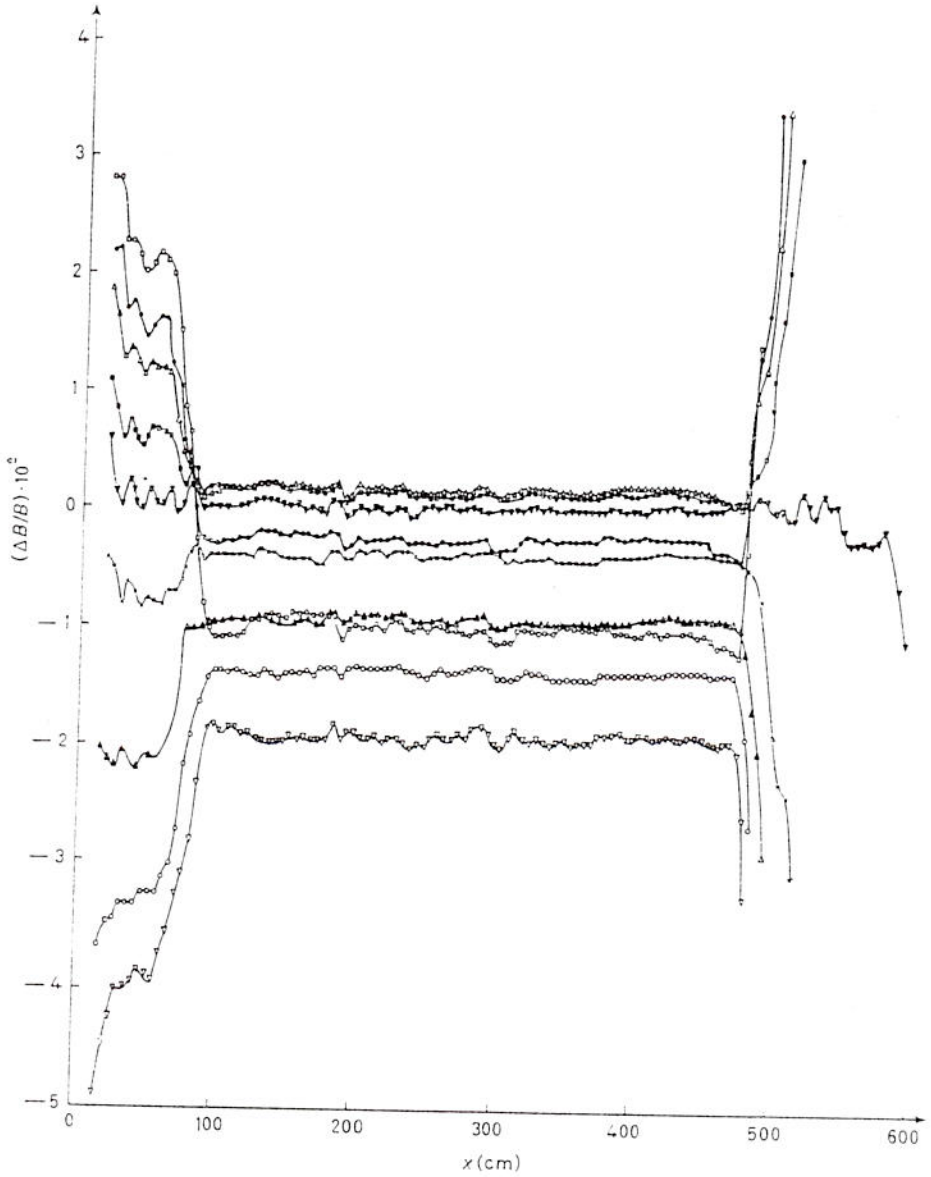

Fig. 28. – Results of traversing the Hall plate in the x-direction. Over the whole storage region $x = 100 \div 460$ the point-to-point fluctuations have been reduced to $\sim 10^{-3}$ and the flux averaged over the orbit area will fluctuate even less. At the two ends, the lines separate because of the increase in field gradient. The essential point is that the field corresponding to $x = 0$ (plotted) remains essentially constant from injection, through storage to the ejection region. (In the higher gradient regions larger fluctuations are permissible as they will not give rise to serious sideways deflection of the orbit.)

the orbit. Having scanned the field along x and y we could already see that the maximum jittering of the orbit could not be more than ± 1 cm in y; but a more direct way of checking this point is by means of a flux coil. A coil consisting of 50 turns of copper conductor with 19 cm radius (corresponding to the expected radius of the optimum muon orbit) is moved along the magnet. If the flux through this coil varies, an indication is obtained on a fluxmeter connected to the coil. To calibrate the scale in terms of orbit sideways displacement, the flux change for 2 cm sideways displacement is measured. To cancel the generator instability we used two coils in opposition; one is kept in a fixed position in the magnet, while the other is moved along x. In Fig. 29

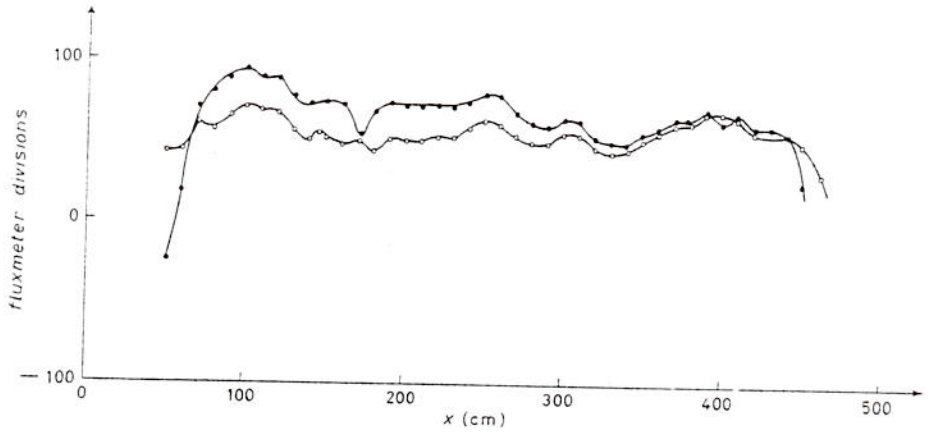

Fig. 29. – Flux-coil measurements of field variations in the x-direction, averaged over an orbit of 19 cm radius. 10 fluxmeter divisions correspond to 1 cm displacement of the orbit in y, as can be seen by comparing the two curves. Residual sideways fluctuations of the orbit have been reduced to $\sim \pm 1$ cm.

the results of the scanning performed at two fixed values of y all along the x axis are shown and are quite satisfactory. The function of the coil is to perform automatically the integration over the orbit one would like to have on the Hall-plate data, and in fact the final correction for x-dependence of the field was based on these flux-coil measurements.

3·2.1. The median plane. For the z-dependence of the field one must be sure that the magnetic median plane coincides with the geometric median plane. This is achieved by making the top and bottom shims perfectly symmetrical and by positioning them in a symmetric way with great care on the top and bottom pole pieces. Apart from natural irregularities of the magnet, this procedure should guarantee that the magnetic and the geometric median planes do coincide.

To show that the magnetic median plane coincides with the geometrical median plane two methods were used:

i) By the use of the flux coil: in this case one coil was kept fixed and the other was moved up and down. We verified that the flux increases in both cases and therefore the « magnetic » median plane is located correctly in the middle of the gap (minimum flux).

ii) By the use of the nuclear resonance technique (which will be described later). Here it is only necessary to say that the variation of the field along z is expected (*) to be $\Delta B/B \sim -0.4 \cdot 10^{-4} z^2$. This variation cannot be detected with the Hall plates, but can with the nuclear resonance. This check was performed after the generator stability had been improved (**) to $\pm 1 \cdot 10^{-4}$. We were then able to verify in many points of our magnet that the field was minimum in the geometric median plane; thus confirming what we already knew through the flux coil data.

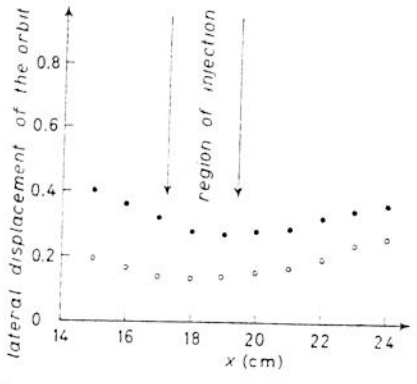

Fig. 30. – Flux-coil measurements in the injection region. Corresponding lateral displacement of the orbit (in cm) is plotted *vs.* x. In connection with the determination of the scattering of the muons in the injection assembly, it was essential to establish that the orbits do not jitter sideways in the first few turns (see Sect. 6·5.4). This is established by the detailed measurements shown above. (Note that the points for $y_c = -2$ have been arbitrarily displaced for comparisons with the points belonging to $y_c = 0$, thus permitting an expansion of the vertical scale.)

3·3. *Absolute calibration of magnetic field.* – In the Hall-plate measurements discussed above, the field variations were measured relative to the value at a fixed point in the magnet ($x = 350$; $y = 10$; $z = 0$). The absolute value of the field was obtained by nuclear resonance. Due to the dimensions of our magnet we could not use the commercially available proton-resonance devices without solving the problem of lengthening the maximum cable length (50 cm) by a factor ~ 10. Instead we have designed a loosely coupled resonant circuit of which the proton resonance probe is an element, fed by an independent frequency generator through a matched cable. The circuit of the 60 MHz frequency generator and of the loosely coupled circuit, together with the other details for observing the proton resonances signal is shown in Fig. 31. The advantage of this system with respect to the commercial devices is that any

(*) As $\nabla^2 B = 0$, $\partial^2 B/\partial z^2 = -\partial^2 B/\partial y^2 = -2b = 0.8 \cdot 10^4$ cm^{-2}.

(**) We are grateful to Mr. T. JENE for this very significant improvement.

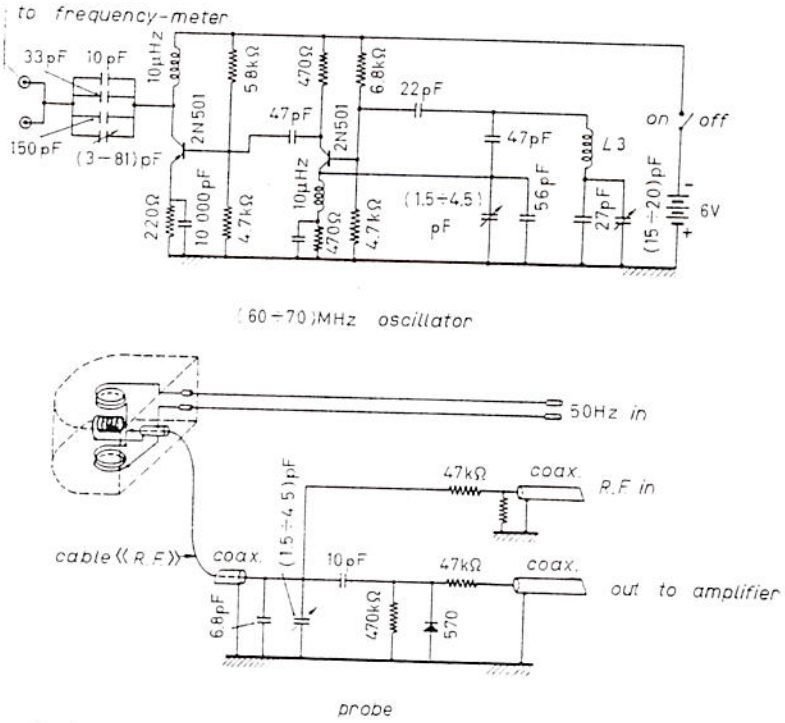

Fig. 31. – Nuclear resonance probe. The commercial (NUMAR) probe is modified as shown and driven by a separately tuned oscillator. As output and input to the probe go via matched cables, virtually any length of cable can be used.

cable length can be used between the proton-resonance probe and the frequency generator. A disadvantage of this system is that the resonant circuit must be retuned whenever the oscillator frequency is changed appreciably.

Using this proton-resonance probe placed at ($x=350$; $y=10$; $z=0$), and varying the excitation circuit of the electromagnet, the calibration curve (field *vs.* current) shown in Fig. 32 is obtained. The

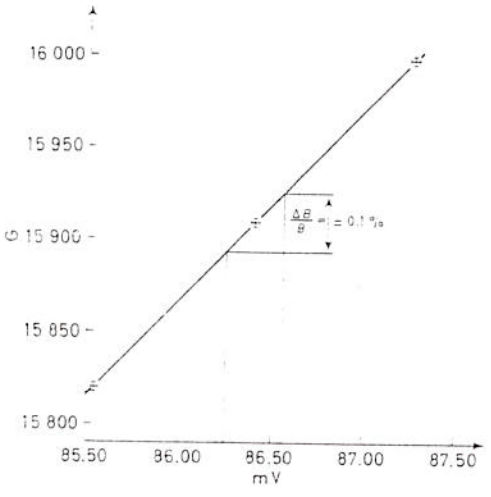

Fig. 32. – Magnetic field measured by nuclear resonance at $x=350$, $y=-10$, *vs.* shunt voltage. All experiments were run at 86.40 mV.

calibration of the magnetic field is thus known to one part in ten thousand and was checked before and after the experiment. The lack of jitter in the typical proton-resonance signals of Fig. 33, showed that there were no high-frequency fluctuations of the magnetic field.

From the knowledge of the absolute field at one point, plus the relative field shape as obtained by Hall plates, the mean field over the muon orbit can be calculated as discussed in Sect. 6·3.

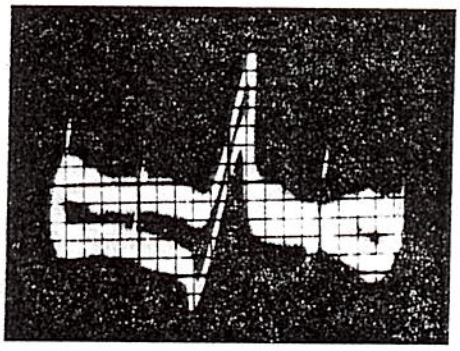

Fig. 33. – Nuclear resonance signal obtained with probe of Fig. 31 using cables ~ 4 m long. The clean signal shows that there were no high-frequency fluctuations of the magnetic field.

During the experiment the shunt voltage was set at 86.40 mV, corresponding to 15.909 kG at the calibration point ($B_0 = 15.871$ kG). The magnet current was monitored every few hours during the collection of the data and never varied by more than 0.05 % from its nominal value. As can be seen from Fig. 32, the corresponding change in the magnetic field is a factor of two less.

3·4. *Vacuum system.*

3·4.1. Vacuum required for muon storage, gas scattering. The limiting condition on the vacuum required in the magnet is set not by the slowing down of the muons, but by loss due to multiple scattering. This tends on the average to increase the amplitude of the vertical oscillation

$$z = A(l) \sin\left(\frac{l}{\lambda}\right), \tag{74}$$

where l = path length, until A reaches the maximum value h allowed by the magnet aperture and the particle is lost.

For a particle which has, at a particular instant, displacement z and inclination to the horizontal plane

$$\Theta = \frac{\mathrm{d}z}{\mathrm{d}l} = \frac{A}{\lambda} \cos\left(\frac{l}{\lambda}\right),$$

the amplitude A can always be found from

$$A^2 = \lambda^2 \Theta^2 + z^2 .$$

The effect of scattering is to change the initial angle Θ_0 to $\Theta = \Theta_0 + \Theta_s$, z remaining the same. Therefore,

$$\frac{\partial}{\partial l}\langle A^2\rangle = \lambda^2 \frac{\partial}{\partial l}\langle \Theta^2\rangle = \lambda^2 \frac{\partial}{\partial l}\langle \Theta_0^2 + \Theta_s^2 + 2\Theta_s\Theta_0\rangle = \tag{75}$$

$$= \lambda^2 \frac{\partial}{\partial l}\langle \Theta_s^2\rangle = \frac{1}{2}\lambda^2 \left(\frac{E_0}{p\beta c}\right)^2 \frac{1}{X_0},$$

where $E_0 = 21$ MeV, and X_0 is the radiation length for the gas contained in the magnet.

If the oscillation amplitudes A in the magnet are populated according to the normalized distribution function $n(A, l)$, the change with distance l will be governed approximately by the diffusion equation

$$\frac{\partial n}{\partial l} = D \frac{\partial^2 n}{\partial A^2}, \tag{76}$$

where D, the diffusion coefficient, can be obtained by noting that according to eq. (76)

$$\frac{\partial}{\partial l}\langle A^2\rangle = \int A^2 \frac{\partial n}{\partial l}\, \mathrm{d}A = D\int A^2 \frac{\partial^2 n}{\partial A^2}\, \mathrm{d}A = 2D\,. \tag{77}$$

Equating eqs. (75) and (77) one finds

$$D = \left(\frac{E_0}{p\beta c}\right)^2 \frac{\lambda^2}{4X_0}\,. \tag{78}$$

The solution of eq. (76) corresponding to the boundary conditions $n(A, l) = 0$ when $A = \pm h$ is of the form

$$n(A, l) = \exp[-\alpha l] \cos\left(\frac{m\pi A}{2h}\right) \qquad \text{with } m = 1, 3, 5 \ldots\,. \tag{79}$$

By substitution in eq. (76) one finds for the mean free path

$$L = \frac{1}{\alpha} = \frac{4h^2}{m^2\pi^2 D} = \frac{16h^2 X_0}{m^2\pi^2\lambda^2}\left(\frac{p\beta c}{E_0}\right)^2, \tag{80}$$

showing that the higher modes ($m \geqslant 3$) decay away very fast and can be neglected.

So far we have assumed that a particle is lost as soon as its oscillation amplitude A reaches the maximum allowable value h; but in fact the loss is

only effective at the maximum phase of the oscillation eq. (74), and before this is reached A may diffuse back below the critical value. We thus have a « first passage » problem.

The real distribution function therefore extrapolates to zero slightly beyond the edges of the magnet at $A = h + h_1$, where h_1 is the extrapolated length. To estimate the correction assume that a distribution function of the form $\cos[\pi A/2(h+h_1)]$ is continuously regenerated but that twice per cycle, at intervals $\Delta l = \pi\lambda$, the tails of the function projecting beyond $A = h$ are cut off. The fraction of particles lost each time is $(\pi^2 h_1^2/8h^2)$ so

$$\frac{1}{n}\frac{\partial n}{\partial l} = -\frac{\pi^2 h_1^2}{8h^2}\frac{1}{\pi\lambda}. \tag{81}$$

However, using eq. (80) with $m = 1$,

$$\frac{1}{n}\frac{\partial n}{\partial l} = -\alpha = -\frac{\pi^2 D}{4h^2}.$$

Hence, equating these two expressions,

$$h_1 = \sqrt{2\pi\lambda D}. \tag{82}$$

Modifying eq. (80) accordingly, the new mean free path becomes

$$L = \frac{16(h+h_1)^2 X_0}{\pi^2\lambda^2}\left(\frac{p\beta c}{E_0}\right)^2. \tag{83}$$

Computing from eqs. (78) and (82) with $p = 90$ MeV/c, $\lambda^2 = 1/b = 2\cdot 10^4$ cm^2, one finds, for air at pressure p atmospheres,

$$h_1 = 4.2\, p^{\frac{1}{2}}$$

a negligible extrapolation correction at most pressures. From eq. (83) with $h = 5$ cm, $L = 500/p$ cm $= 4/p$ turns. So, the mean free path determined by air scattering drops from ~ 4 turns at atmospheric pressure to 3000 turns at 1 mm pressure. A vacuum less than 1 mm is therefore completely satisfactory.

In practice we found that raising the pressure to 1 mm cut the stored rate by 30 %. The average number of turns being ~ 800, this checks well with the calculation.

3·4.2. Vacuum required for α-particle storage. In making preliminary tests on the storage system using α particles of 4.6 MeV, the vacuum requirement is determined by the cross-section for electron pick-up to form

an He^+ ion. If this happens, the radius in the magnetic field is doubled and the particle has a high probability of leaving the magnet before the reverse process $He^+ \to He^{++}$ occurs. Referring to the data of RUTHERFORD [19] one finds for 4.44 MeV α particles that the mean free path λ for electron pick-up in air at N.T.P. is 0.52 mm. Hence, for $\lambda = 2\,000$ turns one calculates $p = 1.7 \cdot 10^{-4}$ mm.

This is a much higher vacuum than required for the muon storage and means that a diffusion pump must be used. We used a three-stage oil diffusion pump with a speed of 500 l/s, backed by a mechanical pump giving 150 l/min.

3·4.3. Vacuum tank. The mechanical construction of the vacuum tank involved some unusual features, occasioned by our desire to have easy access to the interior (*e.g.*, for field measurements) without demounting the magnet.

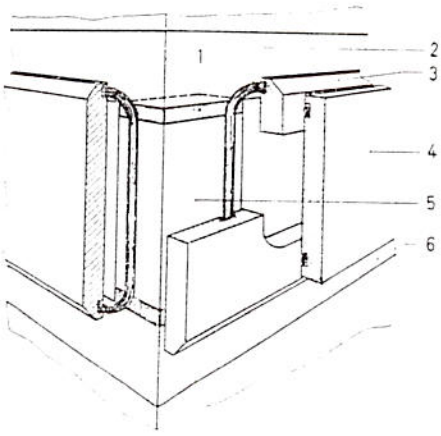

Fig. 34. – Corner of vacuum chamber, showing corner post sealed above and below by hard rubber sheet. The O-rings for the 595 cm long side plate and the 50 cm long end plate sealed onto the poles for their main length, then passed across the hard rubber to run vertically down the corner post. Stop-cock grease was used to improve the seal. This chamber could be mounted and demounted without disturbing the magnetic properties of the system. 1) Hard rubber; 2) O-ring; 3) long side plate (595 cm); 4) secondary side plate (90 cm) (6 each side); 5) corner piece; 6) pole.

The rectangular tank was assembled from six separate plates, plus four corner pieces. The top and bottom pole pieces, 5 cm thick, pulled up to the magnet yoke by long bolts, provided the main strength. The long side plates and the end plates were sucked onto the sides of the pole pieces by the vacuum itself which alone provided enough force to compress the O-rings. The joint between the side plates and the end plates at the four corners is shown in Fig. 34. It consisted of a rectangular corner post sealed top and bottom by 5 mm hard rubber sheet, the whole assembly being greased and forced into the magnet with the help of a small taper on the inside corner. This provided enough pressure for the seal. The sides of the rubber (distorted by the compression) were carefully trimmed flat so that the O-rings of the side plates would run smoothly across them and conti-

[19] E. RUTHERFORD: *Phil. Mag.*, 4, 277 (1924). See also E. RUTHERFORD, J. CHADWICK and C. D. ELLIS: *Radiations from Radioactive Substances* (Cambridge, 1930), p. 124; and for a review S. K. ALLISON and S. D. WARSHAW: *Rev. Mod. Phys.*, 25, 779 (1953).

nue down the faces of the corner piece itself. The corner pieces were held in position by bolts connecting them to the end plates, which in turn were fixed to the magnet.

The long side plates, however, were not bolted but held roughly in position by a series of rollers below and a guide above. The initial force to compress the O-rings was provided by adding sheets of iron. To start the vacuum the magnet was energized, thus attracting the iron plates inward and compressing the gaskets. Once a rough vacuum was established the iron plates could be removed.

The system worked satisfactorily although we occasionally had leaks at the corners. We were able to maintain a vacuum of $(1 \div 1.7) \cdot 10^{-4}$ mm for the α-particle storage, and normally ran the muons using the backing pump only at a pressure ~ 0.1 mm.

3·5. *Storage of α particles.*

3·5.1. Apparatus (see Fig. 35). Having obtained sufficient agreement between the theoretical field shape and the measured field produced by the shims, a final and very direct check on the storage properties of the field was made by storing α particles of the appropriate momentum in the magnet. In

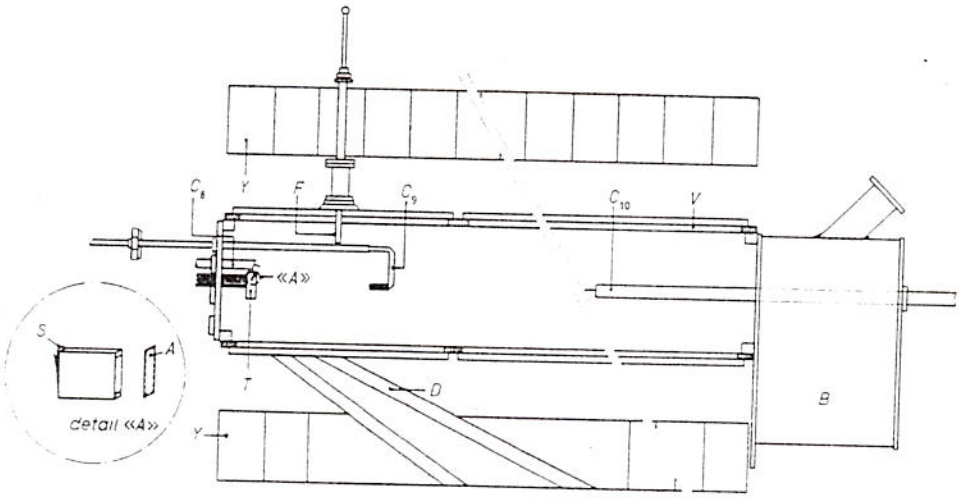

Fig. 35. – Apparatus for establishing the storage of α-particles. S, source of thorium-active deposit; H, collimator; A, graded absorber to give correct momentum spread; T, table, adjustable in x and y under vacuum; C_8, injection counter, plastic scintillator; C_9, caesium iodide scintillator; C_{10}, caesium iodide scintillator; B, extension to vacuum chamber to enable α-particles ejected from the field to be studied; V, vacuum chamber walls; Y, yoke of magnet; F, flap for cutting orbits to establish position in y.

this way no cyclotron time was expended at this stage of the project. This is a significant point, since moving and positioning of the 86-ton magnet requires considerable effort and, once in position, it blocks access to several other beams in the experimental area. We thus avoided untimely interference with other experiments.

The α source consists of thorium-active deposit on an area ~ 0.25 cm^2 of a small aluminium plate. The dominant lines are 8.776 and 6.043 MeV. The 8.776 MeV α's are slowed down through a graded absorber to 160, 180 or 200 MeV/c, corresponding to orbit radii of 17, 19 and 21 cm. This roughly spans the expected distribution of muon-orbit radii. The 6.043 MeV α's stop in the absorber. The 8.776 and 6.043 MeV lines provide the calibration for a silicon junction detector (*), with which it is checked that by inserting the corrected amount of absorber the expected residual momenta are indeed obtained. The source is fastened to the back of a rectangular slot of thin copper (see Fig. 35). The α's emerge through the front end of the slot, which is covered with Al foils. The slot is 2.5 cm long (in the direction of the α beam), 1.5 cm high, and 0.4 cm wide. Only α's emitted within $\sim \pm 16°$ in the vertical and $\sim \pm 4.5°$ in the horizontal direction are thus injected into the magnet. This again is to simulate conditions for storing muons, where multiple scattering and re-incidence on the moderator limit the angular range of acceptable muons.

The source is mounted on a table which can be moved in both the x and y direction without breaking the vacuum. The x motion is made by means of push-rods on which the table rests; the y motion is made by turning a rod which is connected to the table through a rack and pinion movement. Finally, the angle of the slot with respect to the table can be set. In this way the whole available range of angles and positions of injected muons can be simulated.

On leaving the source the α particles pass through a counter consisting of 2.56 mg/cm^2 plastic scintillator covered on each side by 3 μm Al, placed 1.7 cm in front of the source so that the α's traverse it only once. This counter is regarded as an element of the graded absorber mentioned above. It serves to monitor the injected intensity and gives a « start » signal for timing the α particles. The stored particles are detected by one of two counters: for storage out to $x = 150$ cm, counter No. 9 is used. This counter is described in Sect. 6·1 in connection with short storage of muons, the only change here being that the plastic scintillator is replaced by a CsI crystal of the same area (see Fig. 35). Once storage out to 150 cm was established we looked for particles at the other end of the magnet using a counter (No. 10) projecting in from the far end: this was a (5×4) cm CsI crystal on a 210 cm light pipe, and adjustable under vacuum from $x = 470$ to 620 cm. A special « α ejection box » was constructed and attached to the main vacuum system; this made it possible to retract

(*) RCA Victor Company, Ltd., silicon junction α detector, type A.

counter No. 10 out of the magnetic field into the ejection region, and to measure the ejected α particles under vacuum.

A conventional time-to-pulse-height converter ([20]) was used to display the time-of-flight of the particles in the magnet on a 100-channel pulse-height analyser. The period of revolution of the α particles in the magnet being 82.5 ns, the number of turns in the field could then be calculated.

3·5.2. Measurements. The radius distribution of particles making half a turn in the field is first studied with the results shown in Fig. 36. This picture is obtained by moving counter No. 9 along x and plotting the content of only those channels of the analyser which correspond to α's arriving in No. 9 within less than 80 ns. From the position and angle of the source one expects a 19 cm radius particle to arrive at $x \approx 55$ cm. The observed position is $(52 \div 53)$ cm, suggesting that the mean radius is slightly lower, $\varrho = 18$ cm. If counter No. 9 is now moved out to larger x, the counts at the half-turn decrease and the bulk of the particles appears later on the time scale indicating storage.

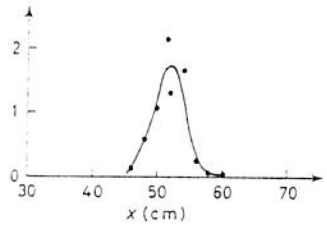

Fig. 36. – Counting rate *vs.* C_9 position for α-particles making a half-turn in the field.

With counter No. 9 at $x = 148$ cm, and after optimizing the stored rate by varying the source position and angle, the brass flap F (see Fig. 35) is pushed into the magnet. The flap cuts the orbit after $\sim \frac{1}{4}$ turn and, as the mean radius of the orbits is known, enables one to compute the position of the orbit centres for the stored beam. It turns out that with F set at $y = -21$ to -22 cm, half the particles are eliminated, implying that the orbits with $y_c = -3$ cm injection are stored most efficiently.

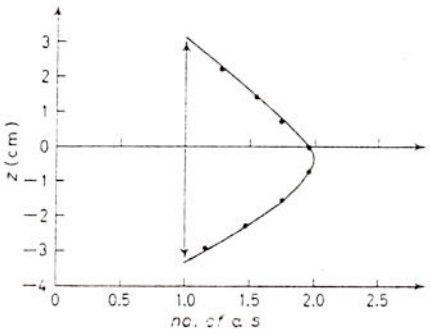

Fig. 37. – Vertical distribution of α-particles at $x = 75$ cm.

Before looking at the far end of the magnet a further check on the field design was made. By moving counter No. 9 up and down it was established that the beam is roughly centred in the magnet, see Fig. 37. The full width at half height is 6.3 cm. The beam centre is within 5 mm of the middle of the magnet. This vertical scan was

([20]) J. FISCHER and A. LUNDBY: *Rev. Sci. Instr.*, 31, 10 (1960).

done at $x = 75$; scans at other positions gave similar results. This confirmed that the magnetic median plane was in the centre of the magnet.

To detect now particles stored for long times, counter No. 10 with long pipe is introduced through the ejection end and placed at $x = 485$ cm. A very prominent bump appears between 20 and 160 μs, peaking around 60 μs, indicating storage for an average of some 700 turns and extending to 2000 turns (see Fig. 38).

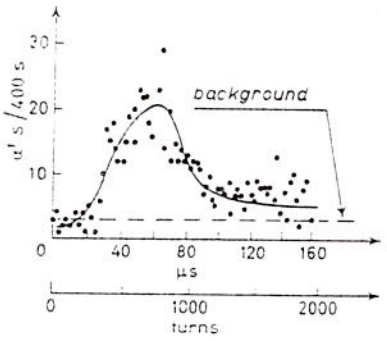

Fig. 38. – α-particle storage for (500÷2000) turns observed at $x = 485$ cm.

Using storage theory [Sect. 2·2, in particular eqs. (35) and (44)] and the parameters a, b, c, d as deduced from the measured field shape, one expects α's with 19 cm radius and $y_c = -2$ to appear at 64 μs, those with $y_c = -1$ at 75 μs, $y_c = 0$ at 90 μs, $y_c = +1$ at 114 μs. Figure 38 thus indicates that orbits with y_c between -1 and -2 cm are stored with highest efficiency.

Various means are now available to maximize this efficiency. We shall not discuss their effects in any detail. By rotating or displacing the source, the bulk of the injected particles can be directed into the high-efficiency region of the magnet. The orbits can be shrunk or expanded by changing the main magnetic field, their momenta can be changed by varying the foil thickness. The optimum conditions were reached in Fig. 39, curve a; the mean storage time is rather short, but the number of stored α's is maximum. This picture was taken at $x = 589$ cm, and curve b shows that the α's are ejected from the field.

The trapping efficiency is best measured in terms of the number of particles making half a turn. At the half-turn the rate is (30÷40)/s in a counter 1 cm high and integrated over all momenta. As the path from source to counter $\pi R \sim 60$ cm

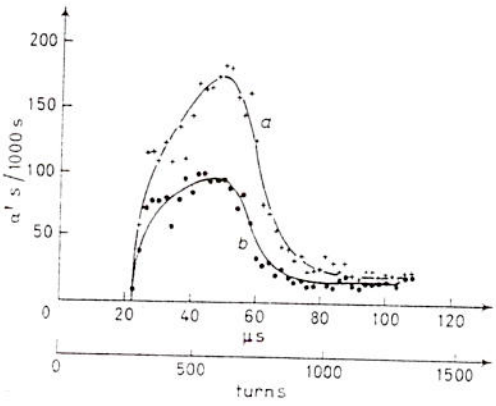

Fig. 39. – Curve a: α-particle storage observed in the ejection region ($x = 589$ cm). Curve b: α-particle storage observed in the ejection region ($x = 612$ cm). These curves show that a large fraction of the particles are ejected from the magnet.

particles are accepted over a vertical angular range of 1°; compared to the acceptance of the magnet which is $2h/\tilde{\lambda}_z \sim 4.5°$, as $h \sim 6$ cm and $\tilde{\lambda}_z \sim 160$ cm is the wavelength for vertical oscillations. The corrected rate at the half-turn is thus 160/s. At $x = 458$ cm we observe about 3 α's/s (Fig. 38) and under optimum conditions (Fig. 39) 10 α's/s at $x = 589$ cm. The storage efficiency is thus of the order of 6 %. About half the α's are ejected (Fig. 39); the other half is presumably lost in the violent oscillations to which they are subjected in stepping across the magnet boundary at $x = 600$ cm. After these tests we increased the field gradient at the ejection end of the magnet by ~ 25 % to the final value reported in Sect. 3·1 and 3·2 above. As a result, almost complete ejection was obtained in the muon experiments reported below.

4. – Electronics.

4·1. *The polarization analyser.* – The polarization analyser has been designed to measure the muon spin direction with with a good accuracy ($\sim 0.5°$), and to collect as much as possible of the ejected muon beam. This determines the apparently large size of the counters, 30 cm wide × 15 cm high. The angular spread of the beam ($\sim 15°$), see Fig. 7, impinging on the analyser is large, but nevertheless it is possible to measure the mean direction of arrival with the required accuracy (see Sect. 6·4). The thickness of the target is sufficient to embrace the range spread of the muons ejected from the magnet.

For the measurement of the spin direction, the technique used is inspired by the method described by COFFIN *et al.* [21]. The muons are stopped in a nondepolarizing insulating material. A pulsed vertical magnetic field is then applied of such intensity and duration that the spin rotation in the horizontal plane determined by $\int B\,dt$ is either 180° (37 G μs) or $\pm 90°$. In the first case the comparison in the same electron telescope of the decay electron intensity at 0° and 180° flipping yields the value of the longitudinal component of the polarization $A_\parallel$; in the second case the same comparison at $-90°$ and $+90°$ flipping yields the transverse component of the polarization $A_\perp$. The angle of spin to the normal to the plane of the analyser is then determined from $\mathrm{tg}\,\theta_s = A_\perp/A_\parallel$.

This method has the advantageous feature of giving results independent of the counter geometry because only one counter telescope is used. However, to increase the efficiency of electron detection we use two electron telescopes 66′ and 77′ (see Fig. 40), the results for each being evaluated separately.

The flipping of the spin must be accomplished within a time short compared

---

[21] T. COFFIN, R. L. GARWIN, S. PENMAN, L. M. LEDERMAN and A. M. SACHS: *Phys. Rev.*, 109, 973 (1958).

to the muon lifetime. With the electronics described below, the over-all time taken to detect the muon and to complete the flipping of the spin is 1.0 μs. The decay electrons are counted in a gate 5 μs long starting 1.1 μs after the muon arrival; 55 % of the decay times fall within this gate.

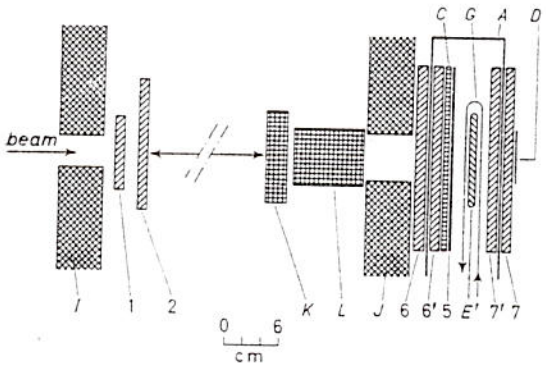

Fig. 40. – Polarization analyser with thin target for input beam measurements. 1, 2, 6, 6', 5, 7, 7', plastic scintillators; E', methylene iodide target in mylar bag; G, flipping coil; A, mumetal shield; C, plexiglas backing for thin scintillator No. 5; I, J, brass collimators; L, beryllium moderator; K, carbon moderator, variable; D, mirror for alignment.

Note that the angle $\pm\theta$ through which the spin is flipped is not critical. If θ deviates from 90°, the effective asymmetry A generated for transversely polarized muons is reduced (as $A \sin\theta$), but there is no error in the polarization angle provided the angles for + and — flipping are the same. Muons polarized perpendicular to the analyser plane, for example, always give zero asymmetry. To ensure equality of the angles the direction of current through the flipping coil is changed by a mechanical commutator. One can show that any capacitive currents (*e.g.* to earth), which may not reverse perfectly, contribute zero to $\int B\,\mathrm{d}t$ because the voltages on all parts of the system are the same before and after the pulse.

Also, it is not necessary for the reversible field to return absolutely to zero after the flipping. A residual steady or oscillatory field will slightly change the effective value of θ for the average muon which decays in the 5 μs time gate but as mentioned above this is not important.

Any nonreversible residual field will, however, cause errors, because it processes all muons in the same direction for time $(1.1 + 2.2) = 3.3$ μs on the average, giving 16° per gauss. The stray field in the target is reduced by iron and mumetal shields, and a small correction is applied for the residual error. In the run with the storage magnet the residual field was 0.02 G upwards, giving a mean spin rotation of —6 mrad. During the input beam measurements the residual field was less than 0.01 G, and no correction was necessary.

4·1.1. Determination of polarization angle. As defined above, the polarization angle θ to be measured is the angle of spin relative to the momentum $\theta = \theta_s - \theta_p$. This is obtained by measuring separately θ_s and θ_p relative to the normal to the plane of the analyser. Consider first the measurement of θ_s.

It is assumed that for $\pm 90°$ flipping the decay electron asymmetry, $A = (n_+ - n_-)/(n_+ + n_-)$, is zero when the muon spin is normal to the plane of the analyser, $\theta_s = 0$. We will now discuss this assumption. For a given counter telescope, say 66′, A will be zero when the spin points along the average direction in which the electrons are counted. This average is to be computed from the counter and target geometry, allowing for absorption of the decay electrons by ionization and bremsstrahlung. If the counters were infinitely wide and of uniform efficiency, the direction would be determined by absorption effects, and would clearly be normal to the counter plane irrespective of the sideways distribution of stopping muons in the target. For an analyser of limited sideways extent this remains true, except for muons stopping so near the edge of the analyser that an appreciable fraction of electrons are lost for geometrical reasons. Absorption effects have already reduced the probability of counting oblique electrons, so these losses become serious only in the last 5 cm at each side of the analyser. Even so, with uniform illumination with muons the mean direction is still normal to the analyser. Errors arise only if, in the last 5 cm, one side is more strongly illuminated than the other.

It is important to realize that errors due to non-uniform illumination of the target are opposite in the forward and backward telescopes, and should cancel in the mean result. One can look for this effect by comparing the $(g-2)$ results obtained with each telescope computed separately.

For measurements on the incident beam the illumination was confined to 10 cm at the centre of the analyser, where this error is negligible.

The essential requirement in the analyser is therefore to maintain counters and target strictly parallel and to reproduce the setting of the whole slab to a fraction of a degree. There is no difficulty in achieving 1 mm accuracy over the 30 cm width, corresponding to 0.2°. It is also essential that the electron telescopes shall have uniform efficiency; this was measured in an auxiliary experiment and found to be always $> 99.5\,\%$ with no left-right asymmetry.

As the same apparatus was used for measurements on the injected and the ejected beam any residual systematic errors should cancel.

The determination of θ_p relative to the normal to the analyser is discussed in Sect. 5 and in Sect. 6·4.

4·1.2. Description of the analyser-target. The targets used are made of methylene iodide, CH_2I_2, chosen for the following properties (*): it does not depolarize the stopped muons: its high density, 3.3, allows the building of targets of a given stopping power with minimum volume, thus requir-

(*) These properties of CH_2I_2 were pointed out to us by the Columbia group measuring the gyromagnetic ratio of the muon.

ing a minimum power from the flipping field generator; it is nonconductive, a necessary condition for the flipping method to be used; and, finally, it does not dissolve lucite, thus allowing the easy construction of containers of any size or shape, with thin walls.

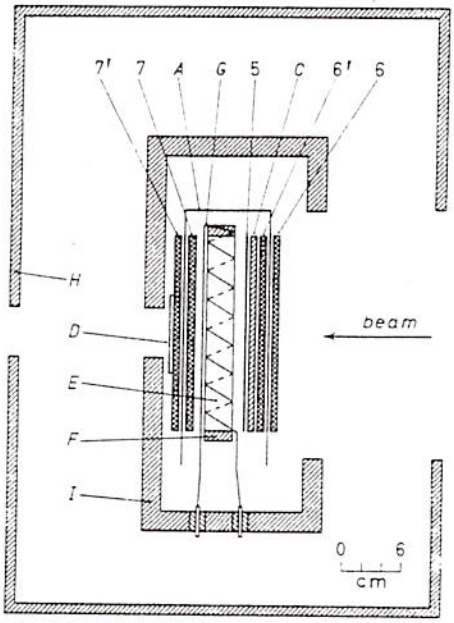

Fig. 41. – Polarization analyser with thick target. *E*, methylene iodide in thin-walled plexiglas box, *F*; *H*, *I*, iron shields. For other symbols see caption to Fig. 40.

Two types of target are used; a thin target for the analysis of the polarization of beams as a function of the range of the muons (Fig. 40), and a thick target for the analysis of the muons ejected from the storage magnet (Fig. 41). The first one consists of a mylar bag, of wall thickness 0.01 mm containing the liquid, and compressed between styrofoam slabs with an average thickness of the CH_2I_2 of about 8 mm. The second one consists of a lucite container with 1 mm thick walls, 30 cm wide, 20 cm high, and 2 cm thick.

The coil for the pulsed magnetic field consists of aluminium tape of 14 mm width, 0.1 mm thickness, wrapped around the targets at one turn per 1.8 cm.

4·1.3. Magnetic shielding. The shielding is done in three steps. Two iron boxes surround the counting assembly and the target. They are made of 1 cm and 2 cm thick Armco iron with beam apertures in the front face of (50×25) cm for the first one, and (30×25) cm for the second. An annealed mumetal box of 1 mm thickness, 26 cm width, and 60 cm in height surrounds the target. The mumetal serves the additional purpose of providing an absorber between the electron counters of the telescope as described below, thus reducing accidental coincidences due to knock-on protons from fast neutrons.

With the box in position near the storage magnet (Fig. 41), the magnetic field in any direction, as measured by Hall plates at the target position, is less than 0.05 G. The vertical component was measured with a sensitive magnetometer as 0.02 G directed oppositely to the main magnet field.

4·1.4. The counter telescopes. Five counters are built into the analyser to define the incoming muon and the decay electron. The decay electrons are counted in two telescopes, 66' and 77', made of 8 mm thick scintillator, 30 cm wide and 20 cm high. The solid angle which each end of these telescopes

subtends at the middle of the target is $0.75 \cdot 2\,\pi$. It is very close to the optimum solid angle, compromising between the reduction of the asymmetry due to integration over a big angle and increase in intensity. The asymmetry is expected to be reduced by a factor of about 0.63 in this geometry. A small additional reduction is expected from the fact that about 8 % of the accepted muons, with the thick target, are stopping in the lucite walls or in the scintillators. The maximum asymmetry, in good geometry in the direct beam, being 25 %, we expect a value of 15 % with our analyser. We observe 12 % with a thin target in the injected beam and 15 % with a thick target in the ejected beam. This difference can be explained by the slight increase in asymmetry expected with the thick target due to the hardening of the decay electron spectrum, of which 50 % is absorbed, and from the fact that with a thin target more muons stop outside the target and are not flipped. Also some possible slight contamination of pions in the straight beam may be responsible for the smaller asymmetry.

Counters 6 and 6′ are separated by the 1 mm thick mumetal walls, as also 7 and 7′.

The incoming muons are detected by the counters 66′ and the thin counter 5, 0.3 cm thick, 30 cm wide, and 20 cm high, located immediately in front of the target. A stopped muon is defined by the signature $66'\,5\overline{7}$, in coincidence with one or several upstream counters. Counter 5 is thin to reduce the number of muons which stop in it before reaching the CH_2I_2 and thus reduce the electron asymmetry.

Careful checks have been done with beams traversing all five counters in order to prove that the efficiency of the counters is uniform and especially that it does not exhibit a right-left asymmetry. The efficiency of the counters 66′ 77′ was proved to be very close to 100 % for fast charged particles.

The whole assembly of counters and target is held tight in correct geometrical position by clamps and spacers. A mirror, glued on the back of the last counter, allows accurate positioning of the assembly. The entire assembly

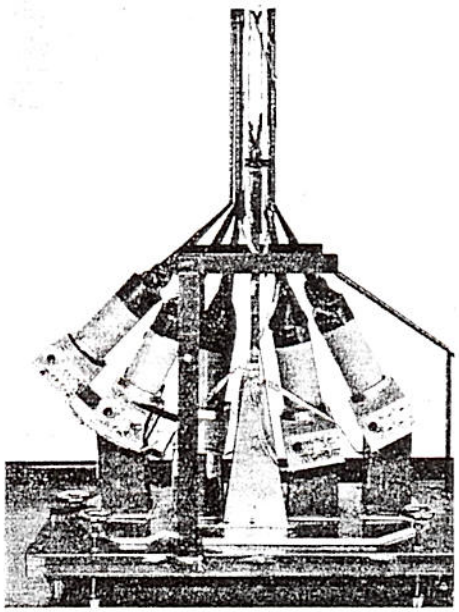

Fig. 42. – Polarization analyser assembly with iron shields removed. The whole assembly can be rotated on the trolley for fine angular adjustment.

can be rotated about a vertical axis, for small final adjustments of angle, independently of the iron shielding boxes. A photograph of the analyser assembly without its iron shielding is shown in Fig. 42.

4·1.5. The electronics associated with the polarization analyser. The electronics associated with the analyser comprises the coincidence circuit defining the arrival of the muon, and the pulsed current generator. Both are placed close to the analyser in order to reduce the delay in triggering the pulsed field. The circuit diagram of the pulser, which is similar to that of Coffin *et al.* [21], can be seen in Fig. 43. An EFP 60 univibrator delivers a posi-

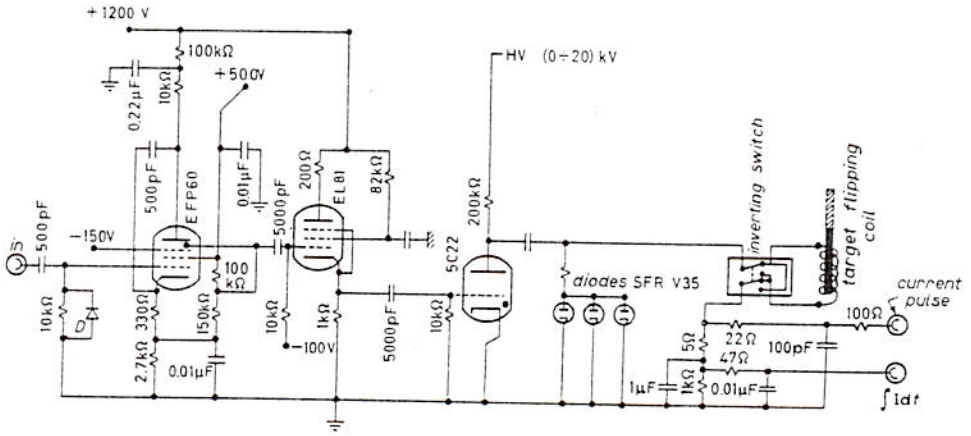

Fig. 43. – Pulse generator for energizing flipping coil.

tive 600 V pulse to the grid of a 5C22 thyratron. The flipping coil is in series with a storage capacity C_1 (0.006 μF) charged through the plate resistance R_1 to the supply voltage, adjustable from 0 to 15 kV. When the thyratron is fired the capacitor is discharged building up current, until at maximum current the voltage on the coil reverses and the current then decays exponentially through the diodes.

The rise-time of the pulse is 0.3 μs, decay-time 0.4 μs. The delay between the muon arrival and the beginning of the flipping pulse is 0.3 μs. For 180° flipping the largest coil requires 9 kV plate voltage on the thyratron plates.

The final adjustment of the plate voltage is done by measuring the value of $\int B\,dt$. This integral should be 37 G·μs for 180° flipping. It is measured directly by an integrating circuit; and for continuous monitoring in the runs the related quantity $\int I\,dt$ is recorded, where I is the current. A 1 μF capacitor C (Fig. 43), calibrated to 1 %, is connected in series with the coil, and yields a

voltage step V which is measured with an oscilloscope

$$V = \frac{1}{C}\int I\,\mathrm{d}t = \frac{10^{-7}}{4\pi N C}\int B\,\mathrm{d}t\,, \tag{84}$$

(N = number of turns per cm = 1/1.8 cm, C is the value of the capacitor).

The direct measurement of $\int B\,\mathrm{d}t$ is achieved as follows. A pick-up coil of inductance L and calibrated surface S, of order 2000 cm², is introduced into the target perpendicular to the lines of flux. It is shunted by a capacity C, such that the ringing period is large compared to the pulse duration. One can then show that the initial amplitude of the ringing train induced by the pulsed field is proportional to $\int B\,\mathrm{d}t$,

$$V = \frac{S}{10^8}\left(\frac{2\pi}{T}\right)^2\int B\,\mathrm{d}t\,, \tag{85}$$

where the period T of the tuned coil is to be determined in an auxiliary measurement.

An over-all check on the calibration is obtained by measuring the decay electron asymmetry as a function of the current in the coil.

In order to allow the high voltage on the thyratron plate to recover its full initial value before a new event triggers it again, a 2 ms dead-time is applied to the stopping muon coincidence circuit after each operation. Thus with the normal burst length of the synchro-cyclotron (200 μs) only one muon can be handled per burst (55 per s): this was the method of running with the storage magnet. For measuring the injected beam, however, we used stochastic operation of the cyclotron giving a long duty cycle.

With the 2 cm thick target the number of gated decay electrons is 20 % of the total number of stopped muons, as a result of the following factors. To the loss of 45 % due to decay, and 20 % from the muons not stopping in the target, must be added the absorption in the methylene iodide which is as much as 50 % because the bad geometry increases the real average thickness. This last loss is, however, harmless since the increase in asymmetry due to hardening of the spectrum compensates for the loss in statistical accuracy. Geometrical losses in our close slab geometry are small.

4·2. *Counters and time measuring circuitry.* – The functions of the electronics are:

i) to measure accurately the time the muon spends in the magnet;

ii) to detect a stopping muon and trigger the pulsed field which flips its spin through $\pm 90°$; and,

iii) to detect the decay electrons emitted backwards and forwards.

4·2.1. Detector assemblies. Overall views of the injection counter assembly, the ejection counters and the polarization analyser are seen in Figs. 44, 41 and 51.

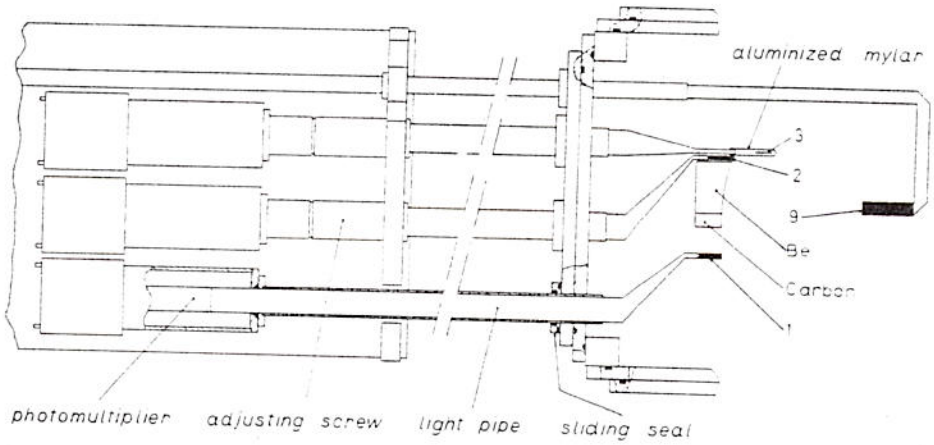

Fig. 44. – Injection counter assembly. 1) plastic scintillator, 4 cm wide × 3 cm high × × 0.8 cm thick; 2) plastic scintillator, 4 cm wide × 3 cm high × 0.8 cm thick; 3) plastic scintillator, 2 cm wide × 8 cm high × 0.04 cm thick; 9) plastic scintillator, 2 cm wide × × 2 cm high × 8 cm thick. All counters and the moderator adjustable in x-direction by sliding seals. The light pipe of No. 9 passed below the median plane, permitting storage out to $x = 150$ cm to be studied. This counter was removed for the main experiment.

All the detectors are plastic scintillator NE 102 (*) glued onto plexiglas light guides. In the case of counter 3, however, the light is collected by means of an aluminized mylar tent, through which the particles can pass for the first few turns; 10 cm from the scintillator the light enters a standard plexiglas light pipe. In the injection assembly each counter can be displaced by known amounts without breaking the vacuum so as to optimize the injection. The counters of the polarization analyser are clamped together with spacers such that their position is always reproduced with respect to the magnet. During storage studies a counter (No. 10) with a 4 cm diameter, 600 cm long, light guide was used from the ejection end of the magnet without difficulties over the light collection efficiency. The other light guides are long enough (~ 60 cm) for the photomultiplier housings to be well outside the main magnetic field. The residual field at the photomultiplier location is < 40 G. The multipliers

(*) Nuclear Enterprises Ltd., Edinburgh.

are shielded by 5 mm soft iron and 2 concentric mumetal shields of 1 mm. All photomultipliers are of the type 56 AVP and the current drain of the resistance chain is about 4 mA at the operating voltage of 2.4 kV. All counters have anode and last dynode signal outputs of 125 Ω terminated by their characteristic impedance at sending and receiving end; no clipping lines are used. The signal from the last dynode is inverted by a fast pulse transformer which introduces negligible distortion and reflection. Dynode outputs are used whenever one counter is used in two different circuits. For instance, in the counter assembly 566′ 77′ the combination (566′ $\overline{7}$) is used as a muon stop signal and the combinations (66′ $\overline{74}$) and (77′ $\overline{6}$′ $\overline{4}$) are used in the decay electron telescopes. The fast timing signals for muon flight-time are the anode outputs of counters 2 and 4, whereas the inverted signals from the last dynode are used in the gating coincidence circuits (123) and (4566′7).

TABLE V. – *Electrical characteristics of the counters used.* *A*) adjustable under vac.; *G*) selected tube for good signal-to-noise ratio; *S*) specially shielded against pulses from spin flipper; *T*) counters used for accurate timing anode outputs; *D*) dynode output used as well as anode output.

1	2	3	4	5	6	6′	7	7′
A	*A*	*A*						
		G	*G*	*G*				
				S	*S*	*S*	*S*	*S*
	T		*T*					
	D		*D*		*D*	*D*	*D*	

4·2.2. Coincidence circuits. The coincidence circuits used at injection (No. 1, 2 and 3), ejection (No. 4, 6, 6′, 5, $\overline{7}$), and for the polarization analyser are diode coincidence circuits with a common clamp diode ([22,23]). They are capable of a resolution of 5 ns (full width at half height) when used with artificial delay-line shaped pulses. Diode pulse limitation is provided at the input. The input to the coincidence circuit is terminated by 125 Ω or else can continue via 125 Ω cable to a number of similar circuits in turn, the last one only being terminated by 125 Ω. The height of pulses in four-fold coincidence, giving no break-through in five-fold coincidence, exceeds by more than 30 db the

([22]) R. L. GARWIN: *Rev. Sci. Instr.*, 24, 618 (1953).
([23]) C. M. YORK: unpublished.

pulse height needed for five-fold coincidence. The coincidence output is detected by a fast transistorized discriminator with a 12 V positive scaler driver and a —4 V output which, when terminated with 125 Ω is 50 ns wide. The negative output goes also via a 20 ns lumped delay-line to an anticoincidence gate followed by a similar discriminator. The anticoincidence gate allows us to veto any multifold coincidence circuit of this type by the output of any other, or directly by a photomultiplier pulse.

All circuits are transitorized ([23]).

4·2.3. Injection assembly (Fig. 44). The signal for a muon injected into the magnet is the coincidence 123. Counters 1 and 2 ensure that the muon passes through the whole thickness of the moderator. Counter 3 is not in line with counter 2 but is placed ~ 2.5 cm further forward in x so that particles must make ~ 2 turns before reaching it. Its width in x is $\sim$ step-size (2 cm) and its thickness 0.4 mm to minimize rescattering of the particle. As after 2 turns the particles have reached the maximum of their vertical oscillation, the particles which give a 123 coincidence have a high probability of being stored. The requirement that the muon counts in 3 reduces the counting rate of the input telescope by rejecting those particles which scatter out of the magnet in the first 2 turns. It thus decreases the dead-time of the digitron logic (see below), and the overall detection efficiency for useful particles is increased.

In the injection telescope, there is some time jitter which cannot be eliminated. Due to differences in injection angles and vertical oscillations after the moderator, the number of turns the particle makes before passing through counter 3 varies. Since one turn takes about 6 ns, the time of pulses (12) and 3 varies by multiples of 6 ns around the mean value set by delay timing. To embrace this jitter the pulse from 3 is lengthened to 20 ns by a fast trigger. On the other hand an uncertainty in timing as great as 6 ns cannot be tolerated; for this reason the coincidence (123) is used only to open a gate for the fast photomultiplier pulse from the anode of counter 2, which defines the arrival time of the muon.

4·2.4. Output telescope (Fig. 1 and 61). Muons emerging from the the magnet are detected by counter 4, which is thin (2 mm), to minimize scattering. As we are interested only in muons which stop in the correct part of the polarization analyser, the signature $(466'5\bar{7})$ is used to gate the fast signal from the anode of counter 4. Counter 4 then gives the accurate output timing signal.

4·2.5. Decay-electron selection. The arrival of the muon as indicated by the coincidence $(466'5\bar{7})$ initiates the flipping of the muon spin.

In order to allow time for spin flipping, only electrons emitted later than 1.1 μs after the muon has stopped are accepted. The time during which decay electrons are accepted is 5 μs. To measure background, provision is also made to count events occurring in an identical interval of 5 μs, starting 6 μs before the muon stop signal. Figure 45 shows the decay electron logic and the time relation

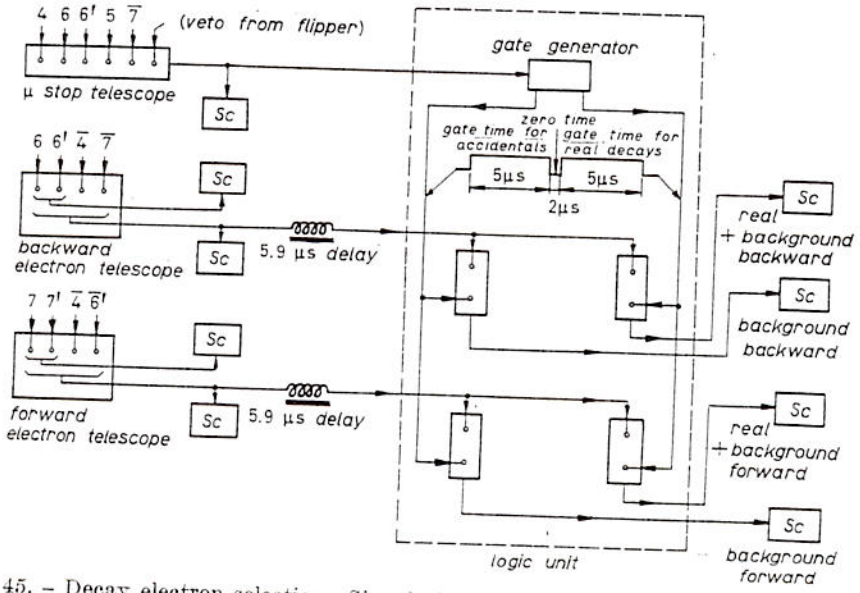

Fig. 45. – Decay electron selection. Signals from $77'\bar{4}\bar{6}'$ are selected by two 5 μs wide gates centred as shown about the muon stop signal $466'5\bar{7}$ to count (real+background) events (late gate) and background only (early gate). Similarly for the other electron telescope signature $66'\bar{4}\bar{7}$. The (real+background) signal was sent to the digitron to activate the « forward » and « backward » flip-flop; see Fig. 46.

of signals. The decay electrons are indicated by coincidence (66′) and (77′).

A beam anticoincidence input is also provided, rejecting any electron count which coincides with an incoming beam particle. There is also a « cross-veto » between (66′) and (77′), rejecting the output of the forward and backward electron telescope when both count simultaneously. The « beam-anti » and « cross-veto » are essential while measuring the polarization of the *injected* particles at high counting rates.

4·3. *Digitron* (Fig. 46). – The function of the digitron is to measure accurately and correctly the time of flight of the muon in the magnet. The muons are classified according to their flight-time in 100 ns bins. For each interval the decay electron asymmetry is determined by recording separately the number

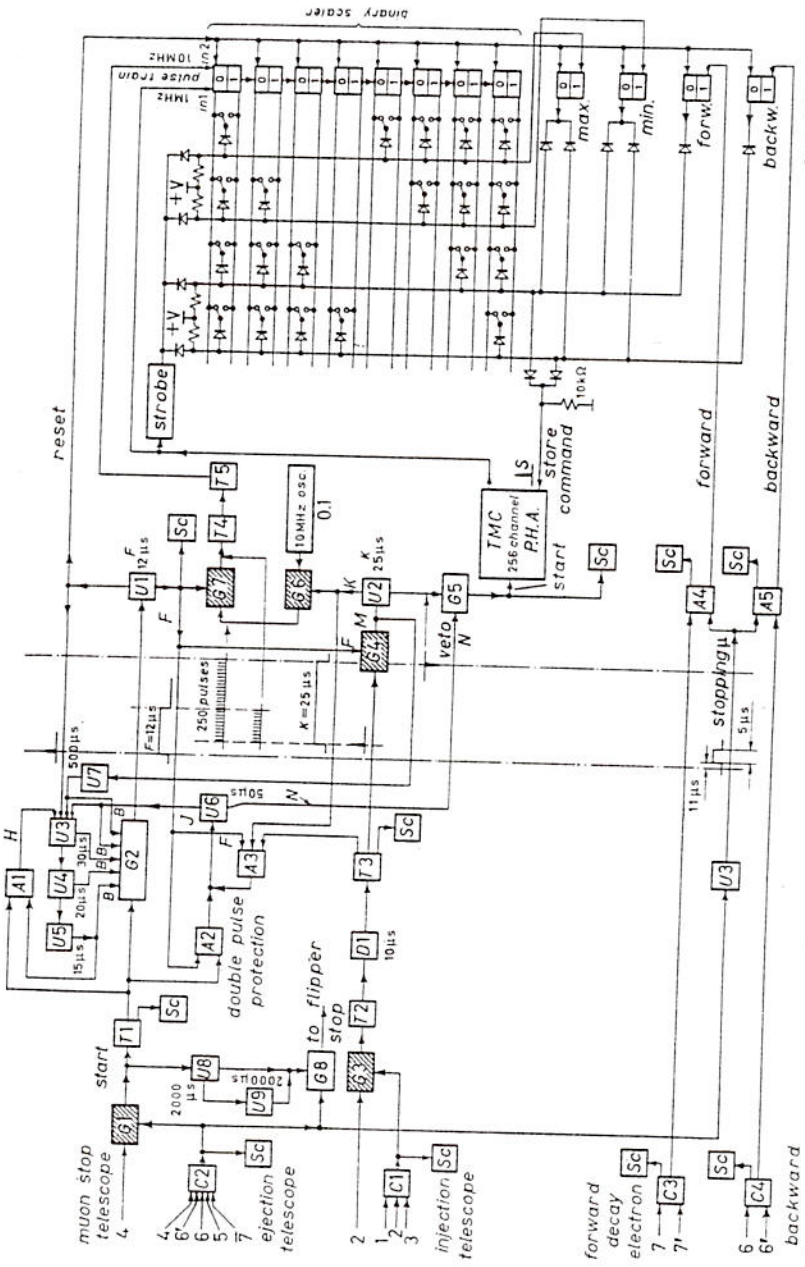

Fig. 46. – Block diagram of digitron and associated circuits. *C*, fast coincidence; *SC*, scaler; *T*, fast trigger; *A*, « and » circuit (slow coincidence); *U*, univibrator; *G*, gates, shaded (normally shut), unshaded (normally open); *D*, delay.

of decay electrons emitted forwards and backwards, with $+90°$ and $-90°$ spin flipping.

The runs are normalized for equal numbers of stopping muons integrated over the whole time spectrum. Note that fluctuations in this normalization (due, for example, to changes in the shape of the storage-time spectrum) produce corresponding errors in the backward and forward telescopes, which cancel out in the overall mean.

The digitron contains, as an essential feature, circuits for rejecting events with more than one signal at injection or ejection within 12 μs. Such events could otherwise be incorrectly timed because there is no way of associating correctly the signals with the wanted particle. During the run about 15 % of the particles were rejected because they were accompanied by a second injection count. During the testing of the digitron at high counting rates, the rejection circuits are even more essential.

While the digitron is processing a particular event, it is dead to all further input signals.

Since there are ~ 100 times more particles at injection than at the output of the magnet, the output particles are used to initiate the sequence of operations in the digitron. When a single unaccompanied count is obtained at ejection the digitron looks for the corresponding injection signal suitably retarded by a delay line. If both signals are present, the timing process is initiated. In this way the rate of loss of events due to digitron dead-time is much reduced.

4·3.1. Working principle of the digitron. The block diagram of the digitron is shown in Fig. 46. The circuit is somewhat modified from that described by SWANSON [24], notably in that it uses a free running 10 MHz crystal-controlled oscillator, instead of a pulsed oscillator, and in that it is completely transistorized. Also the dead-time and confusion rejection circuits are inspired from those of digitron MkV [25], with a few necessary improvements.

The principle is to open a gate for a time whose length is determined by the time interval between the two photomultiplier pulses. Pulses from the 10 MHz crystal-controlled oscillator are counted through this gate, into the digitron scaler, which then determines the address in which the event is to be recorded in the ferrite memory of a modified pulse-height analyser. As a result, the time interval to be measured is digitized in increments of 100 ns.

For a fixed time interval the result of the measurement is statistically distributed between two neighbouring 100 ns channels. The ratio of events in the two channels then determines the time interval precisely. Note that

---

[24] R. A. SWANSON: *Rev. Sci. Instr.*, **31**, 149 (1960).
[25] R. A. LUNDY: *Rev. Sci. Instr.*, **34**, 146 (1963).

in the experiment many counts must be accumulated in each channel to determine the decay electron asymmetry A. The statistical error in time determination then becomes negligible in comparison with the error in A. The limiting accuracy, ~ 1 ns, is set by the stability of the triggering level of the circuits involved and has been determined experimentally.

4·3.2. Digital conversion of time intervals into number of pulses. The gated fast signal from counter 4 (start signal) passes the normally open dead-time gate G_2 (see Fig. 46), and triggers the F-pulse of exactly 12 μs, defined by a delay line. The stop signal from counter 2 is gated by F at G_4 and then generates the 25 μs pulse K which gates the 10 MHz clock pulses at G_6. The resulting pulse train is gated again by the pulse F at G_7. In this way the 10 MHz pulses which fall in the overlap of pulses F and K are passed to the re-shaping triggers T_4 and T_5, and counted via input 1 in the 256-binary scaling system previously re-set to zero by pulse V. The number of pulses is a measure of the time difference between start and stop.

This number is determined by the interval between the rising edge of pulse K and the moment when pulse F falls back. So the total length of pulse K need not be accurately constant; however, the starting time of K and F, as well as the total length of F must be accurately fixed.

4·3.3. Transfer of the timing information to the memory of the TMC multichannel analyser. Once the time interval is stored in digital form in the digitron scaler, this information must be transferred to the appropriate channel of the multichannel analyser. For this purpose the T.M.C. analyser is fitted with a special plug-in unit. The unit is triggered by a negative pulse (trailing edge of pulse K via G_5), and then generates a series of 1 MHz clock pulses which advance the internal address register of the analyser and at the same time are fed into input 2 of the digitron scaler. This adds to the count already accumulated from the 10 MHz pulse train, and the process continues until the scaler matches a number preset on toggle switches. A store command signal is then sent to the analyser, stopping the address counter and adding one count into the corresponding analyser channel. (A C.D.C. 100-channel analyser has also been used in previous runs. In this case the method used to transfer the data was slightly different; we gave the analyser a large pulse to analyse, thus starting the clock pulses which were fed back to the digitron as above.)

4·3.4. Memory splitting. The position of the time spectrum in the analyser memory is clearly determined by the preset match number set on the toggle switches. In fact this match requirement is varied with auxiliary logic to route the spectrum into different parts of the analyser according to

whether a forward or backward decay electron has been detected. This is achieved with diode gates, the *forward* and *backward* flip-flops allowing the appropriate line of switches to be effective when triggered by the corresponding decay electron count.

If the memory is thus split into two, it is essential to impose rigid cuts at each end of the time spectrum; otherwise the tail of the spectrum belonging to one half of the analyser could intrude on the other half. This is achieved by imposing a maximum and minimum 10 MHz count by means of two additional lines of switches which activate the *maximum* and *minimum* flip-flops. If the imposed condition is violated the *match* signal is never generated and the analyser runs to overflow without storing.

Note that if the decay electron from the muon is not detected, the time-of flight is again not registered in the analyser. However, for certain tests we can arrange to suppress the electron requirement and activate the match circuits for every muon stopping in the analyser.

4·3.5. Dead-time circuits, and protection against double pulses. As the timing accuracy depends on the stability of the 12 μs F-pulse, it is essential to allow this trigger plenty of time to recover before being retriggered by another pulse. Accordingly the dead-time gate G_2 is held shut for 65 μs by the univibrators U_3 (30 μs), U_4 (20, μs) and U_5 (15 μs), which are triggered in succession. This arrangement ensures that these triggers are *never* asked to work during their recovery periods, so the dead-time can never run short.

If a particle is accepted for timing (K-pulse present) then the univibrator U_7 is activated prolonging the dead-time for 500 μs, which allows time for the transfer process to the multichannel analyser. After this the normal dead-time of 65 μs is recycled so that U_7 has time to recover before being fired again.

Double pulses on the start input are rejected as follows. Normally the first pulse triggers the 12 μs F-pulse. The second pulse is then detected in coincidence with F by the coincidence circuit A_2, which generates the 50 μs veto pulse (U_6), which closes gate G_5 and prevents the transfer of the number to the multichannel analyser. Thus, such an event is partially processed, but the result never reaches the analyser.

This protection fails if the first of the two pulses falls in the dead period associated with a previous event: the second pulse is then free to trigger the F-pulse, and no veto is generated. To avoid this we ensure that an input pulse can never occur during the last 15 μs of the dead-time. If it does, the dead-time is recycled. Coincidence circuit A_1 detects input pulses during the final 15 μs (U_5) and retriggers the dead-time cycle at U_3. The dead-time will continue to recycle until a 15 μs clear period at the end is encountered. As all dead-times end by recycling the 65 μs U_3, U_4, U_5 series at least once, this protection is always valid.

Double stop pulses both falling inside the 12 μs F-pulse are rejected as follows. The first triggers K, and the second is then detected by the coincidence circuit A_3 and triggers the veto signal U_6 already discussed above.

If a second stop pulse is present but falls outside the F-pulse, it does not veto the event. Such a signal can never correspond to a genuine event as it would mean a flight time through the magnet less than -2 μs, or more than $+10$ μs, both of which are impossible: so no confusion is possible in this case.

Note that U_6 is as usual protected against premature retriggering, because the 65 μs dead-time is recycled as usual when U_6 re-sets.

4·3.6. Time measurement. The 12 μs pulse length of U_1 is accurately controlled by an HH 1500 delay line. This is necessary for two reasons:

i) the length of the F-pulse must be very well fixed and for this reason the pulse length must be defined by a delay line as explained previously;

ii) a similar 10 μs delay line is used in the stop line. These lines have a temperature coefficient of -0.04 %/°C. However, a temperature variation in one is largely compensated by a similar variation in the other, and the storage channel is not affected.

Now, consider an event corresponding to flight time zero. Since there is a 10 μs delay in the stop line, the 25 μs pulse from U_2 starts ~ 2 μs before the end of the 12 μs F-pulse. The number of 10 MHz pulses gated through G_6 and G_7 is 20 and corresponds to zero time.

In fact, the stop pulse (injected μ) can arrive as much as 2 μs later, corresponding to 2 μs of negative flight time in the magnet: this is, of course, unphysical and used to measure background. The stop pulse (injected μ) can also arrive up to 10 μs earlier than the start and in this case there are 120 pulses passed through the gates. This corresponds to 10 μs of storage time. More storage time cannot be examined with the 10 μs delay line, since earlier stop pulses cannot come through G_1. By changing the delay lines this range can be extended.

In the main experiment we used a 256-channel TMC analyser. At first we split this into two blocks of 128 channels (for forward and backward decay electrons), so that we could display the whole 12 μs range of time. The range from 1.8 to $+1.8$ μs was used to determine the background, which was thus measured with sufficient accuracy for correction to the whole run.

For the majority of the run, however, we split the analyser into four blocks of 64 channels displaying only the useful 6 μs region of time from 1.9 to 7.9 μs. We accumulated simultaneously in two blocks the information for backward and forward decay with $+90°$ flipping of the muon spin, and then without clearing the analyser switched to $-90°$ flipping using the other two blocks. Thus, no time was wasted in printing and clearing and we

were able to run automatically, reversing the direction of flipping every 1000 stopping muons ($\sim$20 min), so minimizing errors due to drift.

4·3.7. Calibration and checking of the digitron.

i) Zero time. The exact fractional channel location of zero time of the digitron itself can be obtained by feeding the same pulse into start and stop input simultaneously. In this case, one can either open the gates G_1 and G_3 permanently by applying +6 V to the gate inputs, or supply a coincident gating pulse to both inputs. Care has to be taken that the repetition rate of the input pulses to start and stop is not too high, otherwise the dead-time circuits are always operative and no storage occurs. The timing stability of the digitron has been tested in this way.

In the actual experiment one must know the location of zero time as given by the injection and ejection counters when they receive time-coincident particles. There is a small difference between this zero time and the zero time given by the digitron alone, arising from transit time differences in the photomultipliers and differences in the signal cables connecting them to the digitron. We obtain the zero time calibration by inserting the ejection counter 4 into the injection beam. With this zero the electronics measures, in effect, the μ flight time between the two positions of counter 4 while we require the flight time in the magnet itself. Therefore, a small calculated correction is applied to account for the flight time from counter 4 (injected beam position) to the magnet, and from the magnet to counter 4 (ejection position). This calibration has been repeated at various times and showed no significant variation.

The *stability of zero time* has also been checked repeatedly during the experiment by connecting the counter 4 signal cable to the counter 2 output with a matched T. When cable 4 was not connected to the T, it was replaced there by a 125 Ω termination. This procedure allows quick checks of zero time stability once the difference due to transit time in the multipliers is known.

Various measurements showed no effect of the repetition rate on zero time.

ii) Checking of time scale. The number of nanoseconds per channel is determined by the frequency of the CW oscillator. This frequency has been measured with a Hewlett-Packard frequency-meter and found to be (9.995 ± 0.001) MHz. Variation of the time scale was also measured at various ambient temperatures and found to be negligible.

iii) Linearity check. By feeding pulses into start and stop input with random time relation, one can check the differential linearity of the whole system. This has been done with widely different rates at both start and stop inputs.

No effect of the repetition rate on the linearity was found. All channels gave the same count to better than 0.2 %. This checks not only that the channel width is constant, but also that the protection circuits were operating perfectly.

5. – Polarization of the input beam.

5·1. *Polarization as a function of muon range.* – The same apparatus is used for measuring the polarization properties of the muon beam before and after storage in the magnet in order to cancel minor directional errors. However, for studying the beam before injection a thin target of methylene iodide (8 mm thick) is used, so that the polarization of the beam can be measured as a function of the muon range. The spacing of the counters remained unchanged, the vacant space being filled with styrofoam which kept the target in place.

The 150 MeV/c π^+-μ^+ beam of the CERN Synchro-cyclotron was deflected 20° by an analysing magnet, and focused by a pair of quadrupoles into a slit 3 cm wide × 8 cm high, 2 m from the second quadrupole. This distance corresponded to the distance from quadrupole to beryllium block in the run with the storage magnet. After the slit the beam was monitored by two counters each (7 × 7 × 0.8) cm, and then passed through a further collimator 8 cm wide × × 6 cm high into the polarization analyser, see Fig. 40. The 8 cm Be absorber (the same one used in the storage run) plus variable carbon was placed in front of the second collimator. Only the central section of the polarization analyser was illuminated with muons in these measurements. The counter assembly and collimators were aligned with a beam trajectory previously established with floating wire.

In principle a variation of counter efficiency from side to side in No. 5 would lead to errors in the angle measurement; but calibration of the efficiency with beam particles showed that this did not occur, and, moreover, the forward and backward telescopes gave identical results within statistical error.

A stopping particle was indicated by the coincidence $12\,6'5\overline{7}$, while backward and forward decay electrons were indicated by $6\,6'(\overline{1}\overline{2})(\overline{7}\overline{7}')$ and $7\,7'(\overline{1}\overline{2})(\overline{6}\overline{6}')$. That is, the electron count was vetoed if accompanied by an incoming beam particle giving a 12 coincidence, and also vetoed if a simultaneous count occurred in the other electron telescope. This reduced background due to the beam, and background due to decay electrons originating in the beryllium block and surrounding materials.

The flipping of the spin was initiated by the stopping muon signal, and the electrons were counted in a 5 μs gate delayed 1.1 μs, as already described.

With 0° and 180° flipping we measured the magnitude of the asymmetry $A_\parallel$ available with this beam and counter geometry. Then with 90° flipping we measured the asymmetry $A_\perp$ due to the transverse component of the muon spin. This gave the spin angle $\theta_s = \mathrm{tg}^{-1}(A_\perp/A_\parallel)$, independent of any pion contamination.

The results which are given in Fig. 47, together with the range curve of the stopping particles, show that the A-value increases with muon momentum, while the spin angle changes 10° per cm of range in carbon, passing through zero near the peak of the range curve. The strong dependence of spin angle on range means that to know the mean spin angle at injection we would have to know very accurately the mean range of the particles which are accepted by the magnet and passed through to the analyser at the ejection side. In the 0.4 % experiment we avoided this problem by reducing the magnitude of this range-dependence by the use of a solenoid.

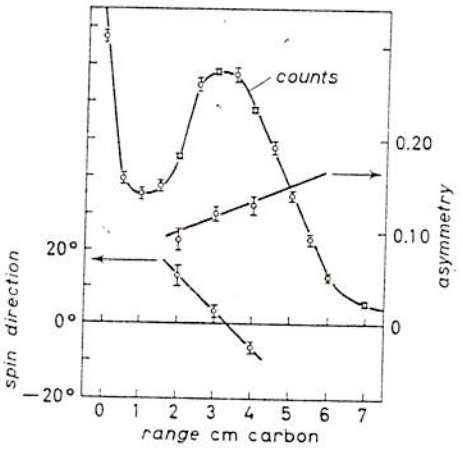

Fig. 47. – Muon range in injected beam showing also effective asymmetry coefficient and muon spin angle *vs.* range. Note the strong angle-range correlation obtained before the solenoid was added.

The range-dependence is due to the preferential selection of certain pion decay angles when the muons are born inside the cyclotron magnet. Muons whose momentum is the same as the pion momentum in the pipe must originate somewhere along a line which runs back into the cyclotron magnet and passes through the cyclotron target. Pions must decay forwards on the average to give such muons. Muons of lower momentum originate along a more sharply curved line which passes outside the cyclotron target, and here right-handed pion decays predominate (*). High-momentum muons, on the other hand, originate on a line which passes inside the cyclotron target, and require predominantly left-handed decays. This explains the slope of horizontal spin direction *vs.* range seen in Fig. 47; but because of the symmetry of the cyclotron with respect to its vertical median plane, no such correlation with the muon momentum can exist for the vertical transverse component of the muon spin.

We therefore arranged to interchange the vertical and horizontal transverse components of the muon spin. This was achieved by passing the beam coming from the cyclotron through a longitudinal magnetic field produced by a sole-

(*) The magnetic field in our cyclotron is ↓.

noid of length 200 cm (see Fig. 48). The field and length of the solenoid are chosen to rotate the transverse component of the muon spin by 90°, whereas the component along the axis of the solenoid is not affected. For our 150 MeV/c muons and 200 cm available length, a magnetic field $B = 3\,950$ G is required to obtain 90° rotation.

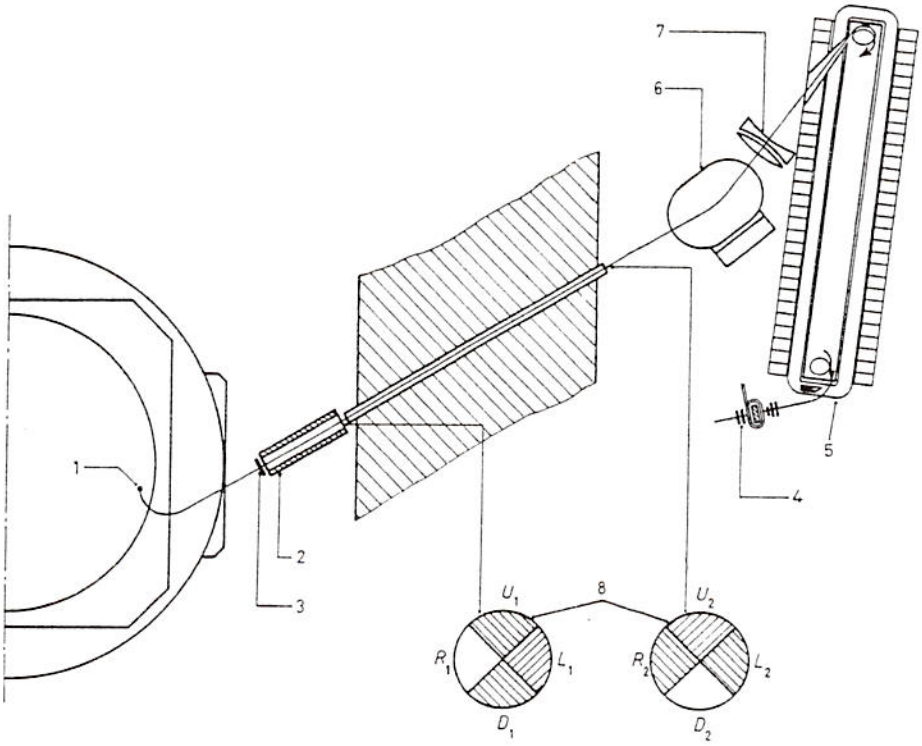

Fig. 48. – Final layout of experiment, showing cyclotron, solenoid, pipe through shielding wall with the possibility of dividing each end of the pipe into quadrants to study beam structure. Note the lead scattering foil added to scramble the muons into different beam cells, thus reducing spin-angle/position correlations. 1) target; 2) solenoid; 3) lead foil; 4) polarization analyser; 5) storage magnet; 6) bending magnet; 7) quadrupole lenses.

The polarization was re-measured with the *solenoid on* as a function of range with the results of Table VI, which are plotted in Fig. 49. The results of a least-squares fit to this data are

(86) θ_{beam} (at range $X = 10$ cm carbon) $= -(0.5 \pm 12)$ mrad ,

(87) and slope $(\mathrm{d}\theta/\mathrm{d}R)_{\text{beam}} = -(19 \pm 12)$ mrad/cm .

TABLE VI. – *Polarization of whole input beam vs. range with solenoid on.*

Range (cm carbon)	θ_{beam} (degrees)
8	2.12 ± 1.0
8.5	1.36 ± 0.44
9	2.0 ± 1.5
9.5	1.4 ± 1.7
10.5	0.3 ± 1.7
11.0	-1.9 ± 1.3

(Note that X is the thickness of carbon absorber: the true range R involves counter thickness, etc., and is discussed in Sect. 6·2.)

In spite of this reduction in the range-dependence of the transverse polarization in the horizontal plane, we still need to apply a correction for the mean range of the stored particles, as described below, see Sect. 6·2 and 7·1.

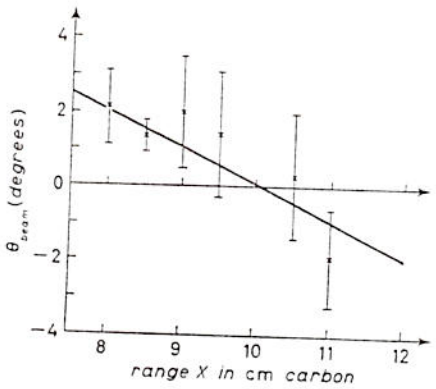

Fig. 49. – Spin angle *vs.* range with *solenoid on.* (For range curve, see Fig. 53.)

5·2. *Variations of polarization in different parts of the beam.* – Because the magnet only stores about 1% of the input beam, the polarization measured for the whole beam is not necessarily that of the partial beam selected by the magnet. It is therefore essential to check whether the polarization angle is the same in different parts of the beam. The beam in the circular pipe (4 m long × 14 cm diameter) through the cyclotron shielding wall is subdivided by placing at the entrance and exit of the pipe two brass absorbers, each of which leaves open only one quadrant of the pipe (see Fig. 48). The four possible positions of each quadrant are combined to divide the beam into 16 independent cells in phase space. For each cell the direction of arrival at the analyser θ_p^i is measured with slits, and the spin angle θ_s^i determined as above. This gives $\theta^i = \theta_s^i - \theta_p^i$ for each of the 16 cells ($i = 1$-16). The slits for measuring θ_p^i consisted of slit 1 (5 cm wide) after the quadrupoles and slit 2 (1 cm wide) in front of the carbon absorber. A typical set of results is given in Fig. 50. The dependence of θ_p^i on the range was measured to be negligible. Notice that the error in θ_p^i was always negligible. These measurements showed strong variations of the order of 20° in the value of the polarization angle from cell to cell.

To eliminate this effect, the beam structure was scrambled by means of a scatterer (1 mm lead foil) placed close to the cyclotron. Muons which originally belonged to one cell were thus distributed over many cells, and the polarization angle in each cell was more nearly an average over the whole beam, and therefore the same from cell to cell. The values of polarization angle θ^i obtained with the lead foil in position are shown in Table VII, together with the fractions of the intensity W^i_{beam} and W^i_{mag} contributed by each cell to the whole beam, and to the particles stored in the magnet. Because $W^i_{\text{mag}} \neq W^i_{\text{beam}}$ the average polarization angle for the beam accepted by the magnet,

$$\theta_{\text{mag}} = \sum W^i_{\text{mag}} \theta^i \,, \tag{88}$$

differs from that for the whole beam,

$$\theta_{\text{beam}} = \sum W^i_{\text{beam}} \theta^i \,, \tag{89}$$

but can now be determined.

Using Eqs. (88) and (89) with the data of Table VII, we find that the correction to be applied to the measured beam polarization to correspond to the beam selected by the magnet is

$$\theta_{\text{mag}} - \theta_{\text{beam}} = 1.04 - 1.46 = \\ = -0.42^\circ = -7.3 \text{ mrad} \tag{90}$$

at range 8.5 cm.

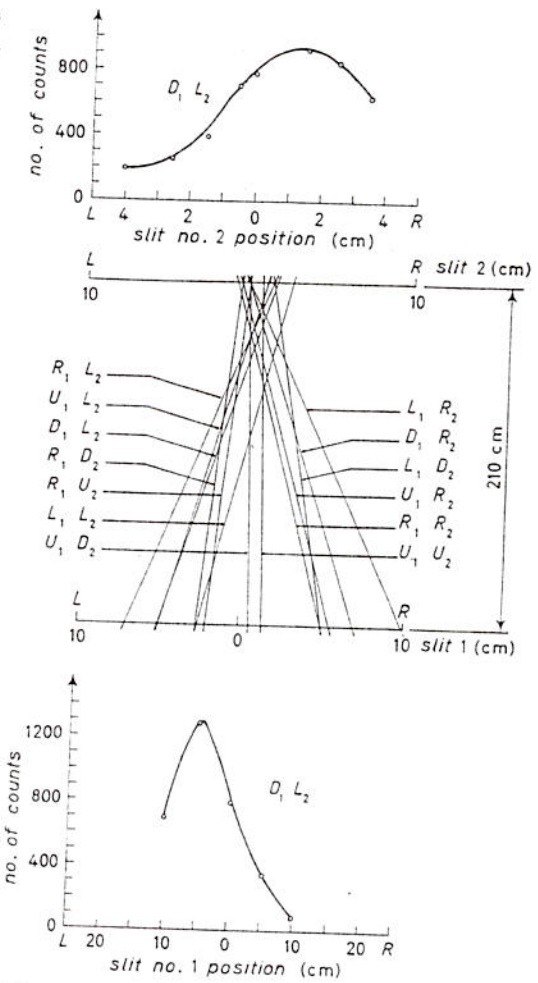

Fig. 50. – Angles of muon arrival θ^i_p for the 16 cells as measured by slits. Typical response curves obtained on moving the slits are also shown.

The correct determination of the average input polarization of the stored beam is complicated by the small, but nonnegligible range-dependence of the polarization angle. It was impossible to predict precisely the average range that the magnet would store, and in fact the detailed input beam measurements

TABLE VII. – *Polarization angles θ^i for input beams divided into 16 parts at $R=8.5$ cm, with contribution W^i_{beam} and W^i_{mag} of each part to the total intensity, in the beam, and stored in the magnet. The uncertainty in the fractional intensity W^i contributes negligibly to the error.*

Cell	θ_{beam}	θ^i (degree)	W^i_{mag} (%)	W^i_{beam} (%)
1	+0.0	−1.64±1.4	8.7	11.9
2	−1.1	+2.80±2.3	5.4	3.1
3	+0.1	+2.00±2.0	2.9	2.2
4	+1.4	−1.14±1.5	7.9	15.0
5	+0.5	+1.20±1.6	10.1	12.3
6	−1.0	+4.46±1.8	9.4	8.0
7	+0.6	+4.00±1.2	4.7	4.1
8	+1.7	+1.26±2.1	5.3	8.1
9	0.0	−0.22±1.6	6.5	5.6
10	−1.0	+2.41±2.6	5.3	2.7
11	+0.0	+4.81±1.3	4.9	2.2
12	+1.4	−2.50±2.5	7.3	5.6
13	−0.5	+1.16±1.3	6.6	6.2
14	−1.1	+1.67±2.6	2.6	1.1
15	−0.5	+3.46±1.2	3.5	1.9
16	+1.0	+3.30±1.0	8.5	9.9

of Table VII were made at range $X = 8.5$ cm carbon, while the equivalent injection range of the stored particles corresponded more nearly to $X = 10$ cm.

It is now a question whether the correction for spatial structure of the beam polarization determined at $X = 8.5$ cm, eq. (90), is valid at $X = 10$ cm. We have

$$(91)\quad \theta_{\text{mag}}(R_2) - \theta_{\text{beam}}(R_2) = \sum W^i_{\text{mag}} \left\{\theta^i(R_1) + \frac{\mathrm{d}\theta^i}{\mathrm{d}R}(R_2 - R_1)\right\} - \\ - \sum W^i_{\text{beam}} \left\{\theta^i(R_1) + \frac{\mathrm{d}\theta^i}{\mathrm{d}R}(R_2 - R_1)\right\}$$

$$(92)\quad = \theta_{\text{mag}}(R_1) - \theta_{\text{beam}}(R_1) + \sum (W^i_{\text{mag}} - W^i_{\text{beam}}) \frac{\mathrm{d}\theta^i}{\mathrm{d}R}(R_2 - R_1) .$$

Here it is assumed that the fractional intensities W^i do not vary appreciably with range: this point was checked experimentally.

The final term in eq. (92) is a product of small quantities: it was shown to be in fact small by measuring the range dependence $\mathrm{d}\theta^i/\mathrm{d}R$ for individual partial beams, as follows.

To measure $(\mathrm{d}\theta^i/\mathrm{d}R)$ for every cell would take a very long time because of the low intensity of muons in an individual beam. In fact, we measured $(\mathrm{d}\theta^i/\mathrm{d}R)$ for six cells only. These six cells, however, constitute 43 % of the

input beam and 46 % of the stored intensity. From these results we can show as follows that the final term in eq. (92) is negligible.

The individual values of $(d\theta'/dR)$ showed fluctuations ($\sim \pm 2°$/cm C), including changes of sign, but the effects largely cancel in summing over the whole pipe. To obtain the maximum possible value of the third term in eq. (92) we:

i) evaluate the term over the six cells for which we have information; this gives a partial correction of 0.01°/cm carbon; and,

ii) assume very pessimistically that for the cells we do not know $(d\theta'/dR)$ is about 2°/cm with sign always equal to the sign of $(W'_{mag} - W'_{beam})$; this gives a partial correction of 0.42° per cm carbon.

Hence, the overall correction (for $\Delta R = 1.5$ cm) is certainly less than 0.64° and can be neglected in comparison with our final error. We conclude that eq. (90) is valid at $R = 10$ cm.

Combining eqs. (86) and (90) we find at our standard range, $X = 10$ cm, the initial polarization of the beam accepted by the magnet is

$$\theta_{mag}(R_0) = -(7.8 \pm 12) \text{ mrad} . \tag{93}$$

Small corrections to other ranges are made by applying eq. (87), see Sect. 7·1.3.

Note that in the measurement of the partial intensities, W'_{beam} and W'_{mag}, cyclotron intensity was monitored by an independent counter telescope which recorded particles from the cyclotron target passing down another beam pipe. In the case of W'_{mag} we also recorded the storage time spectrum for the partial beams. The differences were negligible showing that the values of W'_{mag} are not functions of storage time.

6. – Measurement on the stored beam.

6·1 *Setting up the storage system.* – For injection to the storage magnet the beam described in Sect. 5 was used, the beam line after bending through 20° by the analysing magnet, being established by the floating wire technique. The injection line to the magnetic channel of the storage magnet was also determined by the floating wire method, and the magnet was positioned to make these two lines coincide. It was found possible to adjust the magnet with the aid of the air platforms to millimetre accuracy. The procedure for setting up the storage system was then as follows.

For initial measurements an auxiliary counter, No. 9, was introduced through the end plate at the injection end, as shown in Fig. 44. The light pipe ran

below the median plane, clipping the particles which made vertical oscillations greater than ± 2 cm, but leaving about one-third of the stored orbits for test measurements. The counter could be moved under vacuum along the centre line of the magnet as far as $x = 150$ cm, and adjusted vertically by rotating the light pipe. The scintillator was (1 cm high) $\times$ (2 cm in y) $\times$ (8 cm in x). Particles could miss the counter, above or below, on the first passage because of vertical oscillation, but the length (4 turns in the injection region, which is one-half period of the vertical oscillation) was sufficient to make the probability of a complete miss very small.

For the first measurement we observed coincidences 129 with No. 9 set to see particles emerging from the injection assembly and making half a turn in the magnet, an absorber being inserted to block further turns which would have spoiled the measurement. One may then regard the 129 coincidence system as a crude 180° spectrometer which selects muons in a given momentum band, and by varying the carbon absorber placed in front of the beryllium block one can make a very clean differential range curve. Having chosen the thickness of absorber one can then move No. 9 in and out and determine the diameter of the injected orbits: 2.2 cm of carbon in addition to the beryllium and counters were required to give $\varrho = 19$ cm, the chosen orbit radius.

The thin counter, No. 3, was at first lined up behind No. 2 to check its plateau and efficiency. It was then advanced into its correct position to intercept particles after 2-3 turns. Using No. 9 to start the digitron timing, and the coincident 123 as stop, we then obtained stored rates of 2.3/s at $x = 75$, and 0.7/s at $x = 175$ (~ 100 turns), showing a loss factor of ~ 3 in the transition region as expected.

The stored rate was determined here, and subsequently from the number *vs.* storage time picture presented by the digitron, the decay electron requirement being suppressed at this stage. The group of stored particles was clearly visible on top of the small and level background which was subtracted.

The position of the beam in the injection magnetic channel was now verified by alternately blocking the left-hand and right-hand side, and as a result the injection assembly was advanced 2 cm into the magnet to select particles which where more accurately centred in the channel. This improved the stored rate by a factor 1.5, and including the gain due to optimizing the bending magnet and quadrupole settings we then had at $x = 145$, a stored rate of 2.7/s, the injection telescope rates being (12) = 950/s, (123) = 106/s (but only a fraction of this is due to stored muons).

On removing No. 9, the 123 rate increased to 135/s (more particles can make 2-3 turns), the 12 rate remaining the same, and on observing at the far end with No. 4, we immediately obtained stored, ejected particles; we stopped 0.2 muons/s in the polarization analyser and observed 0.03 decay electrons/s.

After further trials to find the optimum conditions of magnet current,

moderator thickness and analyser position, we ran the first experiment [ref. (13)] at the rates shown in Table VIII.

TABLE VIII. – *Counting rates per second during the runs.*

	1st experiment	2nd experiment
Injection (12) coincidence	1100	1600
Injection (123) coincidence	170	180
Timed muons stopping in analyser	0.3	1.0
Timed muons with decay electrons detected	0.05	0.25
Loss due to rejection of multiple events	14%	13%

For the second experiment [ref. (14)] in which the solenoid was introduced in the input beam as described in Sect. 5, modifications were made to increase the stored rate. The magnet was re-shimmed to eliminate some residual x-dependence of the field, the iron block (see Fig. 61) was added at the output to improve the ejection, a new output window flush with the end of the magnet at $x = 600$ was used, and the injection assembly was rebuilt.

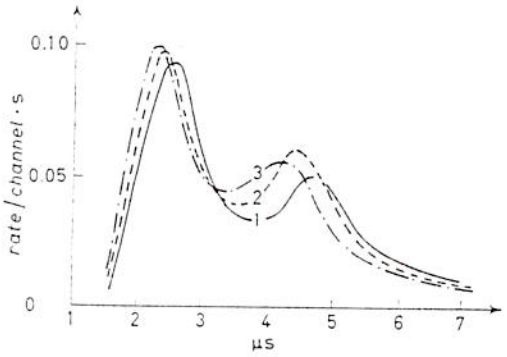

Fig. 51. – Storage time spectrum for muons at various magnet fields. (Compare predicted spectrum, Fig. 9.) Curve 2 is chosen as giving the best intensity in the region (4÷6) μs. magnet shunt reading: 1) 86.0 mV, 2) 86.4 mV, 3) 87.0 mV.

A detailed study of storage *vs.* magnetic field gave the results shown in Fig. 51; the optimum time spectrum and intensity being obtained in curve 2. The variations are understood in terms of sideways deflection of the walking orbits due to x variation of the field after injection. In fact by varying the magnet current we control the fringing field effects in the x direction, and throw the injected orbit centres into the optimum region of y. We choose a spectrum which gives many particles at 4 μs, where the $(g-2)$ precession wave crosses zero, and thus place the particles in the region that contributes most significantly to the final result.

Vertical and horizontal scans through the ejected beam gave the results indicated in Fig. 52. These show that at the ejection window the beam is only ± 2 cm wide at half height; such a concentration in the median plane is ascribed to increased vertical focusing in the steep-gradient ejection region.

At the analyser position the beam is still only ± 4 cm wide vertically, while horizontally the width at half height is 30 cm. (Cf. floating wire ejection measurements, Fig. 7.)

Accordingly the analyser was rebuilt with 30 cm wide counters (instead of 20 cm) to intercept more of the ejected beam. Also improvements in the pulser for flipping the muon spin allowed us to start counting decay electrons earlier.

These improvements gave a factor ~ 3 in the efficiency of the system, and including improvements in the cyclotron itself we were able to run the second experiment at the rates given in Table VIII: overall a fivefold improvement in the rate of data collection.

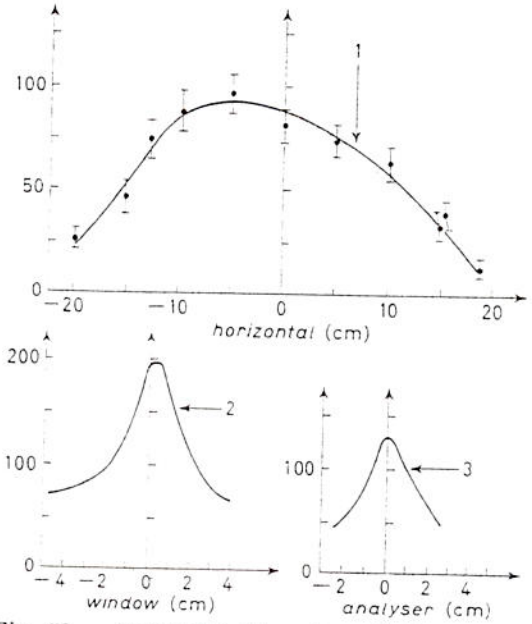

Fig. 52. – Horizontal (1) and vertical (3) scans through the ejected muon beam at position of the analyser (for scanning line see Fig. 7). Also vertical scan (2) at ejection window.

6·2. *Measurement of muon range, orbit centre and radius as a function of storage time.* – Measurement of the position and radius of the orbits as a function of storage time is necessary in order to compute the average magnetic field $\bar{B}_t$ as a function of storage time, and also to calculate the injection polarization which is slightly momentum-dependent.

Three distinct energy measurements have been performed on the stored particles: range measurements; comparison of the counting rate in the backward and forward telescope (B/F method); and probing of the position by means of flaps to find y_e and the orbit diameter. Here we describe the range measurements. Interpretation in terms of momentum and orbit radius is postponed to Sect. 6·3.

6·2.1. Range measurements. The same differential range detector, namely the polarization analyser itself, is used to determine the range of the muons injected into the magnet, and the range of the muons which are stored and ejected into the analyser. A careful evaluation of the quantity of matter traversed by the latter is necessary to establish the correspondence between the two range curves. The thickness of the beryllium moderator and the carbon

pieces used to slow down the injected beam is so chosen that the residual range corresponds to an orbit radius which is optimum for storage and ejection.

i) Injection beam. For a study of the injected beam the thick CH_2I_2 target is replaced by a thin CH_2I_2 target, since it is necessary to flip the spins to measure their direction as a function of range. This layer is equivalent, with the counter No. 5, to a window of 1.72 g cm^{-2} of carbon, and the range curve is measured with graphite absorbers.

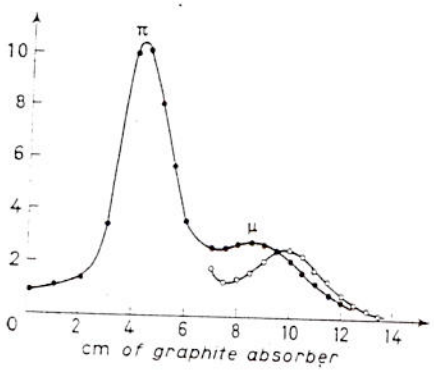

Fig. 53. – Range curves in injected beam with *solenoid on*, with and without lead diffuser: • lead diffuser in, ○ lead diffuser out.

The determination of the peak position of the muons at injection is rather uncertain (see Fig. 53) because of the pion contamination. However, we are not interested in the absolute value of the range but in the correspondence between the two ranges at injection and ejection. The use of the same detectors to define the stopping muons is an important factor of reliability in comparing the two ranges. Table IX represents the evaluation of the different factors contributing to the range of the injected muons.

TABLE IX. – *Range of the injected beam.*

Nature of absorber	Equivalent carbon in g cm^{-2}	Observations
Monitor counter 1 and 2	2.16	The window consists of 5 mm CH_2I_2, 2 mm of plexiglas walls of the container, and 3 mm of plastic scintillator (No. 5). The stopping power of the scintillator (*) relative to carbon is 1.18, the density is 1.05.
$\frac{1}{2}$ window	0.86	
Air 600 cm	0.78	
Counters 6 and 6′ each 8 mm thick	1.92	
2 mumetal walls, each 0.9 mm		
Scotch tape	0.10	
Total	7.00	

(*) University of California Radiation Laboratory Report UCRL-2301.

This table can be summarized by the relation giving the real range in carbon as a function of carbon thickness X (density of carbon = 2.05)

$$R = 7.00 + 2.05\,X \text{ g cm}^{-2}. \tag{94}$$

The peak is around 9 cm of carbon, corresponding to a total range of 25.45 g cm^{-2} of carbon (see Fig. 53).

ii) Ejected beam. The thick CH_2I_2 target is replaced by a thin copper sheet equivalent with the counter No. 5 to a window of 1.36 g cm^{-2} of carbon. The range is measured with plexiglas absorbers of the same dimensions as the polarization analyser because of the wide spread of the ejected

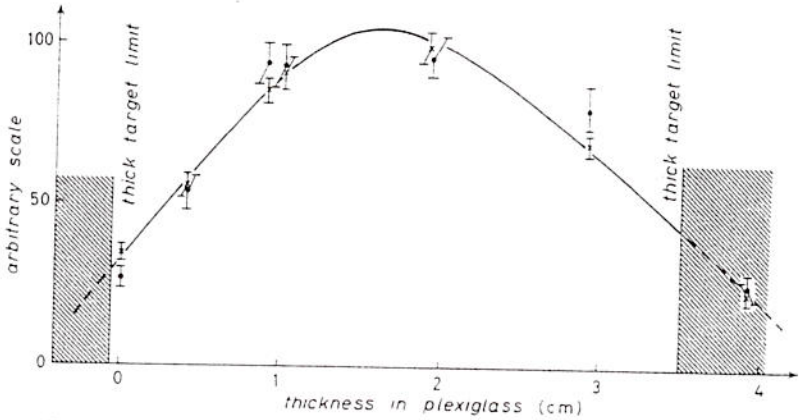

Fig. 54. – Range curve in *ejected beam* measured with thin copper target: × ejected muons stopping in the analyser, • idem with decay electron requirement.

beam. In the same runs the muons are identified as particles stopping in the window, with or without the additional requirement of being followed by a decay electron in the telescopes 66′ or 77′. The range curve is the same with or without this requirement (see Fig. 54). The peak of the range curve is at 1.6 cm of plexiglas. For each absorber thickness, the digitron gives us the corresponding storage time distribution; therefore we can determine the range curve as a function of storage time. The stopped muons are grouped in time intervals of 1 μs width with the results plotted in Fig. 55. There is a slight dependence of the range on storage time. In Table X we tabulate the mean range for each time band (see also Fig. 56). In calculating the average as a

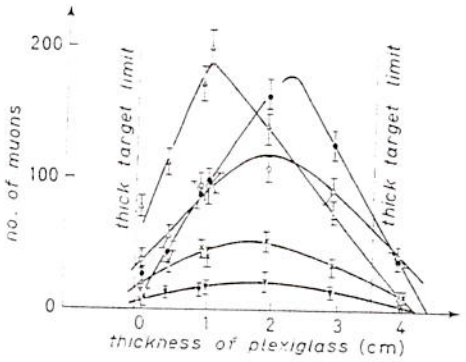

Fig. 55. – Range curve in *ejected beam* for various storage times. (The total data of Fig. 54 are divided into separate time bands.) • 2 to 3 μs, ○ 3 to 4 μs, △ 4 to 5 μs, × 5 to 6 μs, ▼ 6 to 7 μs.

TABLE X.

Time (μs)	Range (cm) (plexi)	Average radius $\bar{\varrho}$ (cm)	ΔR^t (*) (cm) (carbon)
2÷3	1.96	19.40	0.11
3÷4	1.76	19.15	0.01
4÷5	1.58	18.90	0.12
5÷6	1.64	19.00	0.09
6÷7	1.62	19.00	0.10
7÷8	1.56	18.90	0.14

(*) Gives range relative to the standard value corresponding to $X = 10$ cm carbon in the injection measurements, see below eq. (98).

function of storage time, the limits of the thick CH_2I_2 target indicated in Fig. 54 are taken into account (*). The real range of the ejected particles is calculated from the analysis summarized in Table XI of the total amount of matter traversed by the particles to stop in the middle of the thin window.

The range in carbon of the particles stopping in the analyser is therefore given by the relation

$$R_{ej} = 4.28 + 1.29\,X' \text{ g cm}^{-2}, \tag{95}$$

where X' is the thickness of plexiglas in front of the analyser.

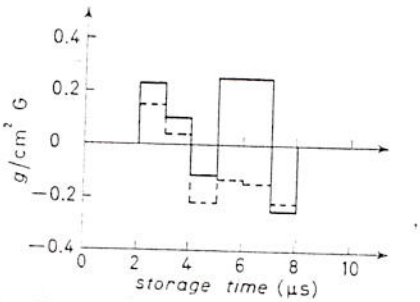

Fig. 56. – Mean range *vs.* storage time derived from Fig. 55 (solid line) and from ratio of counts in backward and forward telescopes, B/F method. —— direct measurements, – – – B/F method.

TABLE XI. – *Range of the ejected particles.*

Nature of absorber	Equivalent carbon in g cm^{-2}	Observations
½ window	0.68	The window consists of 1.5 mm Cu and 3 mm of plastic scintillator (No. 5). Stopping power of Cu = 0.815. Air path is between the exit window of the magnet and the front counter of the analyser. The stopping power of plexiglas relative to carbon is calculated to be 1.09, the density is 1.18.
Counters 6 and 6′	1.92	
2 mumetal walls, each 0.9 mm	1.18	
Scotch tape	0.10	
Counter 4, 2 mm thick and Scotch tape	0.30	
Air 80 cm	1.10	
Total	5.28	

(*) 1 cm CH_2I_2 ($\varrho = 3.3$) is equivalent to 2.2 g cm^{-2} of carbon.

By using the range-momentum relation, to be discussed in detail in Sect. 6·5, we can now obtain the mean orbit radius ϱ for each time band. This information is included in Table X.

iii) Correlation between the injected and ejected muons. To know the initial polarization we must find from which part of the injected range distribution the ejected muons are coming. We therefore evaluate the thickness traversed by these muons inside the magnet, taking into account such effects as the lengthening of the trajectory in the injection assembly because of the curvature in the magnetic field, see Table XII.

TABLE XII. – *Evaluation of the material thickness traversed in the magnet.*

Nature of absorber	Equivalent carbon in g cm^{-2}	Observations
Mylar windows	0.10	The density of beryllium is 1.84 and the stopping power 0.912 (*).
Counter 1 8 mm Counter 2 8 mm Counter 3 0.4 mm	1.97	
Helium bag 600 cm	0.11	Helium bag is between beam vacuum pipe and magnet window.
Be 8 cm	13.42	
Carbon 24.5 mm	5.02	
Curvature effect	0.3	
Total traversed before ejection	20.92	

(*) H. A. BETHE and J. ASHKIN: *Experimental Nuclear Physics* (E. SEGRÈ, Ed.) (New York, 1953), vol. 1, p. 201.

Adding this number to relation (95) we find for the total range of the muons stopping in the thin copper target, with X' cm of plexiglas in front of the polarization analyser

$$R' = 25.20 + 1.29\,X' \text{ g cm}^{-2} . \tag{96}$$

Note that at the peak of the output range curve $X' = 1.6$, giving $R' = 27.26$ g cm^{-2}. It thus appears that the stored muons have a median range 1.81 g cm^{-2} carbon higher than the apparent peak of the injected beam. This, in fact, is not surprising. We compare the range curve of the injected beam obtained in a compact geometry with that for the ejected beam obtained in loose geometry where the scattering plays an important role in selecting out the higher momenta. Very typical of this is the role of counter 3, traversed by the muons after one or two turns in the magnet. Its thickness, 0.4 mm, has a negligible effect on the residual range, but it scatters out 10 % of the beam. Also, the

apparent peak range at injection is shifted to lower values because of the superimposed sloping tail of the pion range curve.

The total error in the determination of the correspondence between the two range curves is estimated to be ± 0.4 g cm^{-2} carbon.

Combining eqs. (94) and (96) we find that the thickness of carbon X in the input beam measurements which corresponds to a given thickness X' of plexiglas at the output of the storage magnet, is given by

$$X = 0\ 63\, X' + 8.88 \text{ cm carbon} . \tag{97}$$

The standard carbon thickness used in the input polarization measurements was $X = 10.0$ (see Sect. 5·1.). Therefore the discrepancy between this standard and the stored range in each time band is

$$\Delta R' = \Delta X = 0.63\, X' - 1.12 \text{ cm carbon} , \tag{98}$$

where X' is the range in plexiglas for the corresponding storage time.

Using eq. (98), the final column in Table X can now be completed. This information will be combined with the measured change of polarization with range ($\mathrm{d}\theta/\mathrm{d}R$) to obtain the true injection polarization angle for each time band (see Sect. 5·2 and 7·1).

6·2.2. B/F method. When muons are stopped in a target the ratio B/F of the number of decay electrons counted in the backward and forward telescope is dependent on the average position of the muons in the target. The variation of this ratio as a function of the storage time therefore gives information about range as a function of storage time. To make this comparison one has to eliminate the effect of different spin orientations as a function of storage time. For this purpose we add the numbers obtained with the flipping field up and down, thus eliminating all asymmetry effects, without using additional running time.

A calibration of the amount of variation of B/F as a function of range is done by inserting a piece of absorber, namely 0.65 cm of plexiglas, and measuring the variation produced in B/F. The result is that a shift of the mean range by 0.33 cm of plexiglas changes B/F from 1.11 to 1.61. If we assume that the relation of B/F to range is linear in that region, we obtain the results of Fig. 56 that agree with those obtained by the direct range measurements.

6·2.3. Determination of the orbit position. The determination of the orbit position is necessary in order to calculate the average field $\bar{B}_t$ along the trajectory of a stored muon. It is important to note that as the orbit follows contour lines of the magnetic field (see Sect. 2·2), the mean field com-

puted at one value of x is valid throughout the magnet. For this reason the magnetic field is measured carefully at $x = 350$, and the position of the orbits as a function of storage time is determined at this position by measuring the maximum excursion y_w of the particles towards the weak field side. This is achieved by introducing a brass flap that can be moved in along the line $x = 350$ to intercept the orbits.

Figure 57 shows the variation of the number of stopped muons as a function of the position of the end of the brass flap, for storage time intervals 1 μs wide. The average maximum ordinate y_w reached by the orbits is calculated for each storage time band from these data. The mean position of the orbit centre for each storage time is then determined from

$$\bar{y}_c = \bar{y}_w - \bar{\varrho} \,, \tag{99}$$

where $\bar{\varrho}$ is taken from Table X, the results being shown in Table XIII.

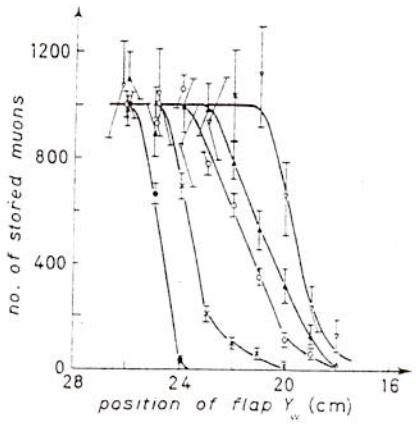

Fig. 57. – Stored intensity *vs.* flap position on the weak field side y_w for various time bands, measured at $x = 350$ cm. From these results we calculated the average maximum excursion of the orbit to the weak field side $\bar{y}_w$ for each time band: hence we obtain $\bar{y}_c$ *vs.* storage time: • 2 to 3 μs, × 3 to 4 μs, ○ 4 to 5 μs, ▲ 5 to 6 μs, ▽ 6 to 7 μs.

TABLE XIII. – ϱ, y_c *and* $\bar{B}$ *for* 1 μs *time bands.*

Time band	ϱ	y_c	$\bar{B}$
2.1÷3.1	19.40	−5.40	15.651
3.1÷4.1	19.15	−4.11	15.729
4.1÷5.1	18.90	−2.68	15.753
5.1÷6.1	19.00	−2.28	15.754
6.1÷7.1	19.00	−0.86	15.757
7.1÷8.1	18.90	+0.96	15.760

6·3. *Computation of* $\bar{B}_t$. – For each time band we now have the mean range of the stored particles from which we have computed the mean radius $\bar{\varrho}$, using the range-momentum relation. A detailed discussion of this relation is given below in connection with the injection scattering (Sect. 6·5) which it affects much more critically.

From the flapping curves we also have y_c for each time band, measured at $x = 350$ cm. We now combine this information with the known field shape

and known absolute value, both corresponding also to $x = 350$ cm (see Sect. 3·2 and 3·3).

To average over the orbit shape we compute $\bar{B}$ for circular orbits, using the measured values of $\bar{\varrho}$ and $\bar{y}_c$. The results are tabulated in Table XIII and plotted in Fig. 58.

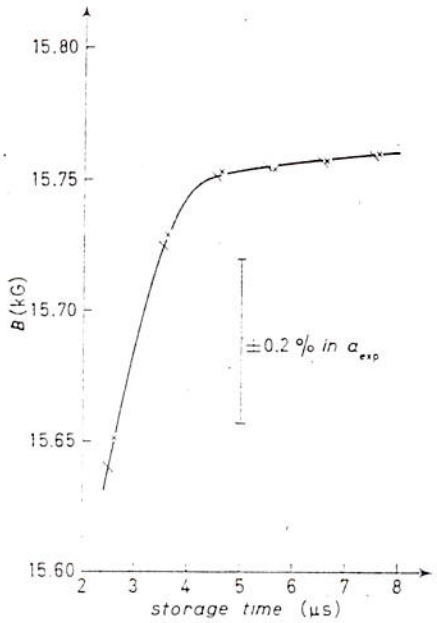

Fig. 58. – Mean field averaged over the orbit $\bar{B}$ *vs.* storage time t. × = point computed for $t = (2.1 \div 3.1)$ μs, etc.: ⁄ = value read off for $t = (2.0 \div 3.0)$ μs, etc.

Later, in connection with the injection scattering measurements, we were obliged to compute the trajectory step by step to find the exact shape in the region of $x = 350$. We took the opportunity of computing $\bar{B}$ for the true shape (see Sect. 6·5); the result agreed with the above to within 1/2 000.

As indicated in Table XIII the time bands used for reducing the measurements of y_c differed by one channel from the usual grouping. To avoid recalculating the data we interpolated to the correct bands using the graph of Fig. 58. The resulting values of $\bar{B}_t$ appear below in Table XVIII.

6·4. *Measurement of angle of arrival at analyser θ_p^t with « venetian blind » counter.* – In order to collect as many muons as possible, the width of the counters in the polarization analyser is 30 cm and the height 15 cm. However the great width introduces a broad distribution in the angles between the momentum of the muon and the reference direction perpendicular to the plane of the counters. It is necessary to know the average value of this angle, which may be a function of storage time and muon momentum. In the 2 % $(g-2)$ experiment ([13]) the angle distribution was obtained by measuring the number of muon arrivals as a function of the position of two slots. These were moved about to define different angles, and to cover different parts of the analyser. For the final measurements we devised a more precise technique of greater acceptance. A « venetian blind »-type counter of the same width as the analyser, was placed in front of it and defined the muon direction, independent of the position of arrival at the analyser.

This counter (see Fig. 59) consisted of 36 scintillation plates, each 10 cm high, 5 cm wide, and 6 mm thick, spaced about 0.23 cm. The scintillators rested on a light guide to which they were optically coupled by means of an

oil bath. Each could rotate around a vertical axis while remaining parallel to the others. The assembly was controlled by an arm A, the position of which was precisely determined by a micrometer. For these measurements the stopping muon signature was vetoed by the venetian blind counter. Therefore only muons which passed between the slats and then stopped in the analyser were counted.

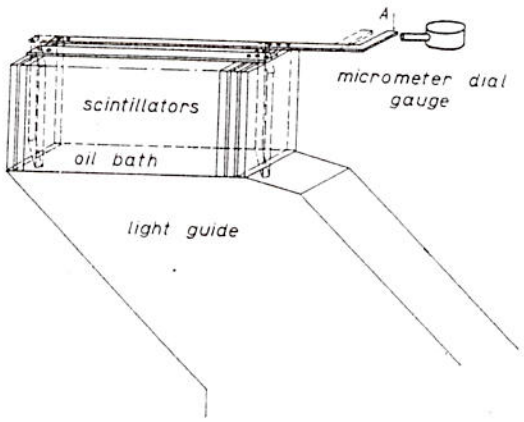

Fig. 59. – « Venetian blind » counter used to measure the direction of arrival of stored ejected muons at the analyser. Lever A controls angle of scintillators. Muon must pass between scintillators, giving no count.

The intrinsic spread in angles introduced by the width between the slats was $\pm 2.5°$.

To test the device it was placed in a pion beam defined by two counters (No. 1, 6 cm wide; No. 2, 4 cm wide; 40 cm apart, see Fig. 60). The anticoincidence curve obtained on turning the slats is also given in Fig. 60. The observed width of 5.7° accords with the expected resolution of the counter plus the angular divergence of the beam. This test showed the good efficiency of the device in eliminating particles arriving from completely wrong directions.

To measure the distribution in angle of the muons reaching the analyser from the storage magnet, the venetian blind counter was installed as shown in Fig. 61. This could be done without moving the analyser, and great care was taken to have the new counter parallel to the analyser assembly. Note that the reference direction for the slats was defined by mechanical measurements to be perpendicular to the plane of the assembly. The corresponding micrometer reading therefore defined normal incidence on the analyser.

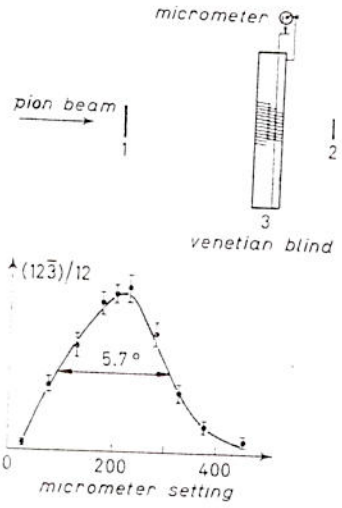

Fig. 60. – Test of « venetian blind » counter, with resolution curve obtained. 1, 2, plastic scintillators; 3, venetian blind counter used in anticoincidence.

The position of the analyser was defined relative to the magnet by means of a template which fitted against the yoke's lower pole piece. This enabled us to check that the analyser was always in the same position, and at the same angle to better than 0.2° throughout the whole storage experiment.

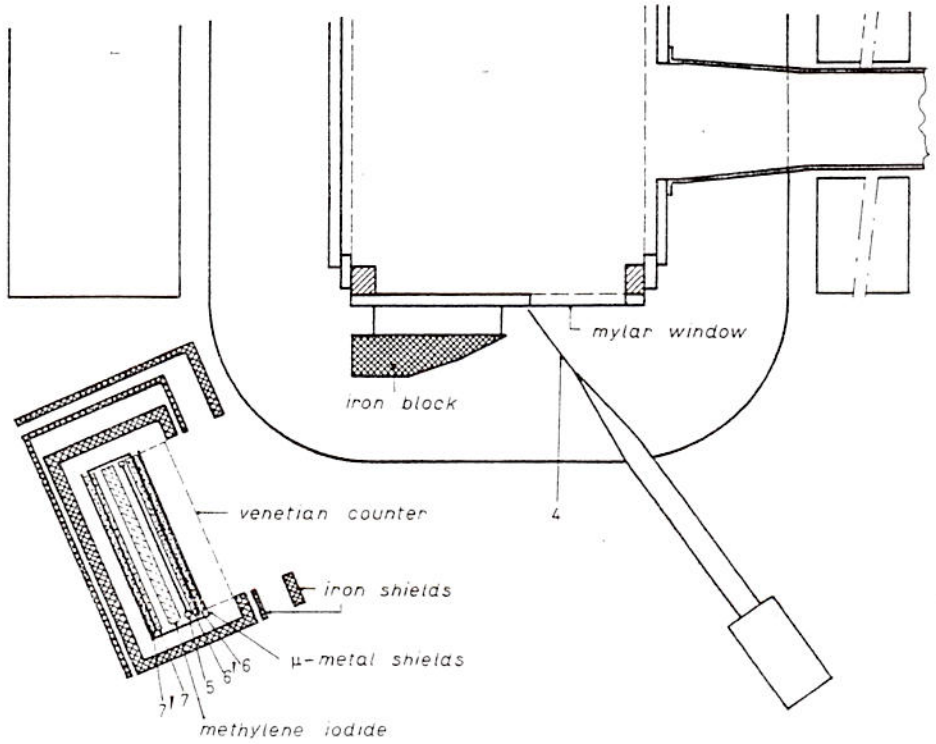

Fig. 61. – Ejection end of magnet with polarization analyser in position. The « venetian blind » counter was installed in position shown by dashed lines for measuring the direction of arrival.

The angular distribution required was that of the ensemble of muons which were recorded in the main experiment. It was essential therefore not only to require the muon to stop in the analyser, but also to require its decay electron to be counted. The efficiency for counting decay electrons drops off at the two sides of the analyser; so without this requirement one would get a wider angular distribution.

Accordingly we used the digitron with decay electron requirement as usual, adding the venetian blind counter as a veto to the stop telescope. In run 1 we recorded only the scaler readings giving gated decay electrons associated with a stopping muon. In run 2 we operated the digitron and recorded the

storage time distribution of the muons with decay electron requirement: in this case the totals were obtained by summing the time analyser channels, and we could also see if there was any correlated variation of arrival direction with storage time. The combined data for the two runs are plotted in Fig. 62.

We require only the average angle of arrival at the analyser and its error σ. This was computed separately for each run using

$$\theta_p = \sum nw\theta \Big/ \sum nw \,,$$

$$\sigma^2 = \sum n(\theta - \bar{\theta})^2 w^2 \Big/ \Big(\sum nw\Big)^2 \,,$$

where n is the number of counts observed at angle θ and this number is allocated to a band in θ of width w. (w is needed to weight the measurements when they are unequally spaced in θ.)

The results were as indicated in Table XIV.

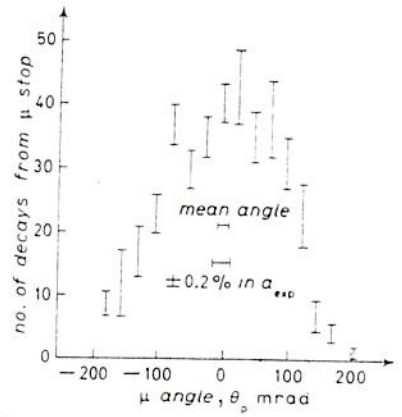

Fig. 62. – Distribution of muon arrival directions θ_p at the polarization analyser as measured by the « venetian blind » counter. Only muons which stop in the polarization analyser and give a decay electron count are included.

TABLE XIV. – *Mean direction of muon arrival, θ_p.*

Run	Requirement	θ_p micrometer div.
1	muon stop, gated decay electron, background subtracted	403 ± 12
2	muon stop, gated decay electron, plus correct time-of-flight for muon	388 ± 9
	weighted	395 ± 7
	normal to analyser	388 ± 10
	therefore, θ_p = arrival direction relative to normal { =	7 ± 15
	≡	−3.5 ± 7.5 mrad

Note. θ_p is measured in the direction of rotation of the muons in the magnet, clockwise looking from above.

The difference between runs 1 and 2 is within the error, so the two runs are combined statistically.

Time dependence of the angle of ejection. Because of the large spread in angles, it is necessary to investigate the possible dependence of the ejection angle on the storage time. We expect little dependence from the

spread in orbit centres because this is very much compressed in the ejection region, and the final trajectory is almost independent of y_c in the storage region. However, the curvature of the ejected trajectories in the fringing field is a function of momentum, and inasmuch as there is a (momentum-storage time) correlation not completely corrected by the c-term in the magnetic field, we may have a (storage time-ejection angle) correlation. To investigate this point $\bar{\theta}$ was evaluated separately for the muons stored in different 1 μs time bands ranging from 2 to 8 μs.

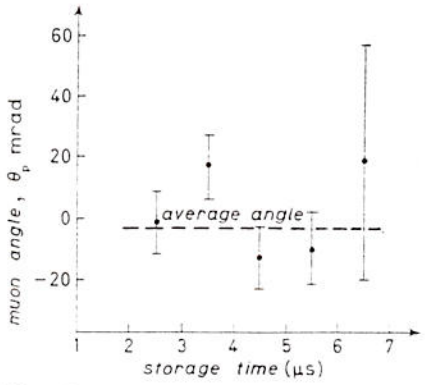

Fig. 63. – Muon arrival direction θ_p as a function of storage time. There is no significant correlation, so the mean value of θ_p can be applied to all time bands.

The results, plotted in Fig. 63, show no correlation large enough to affect our measurements.

The measurements have also been repeated without requiring an electron decay in the polarization analyser, thus giving a better statistical accuracy. They show that the dependence of the ejection angle on storage time is (1.5 ± 4) mrad per μs: a negligible effect.

Note that the average arrival angle measured here is the arithmetic mean, while strictly speaking, according to Sect. 1·2, we need the vector mean. However, for a distribution of width $\pm 10°$ it is readily shown that the error is negligible.

6·5. *Measurement of scattering in the injection assembly.* – A very serious problem in this experiment is caused by the multiple scattering in the injection assembly, which changes the polarization angle.

Suppose the particle is deviated through a small angle θ_p by a transverse electric field E acting for time t. Then

$$\theta_p = \frac{eEt}{p} .$$

In the rest frame the particle experiences a magnetic field $\mathfrak{B} = \beta\gamma E$ for time $\gamma^{-1}t$, which rotates the spin through angle $e/m_0c \cdot \beta Et = \beta^2\gamma\theta_p$. However, to this must be added the Thomas precession of the rest frame relative to the laboratory through angle $-(\gamma-1)\theta_p$. The net rotation of the spin in the laboratory is, therefore, $\theta_s = (1-1/\gamma)\theta_p$, and the polarization angle changes by $\theta = \theta_s - \theta_p = -\theta_p/\gamma$.

The relation between θ and θ_p is linear and therefore applies also when the

deflection θ_p is due to a series of electric fields acting for different times, provided only that the deflection is small at all times. It is, therefore, valid when the deflection is due to multiple scattering in matter.

If the particle is multiply scattered through horizontal angle ψ_{scat}, the polarization angle changes by

$$\theta_{\text{scat}} = -\psi_{\text{scatt}}/\gamma \,. \tag{100}$$

When a muon beam is passed through matter, left and right scatters are normally equally probable and there is no change in the mean polarization angle. However, if scatters in one direction are preferentially selected, there will be a net change in beam polarization. This happens at injection to the magnet, because left and right scatters in the beryllium moderator are not accepted for storage with equal efficiency.

The r.m.s. scattering angle (horizontal projection) for the injection assembly is $\sim 7°$. It is possible, therefore, that the injected particles are all scattered through an angle of this order leading to an error $\sim 5°$ in polarization angle [1.4 % in $(g-2)$].

To eliminate this uncertainty it is essential to measure the scattering suffered at injection for the particles which go into storage. In fact, the scattering angle largely determines the storage time t: particles scattered to the left have their orbit centres to the left of the magnet ($y_c < 0$, weak field side) and walk fast (see Sect. 2·2), and vice versa. The scattering angle is therefore to be determined separately for different storage time bands.

The principle of the determination is as follows (see Fig. 64). For a given orbit radius ϱ the angle at which the particles leave the beryllium block Be is uniquely related to the point y at which the particle crosses the line FF after making about one quarter turn. The object is to determine this position: i) for the stored particles, y^{t}_{mag}; and, ii) for the injected particles which have been slowed down in the injection assem-

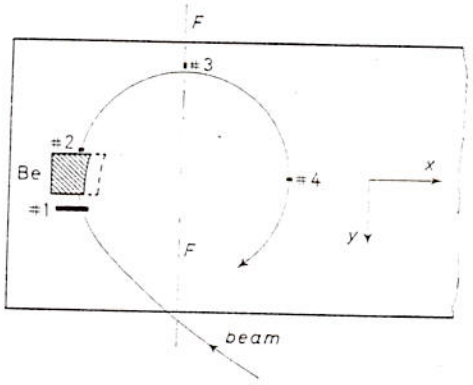

Fig. 64. – Method of measuring average multiple scattering angle in the injection assembly for the stored muons. 1, normal counter 1 of injection assembly; 2, scintillator 0.5 cm wide × 0.8 cm thick; 3, scintillator 0.5 cm wide × 0.04 cm thick movable along line FF; 4, scintillator 0.5 cm wide × 0.8 cm thick adjustable along x-axis, defines the orbit radius. The dashed line shows the position of the beryllium moderator when measuring the position y_{inj} corresponding to the unscattered injected beam.

bly, *but not scattered*, y_{inj}. In each measurement the radius of the orbit must be well defined and have the same value. Then, the correction to be applied to the polarization angle is

$$\theta^t_{scat} = -\psi^t_{scat}/\gamma = (y^t_{mag} - y_{inj})/\gamma\varrho. \tag{101}$$

To find y_{inj}, corresponding to the unscattered beam, we survey the whole Gaussian distribution of scattered particles and take the peak as corresponding to zero scattering.

We now describe in detail first the measurements on the injected beam, and then the measurements on the stored particles, indicating how the radius is defined in each case.

6·5.1. Measurement of y_{inj} with counters on the first half-turn. The position y_{inj} corresponding to the unscattered injected beam is obtained by defining the radius with the small counters No. 2 and No. 4 (an absorber is used to prevent multiple turns). One then probes along the line FF with a small counter No. 3 (0.4 mm thick $\times$ 5 mm wide), coincidences 1234 being recorded. In this way one plots out the whole scattering distribution of particles of a particular ϱ. The peak of the distribution then corresponds to the unscattered beam and gives y_{inj}.

For this procedure to be accurate several precautions are necessary. First, we are assuming that the scattering distribution is symmetric about zero; this will only be true if the particles pass through the injection assembly a long way from the right-hand edge of the Be block and counters. Therefore for this measurement the whole injection assembly is advanced 2 cm into the magnet. (See dotted position in Fig. 64.)

Secondly, in defining ϱ we must remember that No. 2 and No. 4 are not exactly at the ends of a semicircle, and, moreover, the field is not uniform. In fact, to keep ϱ strictly constant No. 4 must be moved as No. 3 is displaced. Therefore we have computed trajectories in the injection field and tabulated the position of No. 4 required to define a particular radius as a function of No. 2 and No. 3 position. Only when this is done do we get symmetrical Gaussian scattering distributions allowing us to identify the peak as the position of the unscattered beam. See Fig. 72 for a typical set of results.

Thirdly, as the beam emerging from the injection assembly is ~ 4 cm wide horizontally, and as different parts of the beam can have different unscattered injection angles, the measurements are repeated with counter No. 2 displaced horizontally in steps of 1 cm. We thus find y_{inj} as a function of No. 2 position. These results are then averaged, using as weighting factors the contribution of each position to the stored intensity. This is measured in a separate *storage* run using the small 5 mm wide No. 2 counter in place of the usual No. 2.

Figure 65 gives the results obtained for storage intensity in each time band as a function of No. 2 position. As the step-size in the injection region is ~ 2 cm there is no storage from positions more than 2 cm inside the edge of the beryllium block. There is a tendency for long storage times to favour positions near the edge, but this is not marked because all storage times have nearly the same step-size in the injection field.

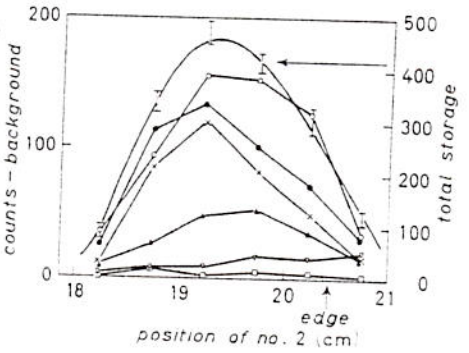

Fig. 65. – Stored intensity *vs.* position of counter 2 (cm - arbitrary zero) for various time bands. • 2 to 3 μs, × 3 to 4 μs, ○ 4 to 5 μs, ▲ 5 to 6 μs, ▽ 6 to 7 μs, □ 7 to 8 μs.

Figure 66 shows y_{inj} as a function of No. 2 position for three orbit radii. The mean $\bar{y}_{inj}$ weigthed according to the intensities of Fig. 65 is also indicated. Conceivably the weighting factors and therefore $\bar{y}_{inj}$ would be different for different time bands, but a calculation using the weights for individual time bands (see Fig. 65) shows that this effect is negligible. The same weights are applied to all radii because we know that there is very little correlation between radius and storage time (see Sect. 6·2).

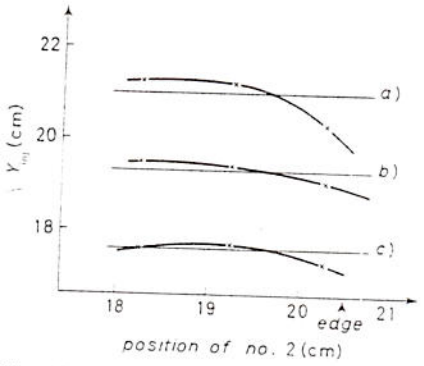

Fig. 66. – y_{inj} for unscattered injected beam for three orbit radii ϱ (cm) as a function of counter 2 position. The results for different counter 2 positions are weighted with the contributions each position gives to the *stored* intensity to obtain the mean value $\bar{y}_{inj}$ as shown.

To show the consistency of the data the nine measurements of y_{inj} are plotted *vs.* radius in Fig. 67, together with the three weighted averages $\bar{y}_{inj}$. It is convenient to find that the mean values lie on a straight line, which allows us to interpolate accurately to find $\bar{y}_{inj}$ corresponding to other radii.

We assign an error ± 2 mm in $\bar{y}_{inj}$ to the final curve of Fig. 67. Note that if the injected beam crosses the magnet centre line ($y=0$) at right angles, we expect to find $t_{inj} = \varrho$ for all radii. Figure 67 shows that this condition is nearly fulfilled, proving the successful operation of the magnet design.

6·5.2. Range curve and orbit radius. Before making flap measurements on the stored particles, it is necessary to define and measure the orbit radius. This is done by defining the range by means of the stop-telescope

(polarization analyser), using a thin range window (1.5 mm Cu+3 mm scintillator $\equiv 1.36$ g cm^{-2} of carbon). The range is varied by means of plexiglas absorbers. The calculation of the range R, in g cm^{-2} of carbon, in terms of the thickness X' of plexiglas, has been detailed above in Sect. 6·2 [see Table XI and eq. (95)]:

(95) $$R = 4.28 + 1.29\, X' .$$

Range-energy relation. To convert the measured range to particle momentum we must first correct the range for multiple scattering in the absorber. MATHER and SEGRÈ [26] show that the rectified range R is larger than the measured range R^* according to

(102) $$(R-R^*)/R = ZmR/3.5M ,$$

where m = mass of electron and M = mass of incident particle. Hence the correction is $\Delta R/R = Z/720 = 0.8\,\%$ for muons in carbon. From the more exact analysis of ØVERÅS [27] we find $\Delta R/R = 1.0\,\%$.

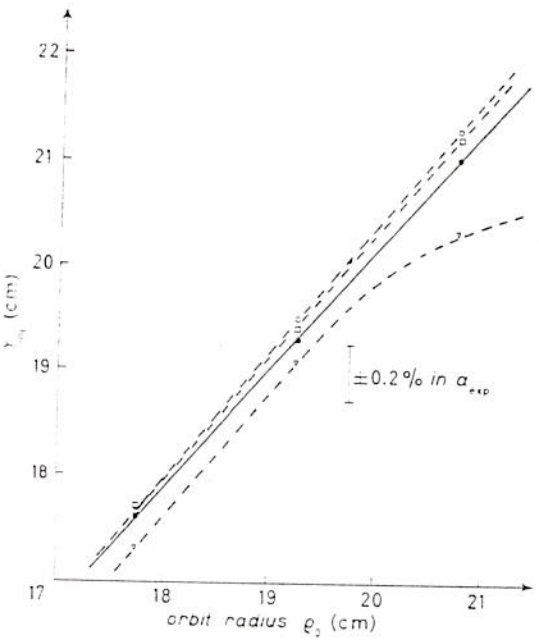

Fig. 67. – y_{inj} *vs.* orbit radius ϱ_0 for several positions of counter 2 (dashed curves). Solid curve shows $\bar{y}_{inj}$ *vs.* orbit radius. The straight line allows us to interpolate for other radii. Note that the injection is placing the orbit centres at $y_c = 0$ on the average as expected from the magnet design. ○ No. 2 at $x = 18.25$; □ No. 2 at $x = 19.25$, ▽ No. 2 at $x = 20.25$, • weighted mean.

For the range-energy relation itself there are two tabulations of the Bethe-Bloch formula; by RICH and MADEY [28] using the mean ionization potential $I = 69$ eV in carbon; and by STERNHEIMER [29] using $I = 78$ eV.

There is also a careful experimental determination by MATHER and SEGRÈ [26] of the range of 339.7 MeV protons in carbon. These have the same velocity as 97 MeV/c muons and therefore are exactly in the range of interest. The

---

[26] R. MATHER and E. SEGRÈ: *Phys. Rev.*, **84**, 191 (1951).

[27] H. ØVERÅS: *On Small Angle Multiple Scattering in Confined Bodies*, CERN Report 60-18 (1960).

[28] M. RICH and R. MADEY: Radiation Laboratory Report UCRL-2301 (1954).

[29] R. M. STERNHEIMER: Brookhaven National Laboratory Report BNL-4051 (1959).

point falls between the two theoretical calculations mentioned above, and corresponds to

$$I = 74.44 \text{ eV} .$$

Figure 68 shows the orbit radius ϱ_0, defined for the field ($B_0 = 15.871$ kG) at the centre line of the magnet ($y = 0$), plotted against thickness of plexiglas absorber, using the range-energy relation of Rich and Madey. The experimental point of MATHER and SEGRÈ (converted to the same scale), is indicated for comparison. The Sternheimer curve would fall 1.5 mm lower in ϱ_0.

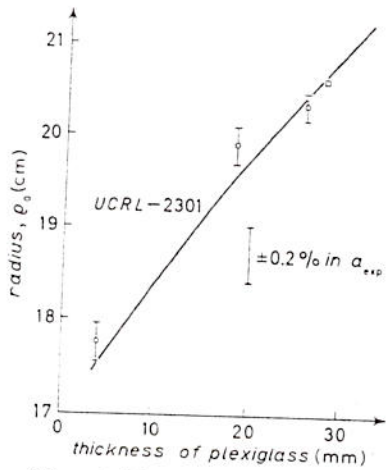

Fig. 68. – Orbit radius ϱ_0 *vs.* range of ejected muons (cf. Fig. 54). Line calculated from RICH and MADEY (ref. [28]). ▫ calibration point from MATHER and SEGRÈ (ref. [26]); ∤ direct radius measurements in our magnet using flaps.

As a check on the method we have made spot measurements of the orbit radius by probing with mechanical shutters along the line $x = 350$. The three points obtained in this way (see below) agree reasonably well with the curve as shown in Fig. 68. The agreement with the Sternheimer curve (1.5 mm lower in radius, not plotted) would be less good. This leads us to adopt the Rich-Madey curve for interpolating our data. However, we do not wish to imply that this curve is necessarily more correct: we are using it to interpolate our data, and the agreement with this relation rather than with Sternheimer may be due to an accumulation of errors in our range measurement.

In summary the radius of the orbits is defined by the range telescope using the curve of Fig. 68 to which is assigned an error of ± 2 mm in radius.

6·5.3. Direct measurement of orbit radius by flapping at 350. As a check on the orbit radius computed from range we measured the radius directly by probing with mechanical shutters (flaps) along the line $x = 350$.

The range was first defined by means of a thin range window, as above, and we than recorded the storage time distribution as a function of flap position. Figures 69 and 70 show how the muons stored in different time bands were intercepted by the flaps. Note that the flaps were used one at a time, never together.

To get a sensitive measurements of radius we analyse the results for each time band separately: in effect storage time t is used here as a label to identify

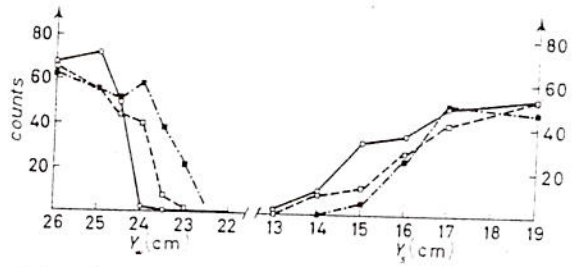

Fig. 69. – Radius determination for range 18.5 mm plexiglas. Stored intensity *vs.* flap positions y_w and y_s on weak and strong field sides, respectively. The results of these radius measurements have been plotted in Fig. 68.

Flapping at $x=350$. *Range* $=18.5$ mm *plexiglas.*

Band	Apparent diam.	ϱ_0 (corrected)	Mean ϱ_0
$2.5 \div 3$	40·65	20·17	
$3 \div 3.5$	39·96	19·83	19.88 ± 0.2
$3.5 \div 4$	39·54	19·65	

the same group of muons on each side of the magnet. Although the orbit centre y_c varies with t and therefore the flaps cut different time bands at different points, we expect that the radius, as defined by range, will be independent of t.

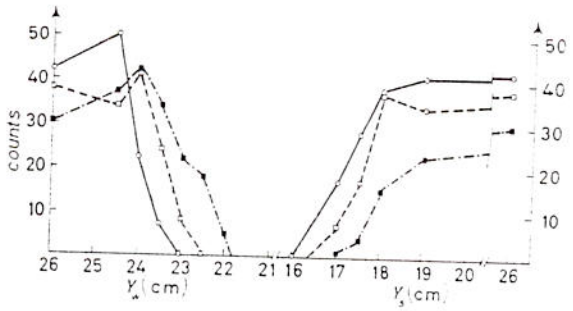

Fig. 70. – As Fig. 69, but at range 26 mm plexiglas.

Flapping at $x=350$. *Range* $=26$ mm *plexiglas.*

Band	Apparent diam.	ϱ_0 (corrected)	Mean ϱ_0
$3.5 \div 4$	41·18	20·46	
$4 \div 4.5$	40·74	20·25	20.31 ± 0.15
$4.5 \div 5$	40·67	20·22	

From the readings of the « integral flapping curve » n_y of stored rate at flap position y, with y increasing in equal steps Δ, one computes the mean value of y from

$$\bar{y} = 26 - \Delta/2 - (\sum n_y)/n_{26} . \tag{103}$$

This gives the extrema of the orbit y_w and y_s on the weak field side (WFS) and strong field side (SFS), respectively. The crude evaluation of orbit radius $\varrho = 0.5(y_s - y_w)$ must now be corrected for the nonuniformity of the field.

We define the radius ϱ_0 as the radius at $y = 0$ (field $B_0 = 15.871$ kG), and compute the shape of the orbit from the measured field.

For a given $d\Theta$ in the direction Θ of the trajectory

$$dy = \varrho \cos\Theta \, d\Theta = \varrho_0 [B_0/B(y)] \cos\Theta \, d\Theta .$$

Hence the extremum of the orbit is given by

$$y_s = \varrho_0 B_0 \int_0^{\pi/2} \frac{\cos\Theta \, d\Theta}{B(y)} , \tag{104}$$

where in $B(y)$ we can use the approximation $y = \varrho_0 \sin\Theta$.

Similarly for y_w. This calculation is repeated for various orbit radii ϱ_0 and position y_c. At the same time one computes $\bar{B}$ the mean field for this particular orbit. A typical set of results is given in Table XV.

TABLE XV. – *Extrema of orbit and mean field for* $\varrho_0 = 19$ cm.

y_c (cm)	y_w (cm)	y_s (cm)	Apparent diameter (cm)	Apparent centre (cm)	$\bar{B}/B_0$
−7	−26.48	−12.00	38.48	−7.24	0.979
−6	−25.36	−12.99	38.36	−6.18	0.986
−5	−24.29	−13.99	38.28	−5.15	0.990
−4	−23.26	14.99	38.24	−4.13	0.992
−3	−22.23	15.99	38.22	−3.12	0.993
−2	−21.22	16.99	38.20	−2.11	0.993
−1	−20.20	17.99	38.19	−1.10	0.993
0	−19.18	19.00	38.18	−0.09	0.993
−1	−18.16	20.01	38.17	+0.92	0.994

Thus the correction, usually ~ 2.5 mm, to find the true diameter $2\varrho_0$ from the measured diameter $(y_s - y_w)$ is established.

The points obtained in this way have been plotted on the range-radius curve of Fig. 68 and, as already mentioned, check reasonably well. They are within our error assignment of ± 2 mm to the curve.

As already mentioned the values of $\bar{B}$ computed in this way agreed with those obtained above for circular orbits (Sect. 6·3).

6·5.4. Position measurements of the stored particles. It remains to find the position of the stored particles y^t_{mag} on the line FF on their first quarter turn. Here it is possible only to do integral measurements, killing the storage gradually by introducing an obstacle, or flap. An essential point here is that the field is uniform with respect to x in the region of measurement, and the orbits do not jitter sideways during the first few turns more than 0.2 cm (see Sect. 3·2 and Fig. 30). If they did the position measured with the flap could correspond to, say, the second or third turn, not the first quarter turn as we require.

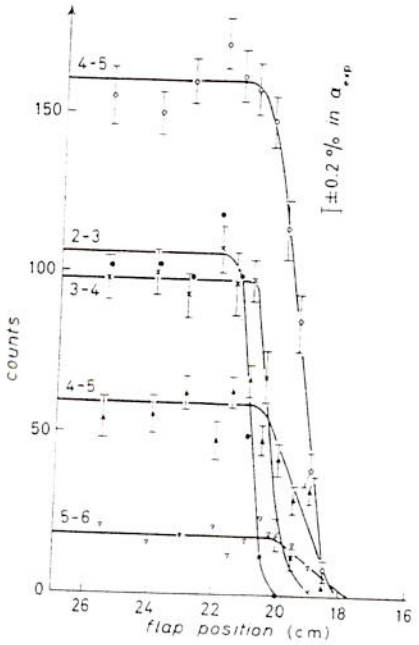

Fig. 71. – Determination of y^t_{mag} the maximum excursion of the stored beam along the line FF (see Fig. 64) for various storage times t. This set of curves applies to muons of range 14 mm plexiglas as defined by the muon stop telescope at ejection. The corresponding orbit radius is read from Fig. 68, so that the comparable value of $\bar{y}_{\text{inj}}$ can then be found from Fig. 67. The difference $(y^t_{\text{mag}} - \bar{y}_{\text{inj}})$ then measures the mean scattering at injection of this group of muons labelled by storage time t and radius ϱ_0.

Preliminary measurements with a brass flap indicated that the stored intensity was at first *increased* when the flap was pushed in a certain distance. Clearly particles which would normally leave the magnet were being scattered into storage by the flap, thus distorting the measurement. To avoid this trouble the mechanical flap was replaced by a scintillator which was used to veto the signal from the injection assembly. Then, any particle which touched the flap could not be registered as a stored event.

For these measurements the normal injection assembly was used with the usual 2 cm wide No. 2 counter. One does not need to study y^t_{mag} as a function of No. 2 position because it is defined, not by the injection system, but by the properties of the magnetic field. Once the radius and storage time are specified there is only one possible value of y^t_{mag}. All that the injection system

can determine is *how many* particles are available at this point, and this does not affect the present measurement. (Cf., for example, Sect. 6·5.1.)

A typical set of results is given in Fig. 71. From the readings one calculates the mean position of the beam for each time band using the procedure indicated in Sect. 6·5.3. The results of these measurements are plotted in Fig. 72 and tabulated in Table XVI. We thus have a detailed study of y^t_{mag} as a function of range and storage time. From the consistency of the data we assign an error ± 2 mm to y^t_{mag}.

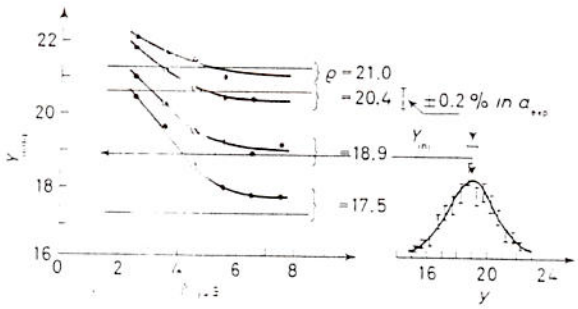

Fig. 72. – Synthesis of injection scattering measurements. The position of the stored particles y^t_{mag} is plotted *vs.* storage time t for four different orbit radii. The corresponding horizontal straight lines show the value of $\bar{y}_{inj}$ for the same radii. The difference between $(y^t_{mag} - \bar{y}_{inj})$ measures the scattering in the injection assembly. *Inset at right.* Typical multiple scattering curve for the injected particles of given radius. The centre of this curve gives y_{inj} the position corresponding to zero scattering.

TABLE XVI.

	Time band (μs)	Range – mm lucite				Mean values $\bar{\theta}^t_{scat}$
		4	14	26	32	
y_{mag} cm	2÷3	20.45	20.97	21.78	22.1	
	3÷4	19.64	20.25	21.21	21.7	
	4÷5	18.55	19.60	20.71	21.4	
	5÷6	17.98	19.20	20.4	21.2	
	6÷7	17.81	19.90	20.4	21.15	
	7÷8	17.75	19.0	20.4	21.1	
radius cm		17.50	18.92	20.42	21.0	(see Fig. 68)
γ		1.27	1.30	1.35	1.36	
y_{inj}		17.33	18.92	20.62	21.28	(see Fig. 67)
θ^t_{scat} mrad	2÷3	138	83	42	28	68
	3÷4	104	54	22	14	47
	4÷5	55	28	4	3	28
	5÷6	29	12	– 7	– 3	10
	6÷7	21	4	– 7	– 5	4
	7÷8	19	4	– 7	– 7	4

6·5.5. Correlation of data. To combine the measurements one proceeds as follows. From the range one deduces the orbit radius using Fig. 68 (see Sect. 6·5.2), and then reads off the corresponding value of $\bar{y}_{inj}$ from Fig. 67 (see Sect. 6·5.1). Equation (101) then determines the correction θ'_{scat} to be applied to the input polarization for each time band and range. These results are included in Table XVI.

To find the final mean value of the correction for each time band we must now weight the four entries according to the range curves of Fig. 55 (see Sect. 6·2). These give, for each time band, the contribution of each range element to the stored muon intensity. The final mean values $\bar{\theta}'_{scat}$ are also included in Table XVI.

To estimate the error we have to combine the error assignments already given, *viz.* ± 2 mm in $\bar{y}_{inj}$, ± 2 mm in y_{max} and ± 2 mm in correlating the radius assignments in the injection and the storage measurements. Combining these errors in quadrature gives ± 3.2 mm, which corresponds to ± 13 mrad in θ'_{scat}. As this error is systematic rather than statistical we take it to apply over the whole range of storage time.

One further source of error remains to be considered. The direction of the unscattered injected beam depends on where the particles come from: those that are focused onto the injection assembly from the right-hand side of the quadrupole lens tend to have $-ve\,\theta$ and a larger value of y_{inj}, and vice versa. This effect was measured by blocking alternately the left- and right-hand sides of the quadrupole. The corresponding displacement in y_{inj} was ~ 6 mm.

Therefore, if by an unlucky chance the stored particles all come from one side of the quadrupole, our value of y_{inj}, measured for the whole beam, could be wrong by ~ 6 mm.

A priori this is unlikely, because the multiple scattering in the beryllium block ($\sim \pm 7°$) is much greater than the spread ($\sim \pm 1.5°$) of the incident beam. An experimental check was made by measuring the storage time distribution with half the quadrupole blocked as above. There was no appreciable difference in the shape of the time distributions, but a 17 % difference in intensity. Combining the two results one finds an error less than 1 mm in y_{inj}, which is negligible.

6·6. $(g-2)$ *precession data.* – A major part of the running time was devoted to the determination of $A(t)$ *vs.* t, that is, to the $(g-2)$ precession curve itself. Here it was important to make sure that the running conditions were exactly the same as in the other measurements. A careful check was kept on all magnet currents (including the solenoid and the cyclotron). These were held constant at their old values to $\sim 1{:}1000$, and the storage magnet itself to $\sim 1{:}4000$.

At the beginning, the available core storage (TMC kicksorter) was split

into two groups of 128 channels each, allowing us to record 12.8 μs of storage time for two groups of data, corresponding to backwards and forwards muon decay in the polarization analyser. This allowed us to record data corresponding to negative storage times and thus to determine the background.

In fact there was a flat background from -2.2 to $+1.8$ μs, giving 41 time channels which were used for the measurement. For 40000 muons stopped in the analyser (~ 10000 decay electrons) there were 29 background counts in 82 channels (41 for forward decay $+41$ for backward decay), corresponding to (0.35 ± 0.07) per channel. This background is, therefore, negligible compared with statistical errors in a run of this length, even if one groups the counts in 10 channels together. However, for the whole run, totalling 936000 stopped muons, it is worth subtracting the background which is known to sufficient accuracy from the above data, *viz.* (8.2 ± 1.6) counts per channel.

The background is understood as follows. In order to score a background event we need a signal in the analyser simulating a stopped muon, followed by a decay electron, and this must be associated by chance with a 123 coincidence event at the input of the magnet. The background is due essentially to stored muons which stop in the analyser and give decay electrons in the usual way, but which have not been detected by the input telescope: they physically miss counter No. 3 for example, or give a pulse smaller than circuit threshold. If this event is associated by chance with a second input particle which does actuate 123, we have a background event. (Note that the rejection circuits do not operate because, although there are two input particles, only one of them is detected in the 123 telescope).

To estimate this background we need P_1, the probability of a stored muon not giving a 123 signal. This is obtained by comparing the total number of particles passing through the magnet with the number registered by the digitron. The following data were obtained for runs of $2 \cdot 10^6$ 12-coincidences (*i.e.*, ~ 6 minutes).

TABLE XVII. – *Calculation of* P_1.

Stopping muon counts in analyser	=	1518
Background measured with flaps at $X=350$ completely closed	=	16
Therefore, total stored particles stopping in analyser	=	1502
K pulses (*) (measured)	=	1380
Hence, number of stored muons which do not have a 123 count = $= 1502 \div 1380$	=	122
P_1	=	8.1%

(*) See Fig. 46. To obtain a K pulse we need a stopping muon, plus an associated 123 count.

The probability of finding another input particle, giving a 123 count, within 12 μs, is obtained from the double-pulse rejection probability P_2. P_2 = ratio of N pulses to K pulses (see digitron circuit, Fig. 46). For the same runs we find $P_2 = 11.5\,\%$. Hence, one expects a background in 12 μs (120 channels) of $1502 \times P_1 P_2 = 14\,\%$; per time channel this is 0.01 % of the total stored rate.

As this background is due to muons we expect the same ratio when we introduce the decay electron requirement. The estimate agrees well with the 0.009 % per time channel reported above.

It remains to consider whether the background is completely uniform. As explained above the background is not due to an electronic failure of the rejection circuits, but involves only one count in the input telescope and one count at the output. There is therefore no possible electronic effect which can give a sloping background. A strong cyclotron beam structure could make the background slope, but as the pulse length of the machine was ~200 μs, this was negligible.

As the background is due to decay electrons from muons stopping in the target, it may be different for forward and backward decays, and may depend on the sign of the flipping field. The relevant quantity is the average polarization of the stored muons. Taking the average symmetry from the precession curve of Fig. 73, we find $\bar{A} \sim 0.015$, which means that the error in assuming the same background for all channels is negligible.

The change in $\mathbf{a}_{exp}$ due to the inclusion of the background is only 0.04 %, one tenth of the quoted error.

A disadvantage of displaying in the kicksorter 12.8 μs of time for forward and for backward decays was that we had to print and clear the analyser every time we reversed the direction of the flipping field. To save time we therefore allocated only 61 channels to each set of data (6.1 μs of time which embraced all the significant part of the time distribution). The kicksorter was divided into 4 groups of 64 channels accumulating separately the data for the 4 possibilities, forward or backward decay, with flipping field up or down.

We then reversed the flipping field automatically for every 1000 stopped muons (~1000 s), and printed the data after every 10^4 muons (~3.5 hours). Out of a total of 104 runs, each of 10^4 stopped muons, 14 were rejected (11 due to electronic failure, 2 to power failure, 1 to mistake in starting); a few doubtful cases were tested by finding whether the corresponding value of $\mathbf{a}_{exp}$ had a significant deviation from the mean. The valid data, totalling 936000 stopped muons, were grouped into 21 sub-runs of unequal length according to the way it had been allowed to accumulate in the kicksorter, and separately analysed for the value of $\mathbf{a}_{exp}$ to check for consistency. The final value was obtained by adding all runs together, with subtraction of background as explained above.

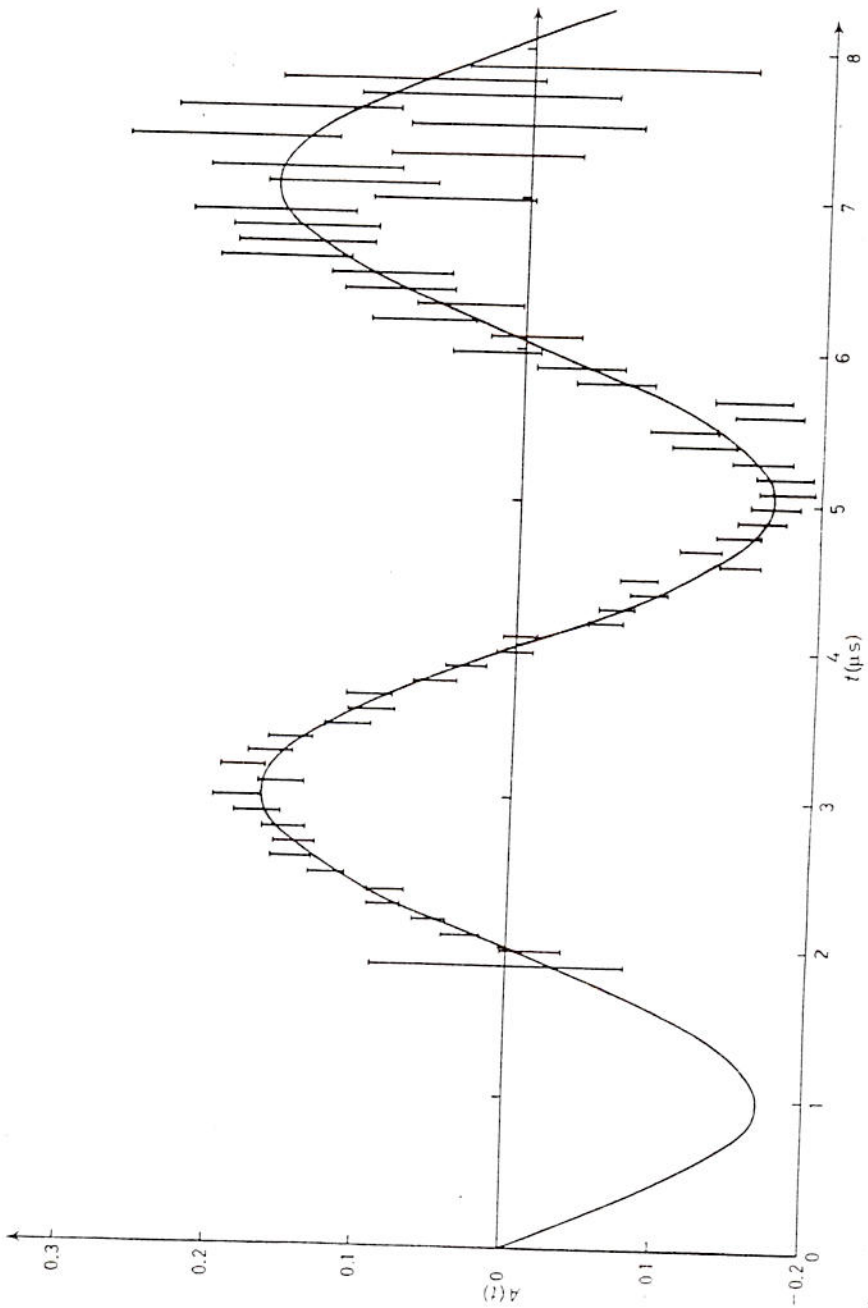

Fig. 73. – Precession curve due to the anomalous magnetic moment of the muon. The frequency of this curve essentially determines $\mathbf{a}_{\mathrm{exp}}$. Electron asymmetry $A(t)$ for $\pm 90°$ flipping (combined data from backward and forward telescopes) is plotted *vs.* storage time t. The curve shows the best fit obtained by varying A_0 and $\mathbf{a}$ in eq. (108).

The data of electron asymmetry $A(t)$ obtained for the combined data are shown in Fig. 73, together with the best fit obtained by varying A_0 and **a** in eq. (108), see below.

7. – Analysis of the data.

7·1. *Final equation for fitting asymmetry data.* – From the decay electron counts in a particular telescope (forward or backward), $n^+_{f,b}(t)$ and $n^-_{f,b}(t)$ for $\pm 90°$ flipping of the muon spin at storage time t, one computes the asymmetry

$$A_{f,b}(t) = \frac{n^+_{f,b}(t) - n^-_{f,b}(t)}{n^+_{f,b}(t) + n^-_{f,b}(t)} = A_0 \sin\theta_s(t) , \tag{105}$$

where $\theta_s(t)$ is the spin direction with respect to the normal to the analyser.

In fitting the data to the fundamental eq. (18)

$$\theta(t) - \theta_t(0) = \mathbf{a}\omega_0 \bar{B}_t \cdot t \tag{18}$$

we have to allow for the corrections already mentioned in the initial polarization $\theta_t(0)$.

With the symbols defined in Sect. 5·1, 5·2 and 6·5

$$\theta_t(0) = \theta^t_{\text{mag}} + \theta^t_{\text{scat}} = \sum \theta_{\text{mag}}(R_0) + \left(\frac{\mathrm{d}\theta}{\mathrm{d}R}\right)_{\text{beam}} \Delta R^t + \theta^t_{\text{scat}} . \tag{106}$$

The determination of the individual terms in eq. (106) as a function of the time band t has been explained in Sect. 6·2 and 6·5.

The final polarization angle is

$$\theta(t) = \theta_s(t) - \theta^t_p , \tag{107}$$

where θ^t_p is the angle of muon arrival relative to the normal to the analyser as measured in Sect. 6·4.

Combining eqs. (18), (105), (106) and (107), the asymmetry observed at storage time t should be fitted to

$$A(t) = A_0 \sin\theta_s(t) = A_0 \sin\{\mathbf{a}\omega_0 \bar{B}_t t + \varphi_t\} , \tag{108}$$

where the phase is defined by

$$\varphi_t = \theta^t_p - \sum \theta_{\text{mag}}(R_0) - \left(\frac{\mathrm{d}\theta}{\mathrm{d}R}\right)_{\text{beam}} \Delta R^t - \theta^t_{\text{scat}} . \tag{109}$$

The results of the measurements leading to the values of φ_t and $\bar{B}_t$ as a function of storage time are collected together in Table XVIII.

TABLE XVIII. – *Combined data for $\bar{B}$ and φ.*

Time band (μs)	$\bar{B}_t$ (kG)	ΔR^t (cm)	$\left(\frac{d\theta}{dR}\right)\cdot\Delta R_t$ (mrad)	θ^t_{mag} (mrad)	θ^t_{scat} (mrad)	θ^t_p (mrad)	Correction due to field in analyser (mrad)	φ (mrad)
2÷3	15.640	0.11	−2.1	− 9.9	+68	−3	−6	+49
3÷4	15.725	−0.01	+0.2	− 7.6	+47	−3	−6	+31
4÷5	15.753	−0.12	+2.3	− 5.6	+28	−3	−6	+13
5÷6	15.754	−0.09	+1.7	− 6.1	+10	−3	−6	− 5
6÷7	15.757	−0.10	+1.9	− 5.9	− 4	−3	−6	−11
7÷8	15.760	−0.14	+2.7	− 5.1	− 4	−3	−6	−10
Error	±0.010			±12	±13	±7.5	±5	±20
Notes	*a*	*b*	*c*	*d*	*e*	*f*	*g*	*h*

Notes: *a*) See Sect. 6·3.
b) See Sect. 6·2.1, Table X.
c) Calculated from *b*), see eq. (87), Sect. 5·1.
d) Column *c*) −7.8 mrad, see eq. (93), Sect. 5·2.
e) See Sect. 6·5.5, Table XVI.
f) See Sect. 6·4.
g) See Sect. 4·1 and 4·1.3.
h) The sum of columns *d*), *e*), *f*) and *g*), eq. (109).

The value of the constant ω_0 is obtained from the precession frequency $(1+\mathbf{a})\omega_0$ of muons at rest in a known magnetic field as determined by HUTCHINSON *et al.* (9), namely 13.554 kHz per gauss.

7·2. *Least-square procedure.* – A two-parameter least-squares fit to the asymmetry data is carried out by varying A_0 and $\mathbf{a}$ in eq. (108) as follows.

The error in $A_{f,b}(t)$ as defined by eq. (105) is to a sufficient approximation

$$(n^+_{f,b}(t) + n^-_{f,b}(t))^{-\frac{1}{2}} = n^{-\frac{1}{2}}, \tag{110}$$

where n are the total counts which contribute. In the case of the net asymmetry for forward and backward telescopes combined $\bar{A} = \frac{1}{2}(A_f - A_b)$ the error is

$$(n^+_f + n^+_b + n^-_f + n^-_b),$$

again corresponding to the total counts which contribute to the point.

The observed asymmetries $A(t)$ are now to be fitted to an equation of the type

$$y_t = A_0 \sin(Bt + \varphi) . \tag{111}$$

Putting $B = B^* + b$, where B^* is the expected frequency, we linearize eq. (111) in b:

$$y_t \approx A \sin(B^* t + \varphi) + A_0 t b \cos(B^* t + \varphi) . \tag{112}$$

Applying the method of least squares we demand

$$\sum n_t \left(y'_t - A \sin(B^* t + \varphi) - A_0 t b \cos(B^* t + \varphi)\right)^2 = \text{minimum} , \tag{113}$$

where y'_t are the experimental asymmetries, and n_t is the total number of counts. By differentiation with respect to A_0 and b and equating to zero we get the conditions:

$$\sum n_t (y'_t - A_0 p_t - A_0 b q_t)(p_t + b q_t) = 0 , \tag{114}$$

$$\sum n_t (y'_t - A_0 p_t - A_0 b q_t) q_t = 0 , \tag{115}$$

with $p_t = \sin(B^* t + \varphi)$ and $q_t = t \cos(B^* t + \varphi)$. Solving for b one finds

$$b = \frac{\sum n_t y'_t q_t \sum n_t p_t^2 - \sum n_t y'_t p_t \sum n_t p_t q_t}{\sum n_t q_t^2 \sum n_t y'_t p_t - \sum n_t p_t q_t \sum n_t y'_t q_t} \tag{116}$$

and by inserting this value for b into

$$A_0 = \frac{\sum n_t y'_t q_t}{\sum n_t p_t q_t - b \sum n_t q_t^2} \tag{117}$$

one obtains the amplitude, without having to assume an *a priori* value for it.

Alternatively, one can assume a value A^* and write

$$A_0 = A^* + a$$

$$B = B^* + b$$

$$y_t = f(t, A_0, B) = f(t, A^*, B^*) + a \left(\frac{\partial f}{\partial A}\right)_{A^*, B^*} - b \left(\frac{\partial f}{\partial B}\right)_{A^*, B^*} \approx$$

$$\approx A^* \sin(B^* t + \varphi) + a \sin(B^* t + \varphi) + A^* b t \cos(B^* t + \varphi) \equiv y_t^0 + a u_t + b v_t .$$

Applying the same least squares method as above, we find the conditions:

$$\chi^2(a, b) = \sum n_t(y_t' - y_t^0 - au_t - bu_t)^2 = \min , \tag{118}$$

$$\begin{cases} \dfrac{\partial \chi^2}{\partial a} = 0 \text{ gives } \sum n_t(F_t - au_t - bv_t)\, u_t = 0 \\ \dfrac{\partial \chi^2}{\partial b} = 0 \text{ gives } \sum n_t(F_t - au_t - bv_t)\, v_t = 0 \end{cases} \tag{119}$$

where $F_t \equiv y_t' - y_t^0$. Solving eq. (119) for a and b:

$$a = \frac{\sum n_t u_t F_t \sum n_t v_t^2 - \sum n_t u_t v_t \sum n_t v_t F_t}{\sum n_t u_t^2 \sum n_t v_t^2 - (\sum n_t u_t v_t)^2} , \tag{120}$$

$$b = \frac{\sum n_t u_t^2 \sum n_t v_t F_t - \sum n_t u_t v_t \sum n_t u_t F_t}{\sum n_t u_t^2 \sum n_t v_t^2 - (\sum n_t u_t v_t)^2} . \tag{121}$$

In practice, the data were analysed twice as a check: once using eqs. (116) and (117), and once using eqs. (120) and (121).

To calculate the errors in a and b, again two equivalent procedures were used. Once A_0 and b are known from eqs. (116) and (117), we reinsert these values into eq. (111). By varying the value of A and b around the values found above, we obtain two χ^2 curves. The change in A and b required to raise the minimum value of χ^2 to χ^2+1 is then the error sought. For each change in the value of, say, A_0, χ^2 must be «reminimized» by varying b. This increases the error in A_0 slightly.

To obtain the errors in a more analytical way, it is perhaps easiest to start from eq. (118); we again define the error in a, say, as that increment in a that increases χ^2 by one, provided b is readjusted to minimize χ^2 when a is varied. We have (putting $\chi^2 = \psi$):

$$\psi(a + \delta a, b + \delta b) - \psi(a, b) = \frac{1}{2}(\delta a)^2 \frac{\partial^2 \psi}{\partial a^2} + \delta a\, \delta b \frac{\partial^2 \psi}{\partial a\, \partial b} + \frac{1}{2}(\delta b)^2 \frac{\partial^2 \psi}{\partial b^2} = 1 . \tag{122}$$

Note that the first derivatives are zero by virtue of eq. (119). The condition for minimum as far as variation of b is concerned is:

$$\left(\frac{\partial \psi}{\partial b}\right)_{a+\delta a,\ b+\delta b} = 0 ,$$

that is,

$$\frac{\partial^2 \psi}{\partial a\, \partial b} \delta a - \frac{\partial^2 \psi}{\partial b^2} \delta b = 0 . \tag{123}$$

Eliminating δb from eqs. (122) and (123) and setting $(\delta a)^2 = \sigma_a^2$ we have

$$\sigma_a^2 = \frac{2(\partial^2\psi/\partial b^2)}{(\partial^2\psi/\partial a^2)(\partial^2\psi/\partial b^2) - (\partial^2\psi/\partial a\,\partial b)^2}. \tag{124}$$

From eq. (118) follows

$$\frac{\partial^2\psi}{\partial a^2} = 2\sum n_t u_t^2; \qquad \frac{\partial^2\psi}{\partial b^2} = 2\sum n_t v_t^2; \qquad \frac{\partial^2\psi}{\partial a\,\partial b} = 2\sum_t n_t u_t v_t;$$

and thus

$$\sigma_a^2 = \frac{\sum n_t v_t^2}{\sum n_t u_t^2 \sum n_t v_t^2 - (\sum n_t u_t v_t)^2}. \tag{125}$$

The expression for σ_b^2 is the same with u_t and v_t interchanged. The result (125) can also be arrived at by use of the error matrix (*).

In computing the sums over time channels required in the least-square procedure, the values of φ_t or $\bar{B}_t$ in Table XVIII are inserted for the corresponding time channels.

Note that the curve fitted to the data is not a pure sine wave because φ_t and $\bar{B}_t$ are functions of storage time. However, for a particular ensemble of particles labelled by the subscript t, $\bar{B}_t$ and φ_t are determined by the injection or ejection conditions and remain fixed: so the polarization angle of the ensemble increases uniformly with time as the particles run through the magnet following eq. (18).

7·3. *Results.* – The data were divided into 21 separate runs as described above; for each run a value of $\mathbf{a}_{\text{exp}}$, the amplitude A_0, the errors, and χ^2 were calculated separately for the forward and backward telescopes, and for the combined asymmetry $\bar{A} = \frac{1}{2}(A_f - A_b)$. The results for the separate runs are listed in Table XIX. The values of χ^2 for these fits ($\chi^2 = 58$ expected) are in accord with the expected distribution (**).

The distribution of the 21 values about their weighted mean is also statistical ($\chi^2 = 20.3$, expected value 19.3).

To obtain the final value, the runs were added together in two groups (an electronic modification which shifted the zero of time by 66 ns after 160 000 muon arrivals made it impossible to sum all data together). The back-

(*) See, for example: R. L. PLACKETT: *Principles of regression analysis* (Oxford, 1960), p. 36.

(**) We are indebted to Dr. D. HUDSON for a comparison of our values with the theoretical χ^2 distribution using « probability paper ».

TABLE XIX. – *Anomalous moment evaluation for separate runs of $A(t)$ vs. t.* The distribution of the individual results about the combined value 1162 is statistical, $\chi^2=20.3$, expected value 19.3.

Run	$a_{exp}\cdot 10^6$	χ^2 for this fit (expectation value = 58)	Difference from final value of a_{exp}	Statistical error $\cdot 10^6$
1	1169	65	+ 7	13
2	1155	70	− 7	14
3	1135	58	−27	15
4	1165	49	+ 3	16
5	1149	76	−13	19
6	1183	50	+21	14
7	1162	53	0	13
8	1154	61	− 8	15
9	1197	68	+35	16
10	1132	72	− 30	14
11	1162	86	0	19
12	1178	50	+16	16
13	1133	62	−29	23
14	1160	63	− 2	13
15	1154	50	− 8	36
16	1174	71	+12	16
17	1150	57	−12	26
18	1145	51	−17	17
19	1146	48	−16	23
20	1181	70	+19	19
21	1173	66	+11	27

ground was subtracted (see Sect. 6·6) and the same quantities were computed for each group with the results given in Table XX, with corresponding statistical error.

TABLE XX. – *Value of $a_{exp}\cdot 10^6$ from combined runs.*

	Forward	Backward	Combined	χ^2 (combined)
Group A	1167± 5	1155± 5	11 623±3.6	60
Group B	1168±11	1149±11	11 613±8.0	45

Combining these results and including in the error estimate the systematic uncertainty in φ_t from Table XVIII, we obtain finally

$$(126)\qquad \begin{cases} a_{exp} = (1162 \pm 5)\cdot 10^{-6} \\ \quad = a_{th}\times(0.997\,4 \pm 0.004\,3)\,. \end{cases}$$

[For a_{th} see eq. (4).] Of the overall error of 0.43 %, statistics of the asymmetry constitutes 0.30 %, errors in the initial polarization 0.18 %, in the injection scattering 0.20 %, and in the final mean beam direction 0.11 %. (*)

8. – Implications of the result.

As we have seen in the last Section, the experimental result eq. (126) agrees within its estimated error with the theoretical prediction eq. (4) to within a few parts per million in g. This Section will be devoted to discussing the consequences of this remarkable agreement in terms of i) limits on the validity of QED; ii) possible structure of the muon; iii) possibility that the photon is a Regge pole; and, iv) unknown couplings or interactions of the muon.

It is possible that several of the effects are operating simultaneously and that their effects accidentally cancel or interfere. While this cannot logically be ruled out, it is instructive to evaluate separately the magnitude of each effect, and to set limits for its existence on the assumption that it is acting by itself.

At the time we started our experiment, the muon and the electron were known to share, within the experimental uncertainty, the same interactions (electromagnetic and weak) and the same intrinsic properties apart from the mass. Since then it has been shown that the neutrinos coming from π decay produce a larger quantity (~ 50 times more) of muons than electrons ([30]). This can be interpreted as showing the existence of a new quantum number, the muonic quantum number, which is a conserved quantity. The muonic quantum number is the first observed difference between muon and electron; but does not resolve the problem of the muon-electron mass difference, which remains one of the deeper mysteries of elementary particle physics.

8·1. *Electrodynamics of the muon.* – In considering to what extent our result verified QED and the pointlike interaction of the muon with the electromagnetic field, it is necessary to postulate some inevitably arbitrary modification of the laws, characterized by a parameter Λ. By comparing the modified theory with the experimental result, limits on Λ can then be specified.

(*) G. R. HENRY, G. SHRANK and R. A. SWANSON using a different technique have recently obtained the result $a_{exp} = (1060 \pm 67) \cdot 10^{-6}$ [G. R. HENRY: *Thesis*, Princeton University (May 1963)].

([30]) G. DANBY, J. M. GAILLARD, K. GOULIANOS, L. M. LEDERMAN, N. MISTRY, M. SCHWARTZ and J. STEINBERGER: *Phys. Rev. Lett.*, 9, 36 (1962); G. BERNARDINI *et al.*: *Proc. of the International Conference on Elementary Particles at Sienna*, vol. 1, (1963), p. 571.

Consider the Feynman diagram (see Fig. 74) responsible for the lowest-order anomalous magnetic moment of the muon (second order in e).

In this diagram one can alter: a) the photon propagator; b) the muon-photon vertices; or, c) the muon propagator.

The change of the photon propagator implies a breakdown of QED, which unfortunately cannot be described in a self-consistent way. The easiest and most popular assumption is to replace the normal photon propagator $1/K^2$ with

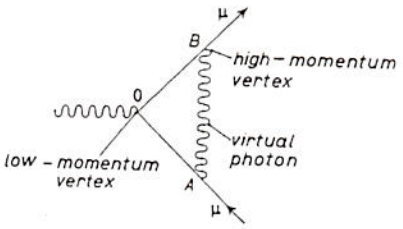

Fig. 74. – Feynman diagram for lowest-order contribution to a_{th}.

$$\frac{1}{K^2}\cdot\frac{\Lambda^2}{K^2+\Lambda^2}=\frac{1}{K^2}-\frac{1}{K^2+\Lambda^2}\,. \tag{127}$$

However, this violates the conservation of probability; for instance as shown by FEYNMAN ([31]), if, using this new photon propagator, one calculates the probability that an electron in a hydrogen atom is in a state « a », plus the probability that it is in another state, one does not find unity, but $(1+K^2/\Lambda^2)^{-1}$.

The effect on the anomalous magnetic moment due to such a change of the photon propagator has been calculated by BERESTETSKIJ *et al.* ([4]), the result being

$$\mathbf{a}'/\mathbf{a}=\left[1-\frac{2}{3}\left(\frac{m_\mu}{\Lambda}\right)^2\right],\quad \text{for } \Lambda^2\gg m_\mu^2\,. \tag{128}$$

However, if the muon electromagnetic vertex is changed from the usual γ_μ to $\gamma_\mu\Lambda^2/(K^2+\Lambda^2)$, which could imply either a modification of the basic rules or more probably the existence of a muon form factor, the anomalous moment is altered by the amount

$$\mathbf{a}'/\mathbf{a}=\left[1-\frac{4}{3}\frac{m_\mu^2}{\Lambda^2}\right],\qquad \text{for } \Lambda^2\gg m_\mu^2\,, \tag{129}$$

as calculated by DE TOLLIS ([32]). This author has also calculated the effect of a change in the muon propagator of the form

$$\frac{1}{(p+K)^2+m_\mu^2}\qquad\text{to}\qquad\frac{1}{(p+K)^2+m_\mu^2}\cdot\frac{\Lambda^2}{(p+K)^2+m_\mu^2+\Lambda^2}\,;$$

the result is

$$\mathbf{a}'/\mathbf{a}=\left[1-\frac{2}{3}\frac{m_\mu^2}{\Lambda^2}\left(\ln\frac{\Lambda^2}{m_\mu^2}+\frac{1}{3}\right)\right],\quad \text{for } \Lambda^2\gg m_\mu^2\,. \tag{130}$$

([31]) R. P. FEYNMAN: *Phys. Rev.*, **76**, 778 (1949).
([32]) B. DE TOLLIS: *Nuovo Cimento*, **16**, 203 (1960).

Another possibility is that pointlike theories do not exist in nature and that all fields, the electromagnetic field as well as the muonic, are characterized by a nonlocality expressed by a cut-off parameter Λ. In this case all the effects mentioned above will operate simultaneously: this supposition gives the limit on the supposed fundamental length which is included in Table XXI.

TABLE XXI.

		Λ (GeV)	Λ^{-1} (fermi)
1	Cut-off in the photon propagator	$\geqslant 0.8$	$\leqslant 0.24$
2	Cut-off in the muon e.m. vertex	$\geqslant 1.1$	$\leqslant 0.18$
3	Cut-off in the muon propagator	$\geqslant 2.0$	$\leqslant 0.10$
4	Effects 1+2+3 added to the fundamental length	$\geqslant 2.5$	$\leqslant 0.08$
5	Cut-off in the dispersion integral	$\geqslant 1.5$	$\leqslant 0.14$
6	Cut-off in the dispersion integral (with a spectral function)	$\geqslant 3.7$	$\leqslant 0.055$
	All figures are given with 95% confidence		

As we have seen, the magnetic moment of the muon is a quantity sensitive to the QED breakdown and to a deviation from a pointlike description of the muon. For illustrative purposes we have kept separate the effect of a change in the muon electromagnetic vertex and in the muon propagator. The vertex and the muon propagator are however related by the Ward identity, and any change in one affects the other if gauge invariance is maintained.

An alternative approach is to express the anomalous magnetic moment as a dispersion integral ([33]) and to calculate the effect of stopping the integration at an upper limit Λ instead of infinity ([34]). The result is

$$\mathbf{a}'/\mathbf{a} = \left[1 - 2\left(\frac{m_\mu}{\Lambda}\right)^2\right]. \tag{131}$$

To introduce a sharp cut-off in the dispersion integral might appear to be a little unphysical. A more reasonable way would be to cut off the dispersion integral gradually by adding the weighting factor (or spectral function) $\Lambda^2/(K^2+\Lambda^2)$ to the integrand. In this case the result, according to PETERMANN ([35]), is

$$\mathbf{a}'/\mathbf{a} = \left[1 - 4\left(\frac{m_\mu}{\Lambda}\right)^2 \ln\left(\frac{\Lambda}{m_\mu}\right)\right]. \tag{132}$$

([33]) S. D. DRELL and F. ZACHARIASEN: *Phys. Rev.*, **111**, 1727 (1958).

([34]) V. B. BERESTETSKIJ: *Žurn. Eksp. Teor. Fiz.*, **39**, 1427 (1960) [translation: *Sov. Phys. JETP*, **12**, 993 (1961)].

([35]) A. PETERMANN: unpublished.

The values obtained for Λ in these various cases are tabulated in Table XXI, assuming that the experimental result is $a_{\text{exp}} > 1152 \cdot 10^{-6}$, *i.e.*, allowing two standard deviations, and so obtaining the 95 % confidence limits. The values corresponding to one standard deviation have already been published [14].

The physical reason why the dispersion integral should have a cut-off is either because the muon or the photon, or both, are not describable by point-like theories. The physical significance of this cut-off in the dispersion integral is therefore related to our previous fundamental length; it is interesting to note that these two different approaches give quite similar results.

8·2. *Slope of photon trajectory.* – Another way of modifying QED is to treat the photon as a Regge pole. If the photon has a sloping trajectory in the Chew-Frautschi-Regge diagram then the calculation of the anomalous moment will be modified. DRELL (*) considered this effect by changing the photon propagator $1/K^2$ into

$$\frac{1}{K^2}\left(\frac{s}{s_0}\right)^{\alpha_\gamma(K^2)-1},$$

where K^2 is the square of the momentum transfer (also denoted t), s the energy variable, $\alpha_\gamma(K^2)$ the spin of the photon as a function of K^2, and s_0 a characteristic energy to be fixed. Assuming $\alpha_\gamma(K^2) - 1 \simeq \eta t$, where η is the slope of the photon trajectory and taking

$$s_0 = (2m_\mu)^2 \simeq (200 \text{ MeV})^2 , \tag{133}$$

the result is $\eta \leqslant 0.1$ GeV^{-2}. However, if we take

$$s_0 = (2m_e)^2 \simeq (1 \text{ MeV})^2 , \tag{134}$$

the result is $\eta \leqslant 0.03$ GeV^{-2}.

The experiment therefore establishes that the slope of the photon trajectory is at least ten times less than the Pomeranchuk slope of ~ 1 GeV^{-2}.

8·3. *Unknown interactions of the muon.* – Let us now see what limits we can put on the interactions of the muon with an unknown field. This is a relevant point because of the present understanding of the masses as originating only from interactions. The muon is 200 times heavier than the electron, and this may be due to an interaction with an, as yet, undiscovered particle [7,8,36].

(*) S. D. DRELL: *Proceedings International School of Physics, Enrico Fermi*, Course XXVI (New York, 1963), p. 231.

[36] I. YU. KOBZAREV and L. B. OKUN': *Žurn. Eksp. Teor. Fiz.*, **41**, 1205 (1961) [translation: *Sov. Phys. JETP*, **14**, 859 (1962)].

If the muon is coupled to another field in addition to the electromagnetic then in calculating $(g-2)$ it is necessary to consider the diagram, Fig. 75, involving a virtual quantum of this unknown field. This will to first order give an independent effect to be added to the electromagnetic corrections already discussed.

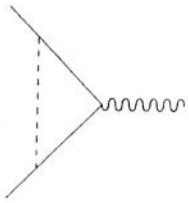

Fig. 75. – Contribution to a_{th} from other interactions of the muon (cf. Fig. 74).

The field may be of scalar, pseudoscalar, or vector type, and the mass of the field-quantum can have any value; moreover, the coupling strength is also unspecified. Indicating with f_s, f_p, f_v, and with M_s, M_p, M_v, the coupling constant and the masses of these unknown fields, scalar, pseudoscalar, and vector, respectively (*), the contribution to the anomalous magnetic moment will be

$$\frac{\delta\mu}{\mu_0} = + f_s^2 \cdot \frac{1}{\pi}\left(\frac{m_\mu}{M_s}\right)^2 \ln\left(\frac{M_s}{m_\mu}\right) \qquad \text{(scalar case)}, \tag{135}$$

$$\frac{\delta\mu}{\mu_0} = - f_p^2 \cdot \frac{1}{\pi}\left(\frac{m_\mu}{M_p}\right)^2 \ln\left(\frac{M_p}{m_\mu}\right) \qquad \text{(pseudoscalar case)}, \tag{136}$$

$$\frac{\delta\mu}{\mu_0} = + f_v^2 \cdot \frac{1}{\pi}\left[\frac{1}{3}\left(\frac{m_\mu}{M_v}\right)^2 - \left(\frac{m_\mu}{M_v}\right)^4 \ln\left(\frac{M_v}{m_\mu}\right)^2\right] \qquad \text{(vector case)}. \tag{137}$$

If, purely as an example, we suppose that the mass of the hypothetical field is equal to the nucleonic mass, we get, with 95 % confidence, the following limits for the coupling constants:

$$\begin{cases} f_s^2 \leqslant 8 \cdot 10^{-4}\,; \\ f_p^2 \leqslant 1.5 \cdot 10^{-3}\,; \\ f_v^2 \leqslant 5 \cdot 10^{-3}\,. \end{cases} \tag{138}$$

For a more massive field, however, larger coupling constants are permissible, as shown in Fig. 76.

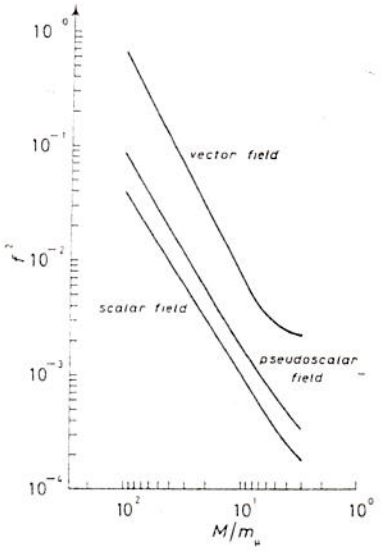

Fig. 76. – Upper limit to the coupling constant f^2 for an unknown field of mass coupled to the muon, as a function of M.

(*) We prefer the notation of ref. ([36]) to that of ref. ([8]) used in our earlier publications (13), (14). Note that $f^2 \equiv G^2/4\pi$ of the earlier papers.

8·4. *The muon mass.* – By combining our result with the precession frequency of muons at rest, we obtain an accurate value for the mass of the muon

$$\frac{m_\mu}{m_e} = \frac{g_\mu}{g_e} \times \frac{f_e}{f_p} \times \frac{f_p}{f_\mu} \times \frac{e_\mu}{e_p}, \tag{139}$$

where the ratio of muon and proton precession frequencies in the same field [9] $f_\mu/f_p = 3.1833 \pm 0.00004$. Correspondingly for the electron [37] $f_e/f_p = 658.2107$, while g_e and g_μ are determined by eqs. (3) and (126). Equation (139) yields the result

$$\frac{m_\mu}{m_e} = 206.765 \pm 0.003 . \tag{140}$$

The error here is determined almost entirely by the error in f_μ/f_p, and we have made the assumption $e_\mu = e_e$.

8·5. *Vacuum polarization effects in muon physics.* – The contribution of electron vacuum polarization effects in the magnetic moment of the muon amounts to $\sim 5 \cdot 10^{-6}$, which is just our experimental error. We could conclude that we measure the existence of this effect with 100 % error. However, there is a way of using the $(g-2)$ result in order to establish the presence of electron vacuum polarization effects in muon physics to ± 4 % accuracy. This result is obtained by combining the new mass value with the X-ray energy in the transition $(3D\text{-}2P)$ of μ-mesic phosphorus [10-12]. The energy of the μ-mesic X-ray is proportional to $m_\mu e_\mu^2 C_\mu$, where m_μ is the mass of the muon, e_μ its electric charge, and C_μ a constant which contains first- and second-order vacuum polarization effects, reduced mass, and α [see PETERMANN and YAMAGUCHI [38]]. Now that the muon mass is known indepen dently by eq. (140) we can regard the X-ray experiment as a measure of C_μ, instead of the mass, for which it was originally designed. The contribution of electron vacuum polarization effects in C_μ amounts to 331.42 eV, compared with the experimental uncertainty in X-ray energy of $(^{+15}_{-10})$ eV. We conclude that electron vacuum polarization effects in muon physics are correct to an accuracy of ± 4 %. Notice that the existence of electron vacuum polarization effects in electron physics is checked by the Lamb shift to $\sim \pm 1$ % and by the electron $(g-2)$ result [eq. (3)] to ± 2 %.

8·6. *Limit on the mass of hypothetical leptons.* – If, together with the electron and muons, other leptons were to exist with the same electromagnetic

---

[37] J. W. M. DUMOND: *Ann. Phys.*, **7**, 365 (1959).
[38] A. PETERMANN and Y. YAMAGUCHI: *Phys. Rev. Lett.*, **2**, 359 (1959).

properties of the known leptons, their contribution to the vacuum polarization would depend only upon their mass, m. As no such supplementary vacuum polarization is detected we can conclude, using the result of the previous paragraph, that $m \geqslant 10\, m_e$ (*). The corresponding limit calculated from the more precise determination of the vacuum polarization in the Lamb shift is also $m \geqslant 10\, m_e$ (*).

8·7. *Limit on the electric charge of* ν_μ. – As mentioned above, the X-ray energy of μ-mesic phosphorus is proportional to $m_\mu e_\mu^3 C_\mu$, where m_μ is the muon mass, e_μ the muon electric charge, and C_μ a constant (see above). The ratio (e_μ/m_μ) is known from the combination of the $(g-2)$ result with the total precession frequency [see eq. (139)]. Instead of using the μ-mesic X-ray experiment to check vacuum polarization effects in muon physics, we can use it to check e_μ. It comes out that

$$e_\mu = (1.000\,00 \pm 0.000\,05)\, e_e\,, \tag{141}$$

where e_e is the electron charge.

Because the neutron charge is known to be zero with a high degree of accuracy ([39]) $[e_n \leqslant 10^{-19} e_e]$, by applying charge conservation to the reaction

$$\pi^- + \mathrm{p} \to \mathrm{n} + \gamma\,,$$

it is known that the π and the proton have the same charge. The equality of the proton-electron charge is established to a high degree of accuracy ([40]) $[e_p = e_e(1 \pm 10^{-16})]$ and therefore in the decay

$$\pi \to \mu + \nu_\mu$$

conservation of electric charge implies that the ν_μ cannot have a charge larger than that which is allowed by eq. (141); conclusion

$$e_{\nu_\mu} = (0.000\,00 \pm 0.000\,05)\, e_e\,. \tag{142}$$

Note that from the absence of high-energy proton recoil tracks in the bubble chamber during the CERN neutrino experiment ([41]), one can deduce

---

(*) We are indebted to Dr. J. S. BELL for these calculations.

([39]) E. FERMI and L. MARSHALL: *Phys. Rev.*, **72**, 1139 (1947).

([40]) J. C. ZORN, G. E. CHAMBERLAIN and V. W. HUGHES: *Phys. Rev.*, **129**, 2566 (1963).

([41]) H. H. BINGHAM, H. BURMEISTER, D. CUNDY, P. G. INNOCENTI, A. LECOURTOIS, R. MØLLERUD, G. MYATT, M. PATY, D. PERKINS, C. A. RAMM, K. SCHULTZE, H. SLETTEN, K. SOOP, R. G. P. VOSS and Y. YOSHIKI: *Proc. of the International Conference on Elementary Particles at Sienna*, vol. 1 (1963), p. 555.

the better limit $e_{\nu_\mu} < 10^{-7} e_e$. Other evidence has been discussed by BERNSTEIN *et al.* [42].

* * *

This project owes much to several decisions and suggestions of Prof. G. BERNARDINI, and to the initiative of Prof. L. M. LEDERMAN during his visit to CERN in 1959. We express our particular appreciation also to Profs. W. K. H. PANOFSKY, V. L. TELEGDI and C. M. YORK for their contributions at various stages of the experiment.

We are indebted especially to our technicians Messrs. B. NICOLAI, R. BOUCLIER and J. BERBIERS for their untiring support through long periods of arduous preparation.

We wish to thank also Dr. B. HEDIN and Messrs. F. BLYTHE and A. ALBRECHT for contributions to the magnet design and mechanical parts.

Finally we are grateful to Mr. E. LEYA and the cyclotron operators, for their collaboration during our many tests and runs on the CERN Synchro-cyclotron.

APPENDIX

Step by step computation of trajectories.

A point on a trajectory is specified by its (x, y) co-ordinates and the angle Θ between the momentum vector and the x axis. To find the subsequent trajectory one first computes the motion in the horizontal plane. We calculate a succession of small steps in each of which the field can be regarded as uniform, and the element of trajectory is therefore a circular arc of radius (in cm) $\varrho = 3.336\, p/B$, where p is the momentum in MeV/c, and the field B is in kG.

For a step-length h the new co-ordinates are:

$$\Theta' = \theta + h/\varrho \,, \tag{143}$$

$$x' = x + h\cos(\Theta + h/2\varrho) = x + h\cos\Theta - \frac{h^2}{2\varrho}\sin\Theta \,, \tag{144}$$

$$y' = y + h\sin(\Theta + h/2\varrho) = y + h\sin\Theta + \frac{h^2}{2\varrho}\cos\Theta \,. \tag{145}$$

---

[42] J. BERNSTEIN, G. FEINBERG and M. RUDERMAN: *Phys. Rev.*, **132**, 1227 (1963).

[43] K. T. BAINBRIDGE: *Experimental Nuclear Physics*, Vol. 1, ed. E. SEGRÈ (New York, 1953), p. 584.

In eqs. (144) and (145), which are computed first, it is sufficient to use the ϱ value corresponding to the magnetic field at the initial point (x, y), because ϱ enters only in the term of order h^2. Having calculated (x', y') one finds the mid-point of the step and uses the corresponding value of ϱ in eq. (143): as ϱ enters here in the first order term, the field at the mid-point must be used. The whole procedure is then correct to order h^2.

The motion of the particle in the vertical plane may be followed at the same time, using as variables z the height above the median plane, and ζ the inclination of the trajectory to the horizontal. The motion is determined by the horizontal component of field normal to the trajectory,

$$B_{\text{horiz}} = z\left(\frac{\partial B}{\partial y}\cos\Theta - \frac{\partial B}{\partial x}\sin\Theta\right).$$

To second order in h one finds

$$z' = (1 - 0.5h^2q)z + h\zeta\,, \tag{146}$$

$$\zeta' = -hqz + (1 - 0.5h^2q)\zeta\,, \tag{147}$$

where

$$q = \left(\frac{\partial B}{\partial y}\cos\theta - \frac{\partial B}{\partial x}\sin\theta\right)\Big/B\varrho \tag{148}$$

is computed at the mid-point of the step.

As eqs. (146) and (147) are linear equations which could be written in matrix form, the final result after many steps will be of the same general form

$$\begin{pmatrix} z'' \\ \zeta'' \end{pmatrix} = \begin{pmatrix} a_{11} & a_{12} \\ a_{21} & a_{22} \end{pmatrix}\begin{pmatrix} z \\ \zeta \end{pmatrix}.$$

To find the matrix connecting initial and final conditions, the simplest procedure is to follow the vertical motion of two particles, the first starting with the initial condition $\begin{pmatrix} 0 \\ 1 \end{pmatrix}$ and the other starting with $\begin{pmatrix} 1 \\ 0 \end{pmatrix}$. The final position and inclination of these two tracks then give the four components of the matrix. As a control on the calculation one can check that the determinant of the matrix is unity.

We have used this programme in various versions depending on the way the magnetic field is specified in the computer. With a theoretical field of analytical form one can specify B and q as functions of (x, y) by analytical expressions. More generally one may specify values of B on a lattice of measured points, and compute the gradients from the differences in neighbouring values.

For some calculations it has been useful to have an approximate analytical expression for the fringing field at the edge of the magnet. An expression

which is quickly computed and gives a good fit to a typical fringing field (43) is

$$\frac{B}{B_0} = \frac{0.1 - \eta - 3\eta^3}{0.125 - \eta - 3\eta^3} \qquad \text{if } \eta < 0 ,$$

$$\frac{B}{B_0} = \frac{0.8}{1 + 2\eta} \qquad \text{if } \eta > 0 ,$$

where $\eta =$ distance from edge in gap widths.

As the exact fringing field depends on the properties of the iron and the disposition of the magnet coils, there is nothing to be gained, in preliminary calculations, by looking for a more exact analytical representation.

RIASSUNTO

La parte anomala del rapporto giromagnetico $a = 1/2(g-2)$ del muone è stata misurata facendo precedere dei muoni da 100 MeV/c in un campo magnetico statico di forma polinomiale, $B \approx B_0(1+ay^2+by^2+cy^3+dy^4)$, e misurandone la precessione $\theta = a\omega_0 \overline{B}t$ in funzione del tempo di cattura « t ». Il risultato è $a_{\text{sperimentale}} = (1162 \pm 5) \cdot 10^{-6}$ da confrontare col valore teorico $a_{\text{teorico}} = \alpha/2\pi + 0.76(\alpha/\pi)^2 = 1165 \cdot 10^{-6}$. Questo accordo prova che il muone obbedisce alle leggi dell'elettrodinamica quantica fino a distanze di circa un decimo di fermi. Vengono discussi in dettaglio: i metodi usati per la cattura magnetica dell'ordine di mille giri per i muoni, le tecniche di misura e le precauzioni necessarie al fine di raggiungere la precisione voluta. Alcuni metodi di analisi delle orbite, di costruzione e misura dei campi magnetici, di analisi di polarizzazione, e di misura elettronica digitalizzata dei tempi di cattura può essere di interesse generale.

END